University of Nottingham
UK | CHINA | MALAYSIA

Numerical Simulation of DBD Plasma Actuators for Flow Control

Huw Borradaile

Thesis submitted to the University of Nottingham
for the degree of Doctor of Philosophy

September 18, 2021

Abstract

Millimetric and sub-millimetric DBD plasma actuators have been investigated for flow control applications using a 4-species plasma-fluid model. The discharge structures for a number of cases were studied and an understanding of the mechanics of these plasma actuators was developed.

The model was initially used to investigate the mechanism behind the unexplained flow reversal observed in annular DBD actuators. It was found that at reduced diameters, the increased curvature of the electric field was responsible for suppressing the discharge during the positive part of the cycle, and thereby inducing an inward axial flow.

Secondly, the model was used to investigate the effect of geometry and ambient gas-fraction on the performance of annular DBD actuators at different scales. It was found that by increasing the local production of ions, both increasing the oxygen gas-fraction and reducing the exposed electrode thickness increased the discharge intensity during the positive part of the cycle.

Finally, a sub-millimetric parallel actuator was also examined. The applied voltage frequency was varied to induce different magnitude streaks in a boundary layer flow over a flat plate. Such a design could be used to control individual streaks via antagonistic superposition.

Acknowledgements

I would like to thank my supervisors Dr. Xuerui Mao and Prof. Kwing-So Choi for all their hard-work, guidance, and patience. They provided me with a strong direction throughout my PhD, providing invaluable experience and advice. I would also like to thank Dr. Dandan Xiao, for her helpful assistance.

I would also like to thank Prof. Francois Rogier for giving me a fantastic opportunity to travel to Toulouse and work with the great people at ONERA. The experience was invaluable. I must also thank Dr. Konstantinos Kourtzanidis, whose help and experience was irreplaceable.

I must also thank my family, for their tremendous understanding and encouragement. I would particularly like to thank my Dad for the hours of proof reading.

Finally, I would like to thank Francesca for sticking by me over the last four years. She has been my rock and inspiration, and I could not have done it without her.

List of Publications

1. *"Flow Reversal in Millimetric Annular DBD Plasma Actuators"*, **Huw Borradaile**, Konstantinos Kourtzanidis, Francois Rogier, Kwing-So Choi and Xuerui Mao (submitted for publication in the Journal of Applied Physics)

2. *"Bypass Transition Induced by DBD Plasma Actuation"*, Dandan Xiao, **Huw Borradaile**, Kwing-So Choi, and Xuerui Mao (under preparation).

Contents

List of Tables

List of Figures

Chapter 1

Introduction

1.1 Motivations

In 2019, the commercial aerospace sector emitted 918 million tons of carbon dioxide (CO_2), an increase of 29% since 2013 [1]. In addition, the combined transport sector is the fastest growing contributor of global greenhouse gas emissions [2], and already accounts for about one-quarter of global emissions and half of global oil consumption [3]. Even modest improvements in efficiency can therefore have a significant global impact. A 1% reduction in drag on a typical jet airliner in cruise conditions would reduce the CO_2 emitted by the aerospace sector by nine million tons per year by 2030 [4]. As a vehicle's design geometry is often heavily constrained by operational requirements, there has been significant research efforts in the development of flow control devices, the addition of which can reduce drag without significant changes to the design.
Over the last two decades, Dielectic Barrier Discharge (DBD) actuators have become one of the most exciting areas of flow control research, with several key advantages over other methods of flow control. Firstly, these actuators are fully electronic devices with no moving parts, allowing for a higher level of control. Secondly, control responses can be implemented in real time, potentially as part of a closed loop control system allowing a system to continuously operate at an optimal operating condition. Their electronic nature allows DBD

actuators to be one of the most flexible forms of flow control, able to operate in a variety of different control regimes, and to switch between regimes rapidly, without wasting unnecessary energy on deployment. There are many mechanical benefits too: DBD actuators are low in mass and volume, which can be attached to a surface without the addition of large cavities or holes which can lead to a significant reduction in structural strength. They are also low maintenance with quick and simple installation and replacement requirements. Crucially, they also have an extremely low power consumption, typically $\sim 1W/cm$ for continuous operation [5], with effectivenesses (the ratio of power saved by applying the control to the power consumed by the control) of over 1000 being recorded for periodic forcing [6]. One of the most promising advantages of DBD actuators is their ability to be readily manufactured into millimetric (even microscale) devices. In principle, this provides the opportunity to directly control both milli and microscale coherent structures and transition modes resulting in a distributed active control with an unprecedented efficiency and effectiveness. At present DBD actuators probably represent the only active control method that can be implemented in this way without a prohibitive cost.

However, despite recent developments, DBD actuators have only been able to produce relatively modest flow velocities of up to 10 m/s [7]. This means that they are ineffective at directly injecting momentum into the higher velocity flows particularly relevant to the transport sector. Nevertheless, progress has been using DBD actuators' limited control effect to destabilise and restabilise the boundary layer of such flows. It has been shown that DBD actuators can effectively "trip" the flow generating streamwise vortices which can delay transition and prevent detachment in these high velocity flows [8]. If the coherent structures within a transitional boundary layer could be manipulated with small, well-timed, and highly localised forcing, the boundary layer could be destabilised and/or restabilised far more effectively and with greater versatility. To implement such a control, a better understanding of how DBD

actuators perform at this scale is needed.

DBD plasma actuators induce flows by ionising the air over the surface, which then experiences an electrohydrodynamic (EHD) force from an electric field. However, experimental investigations of DBD actuators are limited by both their temporal and spatial resolutions, meaning we must rely on accurate numerical models to understand the detailed mechanics of the discharge. The accurate numerical modelling of the complete discharge process is complicated. There are a multiplicity of different ions generated, each governed by their own transport equation, resulting in a very large system of coupled partial differential equations (PDEs). On top of this, the ions interact with each other in a chain of very fast (nanoscale) chemical interactions, crucial parameters of which are difficult to determine, often relying on simplistic empirical approximations. However, recent developments in plasma modelling, as well as increasing computing power, have made it increasingly feasible to solve a reduced plasma model over a sufficient and representative time period.

In this study, a sophisticated 4-species plasma-fluid model will be used to investigate the performance of DBD plasma actuators on the millimetric scale. Using this method, we hope to provide useful physical insight into the underlying mechanisms, as well as the resulting performance of such small scale actuators, bringing us closer to a distributed small-scale control system.

1.2 Aims and Scope

This work will use the 4-species plasma-fluid model to investigate the mechanics underpinning millimetric plasma actuator behaviour, which is a length scale where phenomenological and empirical models fail to generate accurate predictions. Chapter 1 will review the current literature in this multidisciplinary field, and provide a relevant background. Chapter 2 will detail the numerical schemes used during the investigations, as well as their limitations and scalability. Chapter 3 will investigate and explain an interesting and unexplained flow

reversal phenomenon in millimetric annular DBD actuators. Chapter 4 will present a performance parameter study for millimetric annular DBD actuators, illustrating how this flow reversal phenomenon can be controlled by the variation of oxygen gas fraction and exposed electrode thickness. Finally, Chapter 5 will investigate another configuration of millimetric DBD plasma actuators: the linear synthetic jet. Here we will demonstrate a proof-of-concept implementation to control individual boundary layer streaks and thereby control the transition from a laminar to a turbulent boundary layer.

1.3 Review of Plasma Mechanics

1.3.1 The Plasma State

There are five states of observable matter: solid, liquid, gas, plasma and Bose-Einstein condensates. Of these, plasmas make up 99% of observable matter in the universe. Plasmas are found in phenomena such as the Northern Lights, lightning, and the stars. This state is reached when a gas is ionised to such a degree that the electromagnetic interactions between ions dominate over the random motion of gas particles. As a result plasmas self-organise, respond to electromagnetic fields and can conduct electricity.

Energy is required to ionise a gas molecule, and this can be supplied by either a collision with a high-speed electron, or an interaction with a photon. To ionise the required fraction of a gas to generate a plasma, either the mean kinetic energy of electrons must be significantly increased, or an enormous quantity of photons must be generated. In many situations increasing the mean kinetic energy of electrons is more practical, and can be achieved in two ways. Firstly, the addition of thermal energy to the gas will raise the mean kinetic energy of both ions and electrons. Relatively high temperatures ($> 5000K$ for air [9]) are required for ionization to be achieved this way. Alternatively, a strong electric field can be used to accelerate free electrons, present in the gas from ambient

photo-ionisation, until they achieve the required kinetic energy for ionisation. For air, ionisation can be achieved at room temperature with an electric field strength of $\sim 3MV/m$. Plasmas are generated from neutral gases, and each ionisation event produces the same number of positive and negative charges, they are therefore described as quasi-neutral.

Plasmas generated by heating the gas, and those generated by electric fields are categorised as "thermal" and "non-thermal", respectively. However, the thermal and non-thermal categorisations refer to whether the plasma's constituent parts exist in thermal equilibrium, and not the method of ionisation. Denoting the electron, ion, and neutral temperatures as T_e, T_i and T_n, respectively, a thermal plasma is defined as when $T_e \approx T_i \approx T_n$, whilst for a non-thermal plasma $T_e \geq T_i \approx T_n$. The difference in mass between electrons and ions (4 orders of magnitude) ensures there is limited energy exchange between the electrons and heavy particles. This allows a non-equilbrium to be maintained for a long time. Non-thermal plasmas are generally preferred for aerodynamic applications as they can be generated with less input energy, as energy is not required to heat the heavy gas molecules. They can also be implemented more precisely, and less destructively, with limited effects on the thermodynamic and chemical profile of the flow. However, thermal plasmas are still sometimes used in hypersonic flows to mitigate shockwaves [10]. A Dielectric Barrier Discharge (DBD) is a type of non-thermal plasma, and so is characterized by low gas temperatures and rapid chemical interactions.

1.3.2 The Gas Discharge

Neutral gases are insulators, whereas the charged species present in plasmas make them good conductors. When a large potential difference is applied across a gas, it can lead to formation of a conductive non-thermal plasma. Once a plasma is formed, a current will develop and will persist until the potential difference is quenched. This process and the resulting behaviour of a

neutral gas being converted to a conductive plasma is called a gas discharge. Depending on the gas properties, electrode configuration, and applied voltage, different discharge regimes can be observed.

There are two types of current which can be used to quantify the discharge intensity and thus the discharge regime: these are the conduction and displacement current [11]. Firstly, the conduction current $\boldsymbol{J_C}$ describes the movement of charged species

$$\boldsymbol{\nabla} \cdot \boldsymbol{J_C} = -\frac{\partial \rho_c}{\partial t} \tag{1.1}$$

where ρ_c is the charge density. The displacement current $\boldsymbol{J_D}$, on the other hand, results from changes to the electric field,

$$\boldsymbol{J_D} = \frac{\partial(\varepsilon \boldsymbol{E})}{\partial t} \tag{1.2}$$

where $\boldsymbol{E}$ is the electric field, and ε is the permittivity. This is sometimes referred to as the capacitative current in literature.

All gas discharge regimes commence with the transition from a gas to a non-thermal plasma. This process is often sudden and chaotic and is referred to as breakdown. Breakdown occurs because the ionisation process generally leads to the formation of free electrons which in turn increase the rate of ionisation. This ensures breakdown processes are exponential, sudden and dramatic. The mechanics of this process can vary significantly depending on a variety of factors, particularly the reduced electric field strength $\boldsymbol{E}/N$, where N is the number density of neutral particles. This parameter is easily measurable and can be used to give a good approximation of the mean kinetic energy of electrons, as $\boldsymbol{E}$ scales with the energy gained by electrons between collisions, and N scales with the collision frequency. It therefore follows that breakdown can be more readily achieved at lower pressures, whereas at higher pressures a stronger electric field is required.

Once conditions for breakdown have been met, and the ionisation of the neutral gas occurs, the first observable discharge regime is the Townsend discharge,

characterised by its low-current and transient behaviour, and is discussed in more detail in §1.3.3. At low pressures, the Townsend discharge quickly develops into a glow discharge, so named because they radiate photons in the visible range. At higher (atmospheric and above) pressures, the equivalent of the glow discharge is the corona discharge. Whilst similar, the corona discharge differs due to the radiated photons producing additional free electrons via photoionisation. However, as this photoionisation effect can be small and is difficult to model it is often neglected.

At sufficiently high $\boldsymbol{E}/N$ the streamer regime is observed. Here the high levels of ionisation result in a strong local electric field leading to a complicated 3D spatiotemporal structure discussed in more detail in §1.3.3.

If an even larger voltage is applied then a spark breakdown can occur, and the plasma forms a constricted arc with a high conductivity. Acting as a closed circuit, the high current and correspondingly high temperatures often result in damage to the local environment and electrodes. A spark breakdown can be avoided by the strategic placement of a dielectric barrier between the electrodes as explained in §1.4.

1.3.3 Ionisation Regimes

Townsend Breakdown

The Townsend breakdown is often referred to as the electron avalanche. It is initiated by free electrons being accelerated by an applied electric field. These free electrons are present due to photoionisation and background radiation, and are repeatedly recombining with positive ions in a process called attachment. If these electrons achieve a sufficient kinetic energy prior to a collision with a neutral particle, an ionisation event will occur. This ionisation event will split the neutral particle into a positive ion and an additional free electron. Both the original and new free electrons are accelerated by the applied electric field until they achieve enough kinetic energy for another ionisation event.

The breakdown voltage V_{br} is the voltage required to generate a sufficiently strong electric field that the mean acceleration of free electrons between collisions is enough to generate more than one ionisation event in it's life-time. Once this threshold is reached, due to the rapid number of collisions and the high speed of the free electrons, there is a rapid exponential growth in the number of free electrons and ions. As charged species, these free electrons and ions are driven by the applied electric field resulting in a current.

If there is a sufficiently strong electric field, the directed species will release further free electrons from material surfaces they collide with, in a process called secondary electron emission. Understanding and modelling the mechanics of this process is an active area of research, and is often difficult to quantify.

Streamer Breakdown

If the reduced electric field $\boldsymbol{E}/N$ is sufficiently high, the local ionisation leads to the formation of a significant space charge modifying the local electric field. It was this local field distortion which Meek et al [12] determined as responsible for the 3D structure observed at high $\boldsymbol{E}/N$.

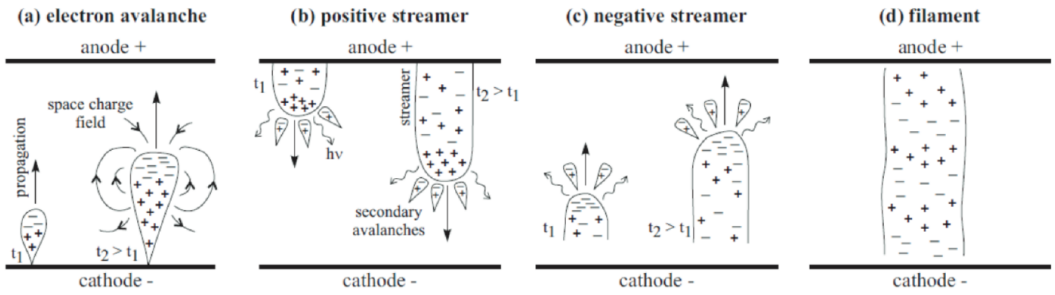

Figure 1.1: *Formation of a streamer [13]*

After the initial avalanche, the slow moving positively charged ions are left behind, as the electrons are absorbed into the anode as illustrated in figure 1.1(a). Due to the high rate of ionisation these positive ions induce a strong positive electric field. This accumulation of positive charge acts like a virtual anode absorbing free electrons and inducing additional ionisation. As electrons are absorbed and driven towards the anode, a current flows through this struc-

ture, whilst the additional ionisation ensures a high density of positive ions at the head of the structure. Progressively, this streamer crosses the gap led by a high density of positive ions, and is therefore called a positive streamer. This is illustrated in figure 1.1(b).

At sufficiently high voltages, the high number of free electrons from the Townsend breakdown generate a large local space charge before they can be absorbed into the anode. In this case, as the free electrons propagate towards the anode, leaving the slow-moving positive ions behind, a difference in potential is generated leading to increased ionisation. This process is self-repeating and this structure quickly crosses the gap. As the head of the structure is negatively charged, it is called a negative streamer, and is illustrated in figure 1.1(c).

Due to their local self-propagating nature, both positive and negative streamers cross the gap very quickly ($O(ns)$), resulting in narrow channels of charged species. Due to these rapid timescales, individual streamers are not easily visible to an experimental observer. However, as the residual ions and free electrons encourage subsequent streamers to follow the same path, the discharge appears to the naked eye as a large number of semi-static luminous filaments, and as such is referred to as a filamentary discharge.

1.4 Review of DBD Plasma Actuators

DBD actuators were first introduced by Roth et al. [14] as an alternative to magnetohydrodynamic control, a form of flow control used for supersonic flight, but with the option that they can be used for low speed applications. In this paper, they showed the potential of DBD actuators to suppress separation over an aerofoil and thereby increasing the stall angle and aerodynamic performance, all the while operating at low power levels due to the absence of large currents.

This breakthrough paper led to a flurry of interest in DBD actuators, as the field recognised the potential of a robust, low cost, and effective active flow

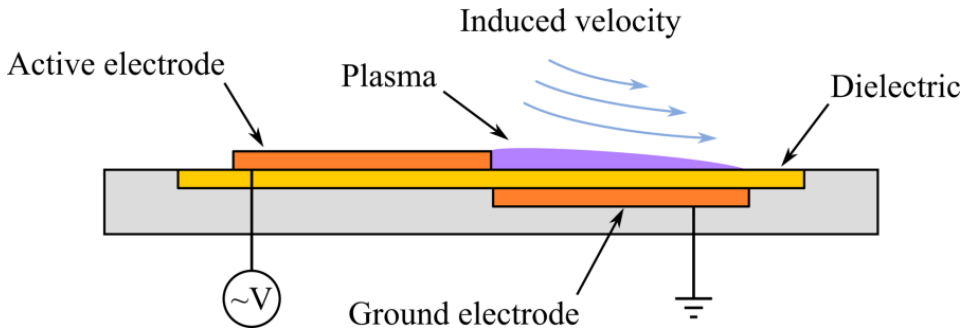

Figure 1.2: *DBD plasma actuator schematic [15].*

control method. Over time the name for Roth's device changed from One Atmosphere Uniform Glow Discharge Plasma (OAUGDP) actuator to the more generic Dielectric Barrier Discharge (DBD) actuator.

Whilst the precise design and layout of DBD actuators does vary, a typical configuration is shown in Figure 1.2. It consists of two electrodes one exposed to the flow, the other which is slightly downstream is covered in a dielectric barrier. The dielectric barrier is essential to ensure that the discharge is self-limiting, keeping the current and correspondingly the power consumption low. When the control is being used to reduce form drag, typically an AC voltage in the order of 3-20 kV and a frequency of approximately 1-10 kHz is applied across both electrodes. This leads to the formation of an ion cloud, which experiences an electrohydrodynamic force due to the asymmetric electric field and is accelerated downstream. There is momentum transfer between the charged particles and the neutral atoms, due to the high number of collisions, leading to the acceleration of the neutral boundary layer. However, this explanation is incomplete as experimental observations have described the plasma discharge having a macro-scale spatial and temporal structure. To develop more effective actuators it is important to understand the inner workings of the discharge in depth.

Dielectric materials, from which this actuator gets it name, are electrical insulators with polar molecules. When placed in an electric field, these molecules store electrical energy. In the DBD actuator design, a dielectric material is placed between a pair of electrodes with a potential difference high enough to

induce a gas discharge. The charged species in the gas discharge are driven towards and deposited on the surface, building an opposing potential. Eventually this opposite potential will reduce the applied electric field terminating the discharge. This is useful, because if the electric field strength was not reduced, the current (and thus power) would continue to increase exponentially leading to the transition to the power-hungry and damaging arc discharge [16]. However, to allow for a continuous discharge the applied electric field has to be continuously increased. This is obviously impractical for longer time periods. It is therefore most common for an alternating voltage to be applied. Usually, this applied voltage in sinusoidal but a number of other voltage profiles have been investigated [17].

The key properties of the plasma discharge have been observed and measured experimentally. In all cases, it was found to be a very weak plasma, with ion concentrations of the order of 1ppm[18]. It was also found that, as the plasma is generated by ionising neutral air, the resulting plasma is predominately quasi-neutral. An exception is when an electrostatic sheath is present, which has a greater density of positive ions, and hence an overall excess positive charge. Electron temperatures have been measured at 10000K [19] but there is an order of magnitude difference between the electron temperature and the ion temperature and therefore this plasma is not considered thermal.

The most important feature of the DBD actuator is that it can sustain a large-volume discharge at atmospheric pressure without the discharge collapsing into a constricted arc[20]. This keeps the currents crossing the gap small, and not only does this prevent damage to the dielectric and unnecessary heating, it keeps the power consumption low. Crucially a constricted arc means a smaller forcing volume, therefore the addition of a dielectric barrier allows for the body force to be distributed over a larger volume and more momentum to be injected into the boundary layer.

Since Roth et al.'s original work, the potential of a MEMS-style active massless flow control was quickly realised, even whilst the mechanism and structures

underpinning the discharge were not fully understood. Subsection 1.4.1 reviews the key discoveries and progress in understanding the discharge mechanics of a DBD actuator. The current understanding of how the EHD force is induced is covered in subsection 1.4.2. Finally, subsection 1.4.3 covers the progress in using this physical insight to develop simplified models to predict actuator performance.

1.4.1 Discharge Mechanics

The early work undertaken to reveal the mechanism behind DBD actuators was all experimental. Enloe et al. [20], used an experimental photomultiplier tube to observe that there were periods of the cycle where no ionisation occurs. More precisely, they concluded that the plasma was non-uniform but rather consisted of a series of microdischarges and streamers occurring in quick succession. They also observed an asymmetry between the discharges during the positve and negative subcycles.

This was confirmed by Orlov et al. [21] using a photomultiplier-tube output phase locked with the AC input to the actuator to generate an accurate time-series. It was found that there were clear differences in discharge structure of the positive half-cycle and the negative half-cycle. It was also noted that the light emission consisted of a series of numerous narrow peaks, confirming the presence of numerous intermittant microdischarges.

In 2010, Corke et al. [18] proposed that the difference in discharge structure of the positive and negative half-cycles, was due to the source of electrons. It was suggested that during the negative half-cycle the exposed electrode supplied a consistent source of electrons, whilst during the positive half-cycle, the electrons have to be sourced from the negatively charged dielectric which due to its surface chemistry doesn't release them so readily. Boeuf modelled the discharge asymmetry in 2007 [22]. This was one of the earliest fluid numerical models. However, due to the limited computation power, it assumed a pure

nitrogen mixture and only modelled two species: electrons and positive ions. However, this was an important development as most experimental investigations are limited to a sampling frequency of $O(\mu Hz)$, clearly limiting their ability to visualise individual microdischarges of $O(1ns)$.

Around the same time Likhanskii et al. [23] indicated the important role of negative ions in an atmospheric discharge using a 4-species fluid model. Another numerical model developed by Boeuf et al. [22] showed that for both a ramp and a sine voltage, the discharge consisted of diffuse low current corona discharge interrupted by the formation of intense streamers. They found that the contribution of the low current phases is dominant because the force acted over a much longer time period and larger volume than the more intense streamers.

1.4.2 Force Generation

As stated, there are two periods of activity during the AC cycle of a DBD plasma actuator. These are the positive-going positive part and the negative going negative part. These are termed the positive and negative discharge (or the forward and backward stroke) respectively. The continually increasing potential difference during these periods prevents the accumulated charge on the dielectric surface from quenching the discharge.

There are distinct differences in the discharge structure of the positive and negative discharges, which can be clearly seen in experiments [21]. The positive going cycle has a series of corona discharges, transitioning to the streamer regime if a significantly high voltage is applied. The negative discharge cycle is characterised by multiple successive microdischarges. The highly mobile electrons rapidly charge the dielectric, resulting in the rapid quenching of the discharge, and thus repetitive extinction and formation of the plasma volume. The plasma volume and the forcing volume are significantly reduced during the negative discharge. This is serendipitous as the assymmetry of these discharges

leads to the formation of a resultant force.

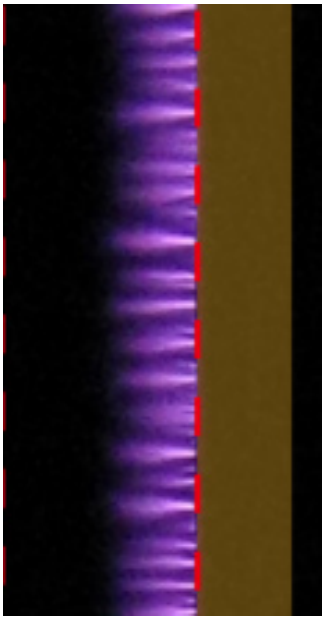

Figure 1.3: *Plasma Streamers [24]*

If a sufficiently high voltage is applied that a streamer regime is observed, the plasma volume is reduced and the current density increases. A typical streamer regime is shown in figure 1.3. This increased current rapidly charges the dielectric, ensuring the streamers exist over short timescales. Boeuf et al. determined that, because of this, the majority of the force is generated by the corona discharge between the formation of streamers [22]. It was later determined that the high current also leads to most of the energy being dissipated as heat, resulting acoustic waves and a reduced efficiency [25]. In order to achieve maximum efficiency, it is sensible to avoid the streamer regime by using lower applied voltages and frequencies. Streamers can also propagate far from the exposed electrode [5], which for millimetric actuators can be detrimental to the design, even though the increased propagation of streamers will be limited by the length of the dielectric. In this case, the utilisation of low applied voltages to avoid the transition to the streamer regime is therefore preferred.

Regardless of the mode of operation, all AC-DBD actuators utilise the same mechanism to induce a force into the boundary layer. A high voltage is applied across electrodes leading to breakdown and the generation of a gas discharge.

The newly formed charged species in the plasma volume are accelerated by the strong applied electric field. An asymmetrical electrode configuration, is used to direct this drift away from the exposed electrode edge. The collisions between these directed charged species and neutral fluid molecules lead to momentum transfer to the fluid, resulting in an apparent induced electrohydrodynamic (EHD) body force $\boldsymbol{F}$ which can be calculated as

$$\boldsymbol{F} = e\boldsymbol{E}(n_p - n_e - n_n) - \sum_{k=e,n,p} \boldsymbol{\nabla} k_b T_k n_k \tag{1.3}$$

where the subscripts p, n, and e refer to the positive ions, negative ions and electrons respectively, n indicates the species' number density, and T their temperature. $\boldsymbol{E}$ is the applied electric field, and k_b is the Boltzmann constant [25–27]. The forcing distribution is multidimensional, and even though two actuators generate the same resultant thrust, they might generate different flow features.

Equation 1.3 can be split into the first and second terms which are the advective and diffusive terms, respectively. The advective term decribes the drift of charged species due to the applied electric field, whilst the diffusive term describes the migration of particles due to concentration gradients. In general, the advective term greatly exceeds the diffusive term, with ratios of over a 1000 being reported. The diffusive term is therefore often neglected, and there is often strong agreement between the electric field lines and the instantaneous motion of the charged species.

Whilst there is good consensus that the positive discharge generates positive forcing away from the exposed electrode, there is conflicting evidence and results regarding the direction of the forcing during the negative cycle. A number of papers [28–30] observe a PUSH-pull behaviour (the capitalisation indicates the magnitude of the forcing) with the negative cycle behaving antagonistically, . However, PUSH-push forcing has been reported by [31–33] describing a positive contribution of the negative ions during the negative cycle. The

differences in configurations and experimental set-ups make it difficult to precisely understand this discrepancy. However, it seems that at higher voltages the contributions of the negative ions become increasingly important, and can propagate along the surface during the negative discharge leading to a large plasma volume and a significant assistive force away from the exposed electrode. More recently, Kourtzanidis et al. [34] have shown that there are often regions of both positive and negative forcing components during the negative half-cycle, and the location of the velocity measurement is important.

1.4.3 Performance Modelling

The experimental and computational studies described above provide an understanding which can be used to develop a simplified model or framework which allows the performance and behaviour of DBD actuators to be quickly and accurately predicted.

Several studies have focused on how actuator performance scales with key input parameters. For example Pons et al. [35] found a relationship between the electrical power and a range of parameters. The method consisted of placing a capacitor between the grounded electrode and earth, and plotting the V–Q curve. The consumed power was found to be proportional to $V^{3.5}$. Thomas et al. [36] also found that the induced thrust was also proportional to $V^{3.5}$ and directly proportional to the input power. A caveat, found much earlier by [20, 37] showed that, with increasing AC amplitude, the maximum velocity induced by the plasma actuator was limited by the area of the covered electrode. Thus the dielectric area needed to store charge can be too small to take full advantage of the applied voltage.

1.5 Review of Flow Control

Flow control refers to the modification of the flow field by either passive or active means. It is an important field in fluid dynamics due to its numerous

applications in many industrial sectors, and because the geometry of a design is often dictated by other considerations.

There is an extensive variety of different flow control methods that are used to manipulate the flow to achieve different desired effects. The majority of these methods are used to reduce drag of one form or another. For subsonic flows, the drag behind a body can be categorised as either form drag or skin friction drag or usually some combination of the two. Form drag is caused by boundary layer separation leading to a low pressure region behind the body, whereas skin friction drag, sometimes called viscous drag, is caused by the viscous shearing of the fluid at the surface. It is possible to divide these drag reducing flow control methods into two groups depending on whether they reduce form drag or skin friction drag.

Flow control devices designed to reduce form drag, do so by delaying boundary layer separation. This is important for bluff bodies, with larger effective diameters, where the likelihood of separation is high. If separation occurs along a significant proportion of the surface at atmospheric conditions, form drag is likely to dominate over the skin friction term, due to air's relatively low viscosity. To delay separation, flow control methods look to increase the flow velocity near the wall. This can be done by directly injecting momentum into the boundary layer for example with blowing, a moving surface, or a DBD actuator. Suction can also be used to remove the low velocity boundary flow, resulting in a net increase of the average velocity near the wall . Alternatively, vorticity can be generated to mix the boundary flow with the higher momentum freestream, which also increases the near wall velocity. This is a common method used in the aerospace industry, as it can be implemented passively with the addition of small protrusions on the surface. These methods increase the skin friction as they increase the velocity gradient at the wall.

On the other hand, flow control methods designed to reduce skin friction drag do so by suppressing the boundary layer's transition from a laminar state to turbulent one. This is effective as laminar boundary layers have a significantly

lower shear rates than their turbulent counterparts, and is particularly important for large streamlined bodies like trains or aeroplanes. To achieve this passively, the surface roughness is often reduced as this is the key controllable factor that results in early transition. Painting, using flush rivets and waxing are the most common ways this is implemented.

On the path to turbulence, a laminar boundary layer will pass through several different modes characterised by distinct coherent structures. Whilst boundary layer transition is still very much an active area of research, several methods rely on suppressing specific transition modes. This forces the flow to transition through less energetic modes which takes longer. The dominant transition mode depends on the structure of the boundary layer. For a 3D boundary layer which usually transitions through cross-flow instability, it has been shown that generating spanwise waves in the boundary layer is effective at suppressing turbulence generation, and delaying transition. This has been effectively achieved with annular DBD actuators [38].

It is also possible for these flow control methods to be split into passive flow control methods and active flow control methods. A passive flow control is defined as a method that requires no external power input, for example, it gets all its power from the flow field itself. This typically reduces maintenance and design costs but also restricts the amount of alteration to the flow field that can be achieved, as well as their operational flexibility. Active flow control methods require an external power source which increases their complexity and cost, but allows for a far less limited range of operation. Active flow controls have been used to generate lift coefficients (C_{Lmax}) of over 10 [39] whereas the typical maximum achieved by a passive control is 3.5.

It is often useful to dynamically run a flow control method under different regimes to achieve different effects depending on how the device is being utilised at that moment, for example, ailerons on the wing of an aeroplane are altered to increase or decrease their lift and correspondingly bank the aircraft. This can sometimes be achieved with passive controls but usually there is an active

energy consumption to change the regime. It is easier to make a dynamic active control, as by definition the input power is externally provided and therefore can be regulated.

A flow control system is like any other control system, in that they are trying to operate at an optimal condition, where the maximum energy saving can be achieved with the minimum energy expenditure. However, as the initial flow field is variable it is impossible to have the control system operating at this optimal condition all of the time, without a feedback loop. This is called a closed loop control system and a flow control system can be designed that adjusts itself to maintain an optimal operating condition. This is clearly preferable to a design which over or under compensates and leads to inefficiencies. Unfortunately to develop an effective closed loop control system there must be a very fast response time between the sensor and the actuator otherwise it will constantly overshoot the desired operating condition. This fast response time depends on the mechanics of the actuator and also the interfacing between the sensor and the actuator.

1.6 Laminar to Turbulent Transition

Fluid flow can exist as either laminar or turbulent, depending on whether the non-dimensional ratio of inertial and viscous forces exceeds a critical value. In fluid dynamics, laminar flow is characterized by smooth movement of regular fluid layers, with very limited mixing between layers. In contrast turbulent flow is characterized by agitated and irregular mass flow, which enhances the kinetic energy mixing. Due to this intense mixing a turbulent boundary layer has a steep gradient of velocity at the wall and therefore a large shear stress and high skin-friction.

Overcoming this increased drag is a significant cost in a wide variety of sectors. Skin-friction drag accounts for about 60% of the total drag of a modern airliner at cruise. “A 1% reduction in drag on a jet airliner in cruise condi-

tions translates roughly to a 0.75% reduction in fuel consumption, implying a potential reduction in emitted CO_2 of nine million tonnes [per year] per 1% drag reduction" for the aerospace sector [4]. "A 1% drag decrease corresponds approximately, to a 5 - 10% increase in payload" [40].

The transition from a laminar boundary layer to a turbulent one is a complicated process, and has been an active area of research since at least 1883 [41]. However, there have been a number of recent advances in the field, as the development of high-performance computing has allowed high resolution direct numerical simulations (DNS) to examine all scales of the flow, leading to a number of recent discoveries in this field. Nevertheless, the computational cost of these investigations is still large enough to limit them to relatively simple flows, and there are still a number of significant unsolved problems [42].

The transition process can be broken down into a number of stages. Firstly, small perturbations and eddies present in the freestream induce disturbances into the boundary layer profile. This stage is often described as the receptivity phase. These disturbances either grow in magnitude or decay within the boundary layer, depending on the stability of the boundary layer profile. However, the large variety of potential disturbances combined with the diversity of boundary layer profiles, lead to a very large number of transition modes. This problem is compounded as the induced unstable flow structures can interact, developing secondary instabilities and complicated breakdown phenomena.

Despite this, it is common to categorised boundary layer transitions into two modes. All modes which can be described by linear stability theory [43, 44] are classified as "Classical" or "Natural" transition. Whilst those which do not are classified as "Bypass" transition.

1.6.1 Classical Transition

Tollmien and Schlichting were the first to examine the stability of the laminar boundary layer via linear stability theory [43, 44] . They demonstrated how solutions to the linearized Navier stokes equations could be found, by examining the maximal sensitivity to small perturbations. Exponentially growing solutions can be identified, and these so-called "primary" instabilities in the laminar boundary layer are excited by weak perturbations in the flow, eventually becoming energetic enough to generate spanwise secondary instabilities. The nature of the dominant boundary layer instability depends on the geometry of the flow field. Below we describe two common instabilities: Tollmien–Schlichting (T-S) waves and cross-flow instability. These instabilities are the primary method of transition in a number of practical applications. They are also suppressed and controlled with active and passive methods of flow control. A mathematically rigorous description of these and other primary instabilities can be found in works by Schlichting et al. [45], White et al. [46], or Schmid et al.[47]. Tollmien–Schlichting (T-S) waves are often the dominant instability found in two-dimensional (2D) bounded shear flows such as boundary layer and channel flows, which are some of the most studied areas in fluid mechanics, and T-S modes often dominate the transition of these flows. These instabilities can be identified as spanwise vortices which propagate downstream and grow in size and magnitude as shown in figure 1.4. According to linear stability theory these grow exponentially, eventually leading to the development of a secondary instability as a three-dimensional spanwise modulation of the T-S waves resulting in a fully turbulent boundary layer.

Meanwhile, the cross-flow instability is found in 3D boundary layers such as those found on swept wing aircraft, or rotating structures [49]. This inviscid instability is inherent in the boundary layer profile [50]. The dis-alignment of the pressure forces and the streamwise direction lead to a surface flow perpendicular to the free-stream. It is this perpendicular "cross-flow" which gives the

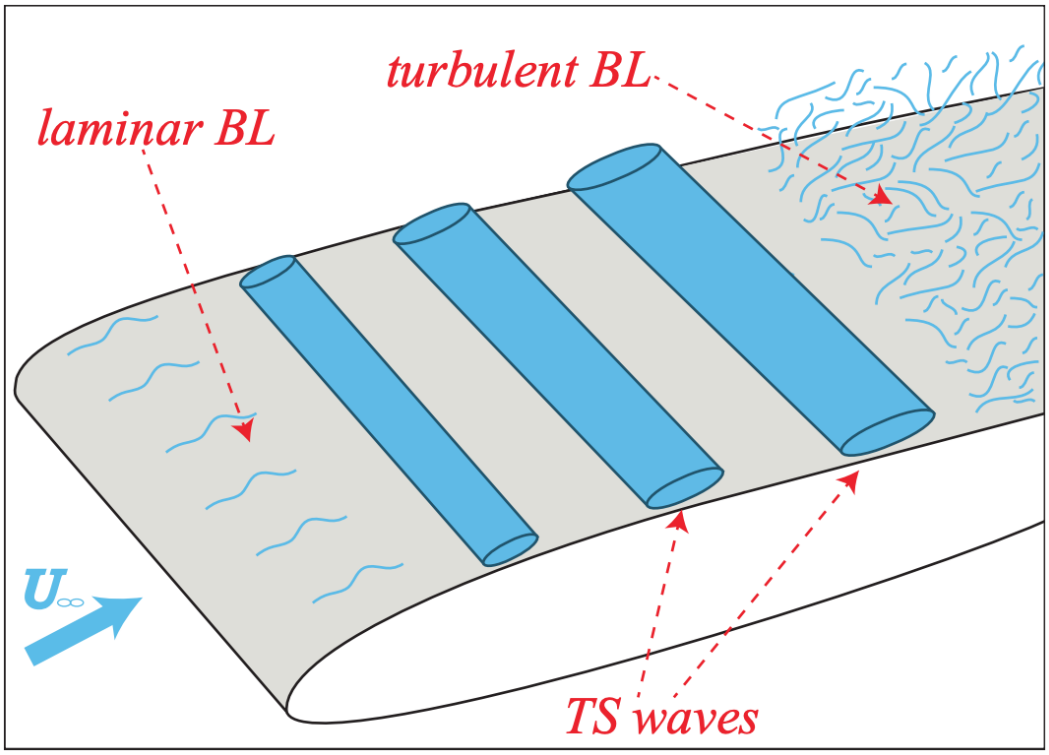

Figure 1.4: *Schematic of a classical boundary-layer transition characterized by the secondary instability of Tollmien-Schlichting waves [48]. (BL = boundary layer, and TS = Tollmien-Schlichting).*

instability it's name. This change of direction in the low-speed, near surface flow leads to an inflection point in the boundary layer profile, and consequently the formation of weak vortices. These vortices destabilise the mean flow, and develop spanwise shearing modes eventually leading to turbulent breakdown.

1.6.2 Bypass Transition

It was found that linear stability theory was a poor predictor of transition of energetic flows, which would often breakdown to turbulence earlier than predicted by linear stability theory [51]. For some flows the experiments observed transition, even when linear stability theory predicted a stable flow at at all Reynolds numbers [52, 53]. The seminal work on addressing these discrepancies was undertaken by Klebanoff et al. [54] (and later expanded on by Kendall et al. [55, 56]) which gave physical insight into a boundary layer undergoing early transition when the boundary layer was agitated by unsteady forcing. Klebanoff et al. identified that the majority of the energy with the bound-

ary layer was in the low-frequency spectrum, with the maximum energy near the middle of the boundary layer, a key discrepancy compared to the classical transition mode.

Eventually a working understanding for these cases was proposed by Ellingsen et al. [57] and later expanded on by Landahl et al. [58]. These works described how alternating low and high velocity streamwise streaks could develop allowing for the more rapid development of instabilities than the exponential growth of T-S waves described under the linear stability theory. The growth of these disturbance is called non-linear transient growth.

Bypass transition has become a loose term to describe this form of transition, as it "bypasses" the linear range of the exponential growth of the small disturbances, thus leading to a more rapid transition. It has been found that Bypass transition is predominant form of transition for many practical applications (e.g. turbomachinary), and can be induced by strong free stream turbulence, surface roughness or by surface impulses [59].

Strong free-stream turbulence leads to one of the most complicated transition processes. When the boundary layer is subject to free stream turbulence, streaks are formed as a result of the low frequency disturbances entering the boundary layer via shear sheltering [60]. These streaks can be present in classical transition, bypass transition and indeed turbulent boundary layers, but play a key role in Bypass transition. Swearingen et al. identified two forms of secondary instability leading to the breakdown of streaks: a sinuous type and a varicose type [61]. Whilst Andersson et al. [62] showed how both these secondary instabilities originated from the interaction with the free-stream turbulence. The sinuous mode is associated with the spanwise in the cross-sectional velocity profile and features an asymmetric pattern with respect to the unstable streak, whereas the varicose one is related to the wall-normal in inflection point and presents a symmetric pattern. Matsubara et al. analysed the behaviour of the streamwise streaks more closely indicating how the spanwise size of the structures followed the boundary-layer thickness [63]. For

a more thorough review of the effects of free-stream turbulence on boundary layer transition, the reader if referred to the recent review by Fransson et al. [42]

1.7 Turbulent Boundary Layer Structures

Turbulent flows are complex, multi-scale, and chaotic, but can still be characterised by considerable structure. Recurring characteristic structures present in many different flows are collectively termed coherent structures. A precise definition of coherent structures does not exist, although a loose one is provided by Robinson et al. [64]:

"It is a three-dimensional region of the flow over which at least one fundamental flow variable (velocity component, density, temperature, etc.) exhibits significant correlation with itself or with another variable over a range of space and/or time that is significantly larger than the smallest scales of the flow."

Despite this, coherent structures have become one of the most researched areas of fluid mechanics, with hundreds of structures being identified and characterised. Most of these structures are large but are generally composed of fundamental building blocks such as streaks and hairpin vortices. In this section the formation and mechanics of these two crucial flow structures and their breakdown are reviewed.

The first coherent structures to be formally identified were streaks by Kline et al. in 1967 [65]. They were described as long, thin, streamwise structures, with a consistent streamwise velocity. The scale of these streaks are surprisingly consistent, with a width of 20, and a length of upto 1000 viscous units (one viscous unit $= \nu/u^*$) [66, 67]. The formation of streaks is attributed to counter-rotating streamwise vortices in the near-wall region [68]. These vortices drag high momentum fluid from the upper boundary layer and low momentum fluid from the lower boundary layer into the gaps between vortices. This generates alternating high and low-speed streaks as shown in figure 1.5. Whilst the

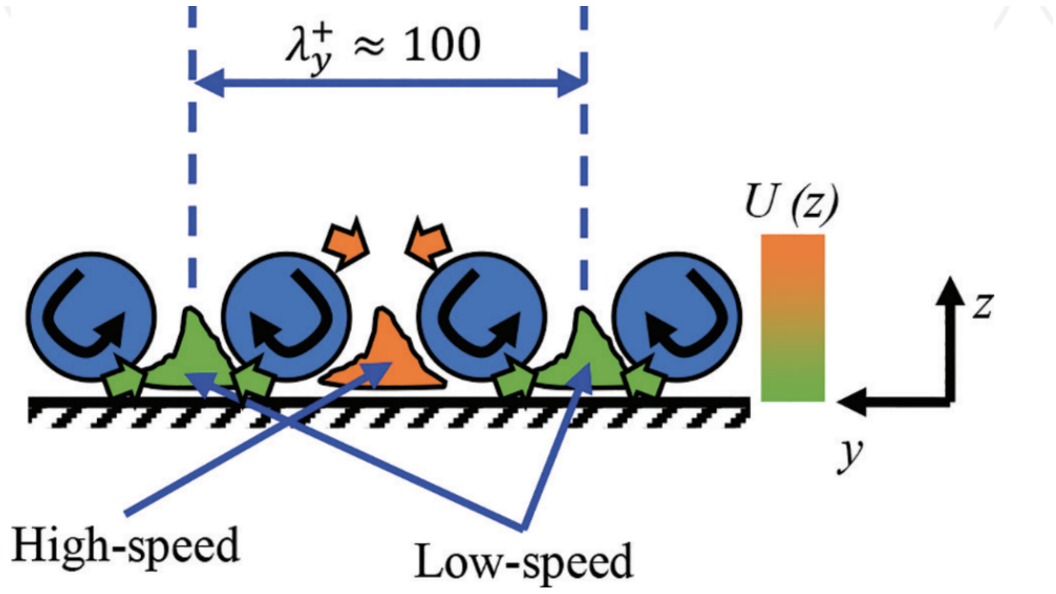

Figure 1.5: *High- and low-speed streak generation by streamwise counter-rotating vortices [70].*

presence of counter-rotating streamwise vortices is necessary for the production of streaks, streaks can persist even once this vorticity is suppressed [69]. The consistent research interest in streaks, comes from their dominant role in the production of near-wall turbulence and resulting drag generation.

Hairpin vortices are another fundamental structure observed within turbulent flows. The initial theoretical work proposing hairpin vortices was developed in 1955 by Theodorsen et al. [71]. However it wasn't until 1981 that the structure was successfully observed in experiments [72]. A hairpin vortex consists of two streamwise counter rotating vortices commonly referred to as "legs", which are connected at the "head" of the vortex (as shown in figure 1.6). This structure is self-interacting with the induced flow from the legs, lifting up the head into the upper boundary layer with its higher velocity flows. With different parts of the structure now experiencing different streamwise velocities, the structure is stretched in the streamwise direction. Also via the conservation of angular momentum, the vortex intensifies leading to faster rotation. Often streaks can be induced by the streamwise vortices present in the legs of the hairpin. Similarly streaks can lead to the development of hairpin vortices, allowing for a repeated cycle of induced coherent structures and turbulence generation.

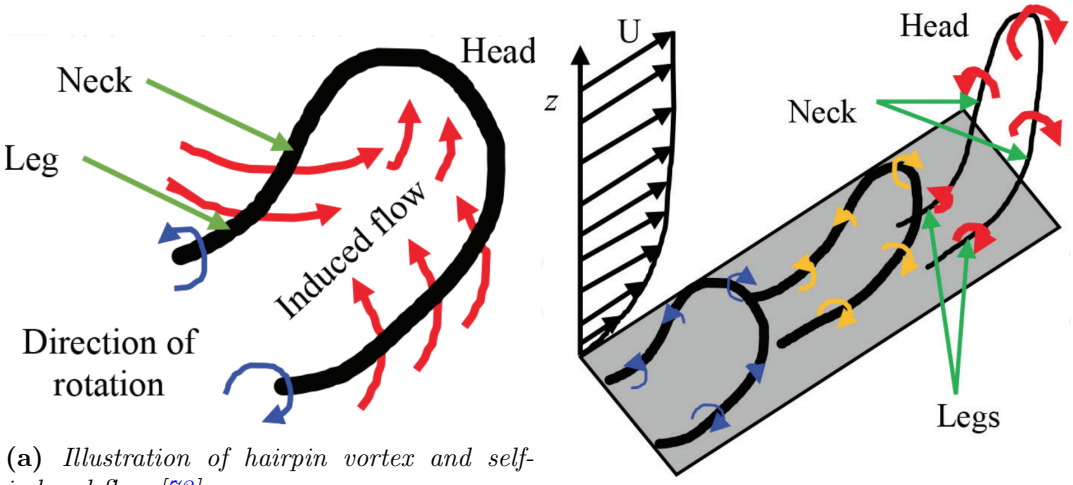

(a) *Illustration of hairpin vortex and self-induced flow [73]*

(b) *Illustration of hairpin vortex stretching [73]*

Figure 1.6: *The self-interaction of hairpin vortices.*

The coherent structures described above generate turbulence, but it is the breakdown of these structures which proliferates the turbulence and instigates the transition to a fully turbulent regime. The classical description of streak breakdown is called bursting. Originally described by Kline et al. [65], and then expanded by Kim et al. [74] amongst others, it has been characterised as having three phases: streak-lifting, meandering and finally bursting.

In the initial streak-lifting phase, the streak will drift away from the wall as it extends downstream. As the streak enters the higher-speed free-stream, it becomes stretched and narrower. The streak's low-speed fluid, causes an inflection in the boundary layer's velocity profile. This velocity gradient leads to a viscous shearing, and eventually the formation of a spanwise vorticity, and consequently a hairpin vortex. This induced vorticity then propagates downstream.

Once a certain threshold is reached, the streaks become unstable and begin to exhibit secondary instabilities. These present themselves as the meandering and oscillations of streaks in both the wall-normal and span-wise directions. Finally, the amplitude of the oscillations steadily increases until the non-streamwise momentum leads to fluid separating from the streak and the streak breaking down. This is called bursting [74].

1.7.1 DBD Actuators For Flow Control

The original DBD actuator design by Roth produced a tangential wall jet of 2.4 m/s [75] which due to incremental design improvements can now reach speeds of 7 m/s, and upto 11 m/s if an array of actuators are used [5]. This relatively modest control effect has proved useful for a variety of applications, particularly low speed flows. There are three main ways a massless control can be used: delaying transition, preventing detachment, and stabilising wake flows. The versatility of these actuators has been demonstrated by the development of a number of different geometries and operating regimes to utilise the control effect for different applications.

Early experimental works such as Hultgren et al. [76] show that early transition can be promoted to control boundary layer separation using a single DBD actuator. This was achieved for a range of low speed flows ($50000 < Re < 300000$) and various free stream turbulence intensities (from 0.2% to 7%). More recently, Grundmann et al. have been able to suppress transition on a flat plate [77]. This was achieved with actuators operating in a both steady and pulsed modes suppressing artificially generated Tollmien–Schlichting waves, thus stabilising the boundary layer. The alternative crossflow transition mode has been suppressed in supersonic boundary layers by Schuele et al. [78]. Here millimetric annular DBD plasma actuators were used to mimic passive surface roughness by exciting subcritical wavelengths and thus increasing the stability of the mean velocity profile in the cross flow.

Delaying and preventing separation around cylinders and bluff bodies can lead to dramatic drag reductions. This makes them well suited for control by active flow control methods which can have an apparent effectiveness of over 1000 [6]. The classical example of a bluff body is the cylinder, therefore it is unsurprising there has been several works where DBD plasma actuators have been implemented to control flow round a cylinder. One of the earliest works was Thomas et al. [79], where linear DBD actuators were used to stabilise the

wake flow around a cylinder. The Karman shedding was totally suppressed, even at a 25% duty cycle, which was found to be the most effective. This work was expanded on by Asghar et al. [80], who used a similar experimental set up to synchronise the vortex shedding from two circular cylinders. This was found to be successful for an arbitrary choice of cylinders.

Another key area of flow control is associated with improving the aerodynamic performance of aerofoils, due to their multitude of applications. DBD plasma actuators have been implemented widely in this area to improve a range of performance characteristics. Post et al. [37] investigated improving the performance of a generic aerofoil. By implementing a DBD actuator near the leading edge, the flow was reattached at an angle of attack 8 degrees beyond stall. The mechanism of stall recovery is attributed to the near-wall jet, generated by the actuator, injecting momentum into the boundary layer, and preventing a negative boundary layer velocity gradient.

Experimental investigations have also found that DBD actuators deployed at the leading edge improved the high-angle-of-attack performance of both a flat-plate, NACA [81], and Eppler E338 aerofoils [82] in low speed flows ($Re = 3000$). Such a deployment was found to lead to a significant increase in lift coefficient, especially at high angles of attack. Performance was also improved over a 75 deg swept delta wing at moderate Reynold's numbers ($Re = 10^5$) by implementing a series of actuators affecting the wake and leading-edge vortex, respectively [83]. In addition to the experimental investigations, several phenomenological models have been used to model the flow control effect on aerofoils. For example, a phenomenological model was used to investigate stall prevention in high angle-of-attack NACA 0015 airfoils using pulsed actuation [84]. Another example is the mitigation of flow separation and vortex shedding post stall, using a variety of actuator configurations [85].

The DBD actuator has also been applied for attenuating cavity noise [86], enhancing jet mixing [87], as well as both the primary [88, 89] or supplemental [90] high-lift device on UAVs. Work has also been undertaken to implement

DBD actuators as part of a closed loop control. An early example of this is where mixing in a 3D pipe flow was maxmimised by axisymmetic suction-blowing pairs [91].

1.7.2 Controlling Boundary Layer Instabilites

Due to their small scale, coherent boundary layer structures can be modified with minimal energy input resulting in a very effective control. However, there are a number of challenges to overcome before such a control method can be practically implemented. Such a strategy would require sensing and actuation to be implemented at the time and length scales of the near-wall coherent structures. This would require sub-millimetric actuators operating with an extremely fast response time. The chaotic and unpredictable nature of these structures would also necessitate a dense spatial array of actuators over the surface, reacting in real-time to microsensor input. The practicality of designing such microsensors and actuators, which can be manufactured, installed, and maintained cheaply whilst having sufficient durability for practical applications has proven a significant challenge. The long-term practical feasibility of such a system is still a subject of disagreement.

An early attempt at the active control of streaks was published by Gad-El-Hak et al. in 1989 [92]. This work showed that artificially generated streaks could be suppressed with precise and selective suction from two sub-millimetric mechanical actuators ($D = 0.4\ mm$). This control prevented streak breakdown and effectively delayed the transition to turbulence. In fact, with a suction coefficient of $0.0006 - 0.0015$, the effectiveness was much higher than anticipated with only a nominal power input required. However this work did not address the feasibility of implementing such a control, with no method of predicting the location of streaks or scaling the control across the surface. Significant structural modifications would also be required before such an actuator could be distributed over its surface to prevent structural weaknesses. However, this

work did demonstrate the potential benefits and effectiveness of a localised control acting at the time and length scale of streaks.

Since this preliminary work, there have been large improvements in the micro-fabrication of Micro-ElectroMechanical Systems (MEMS). These are electronic systems with mechanical moving parts and generally range in size from 1 μm to 1 mm [93]. The motion of mechanical parts is generally developed by either electrostatic actuation or thermal expansion. These improvements in micro-fabrication allow for the production of cheap sub-millimetric actuators which can be affixed to a surface cheaply and easily. In 1998, Sherman et al. showed that a MEMS actuator with an oscillating microplate could induce a spanwise velocity into the boundary layer, and concluded such a device could be used to suppress streaks by generating two counter-rotating streamwise vortices [94]. However, the device's small moving parts would be susceptible to damage from debris, icing, and surface abrasion present in real-world applications.

Another attempt at designing a distributed sub-millimetric control was devised by Jacobson et al. in 1997 [95]. This was another MEMS design which used a piezoelectric cantilever mounted flush to the wall. This device generated two counter rotating stream-wise vortices leading to the formation of streaks more than 40 displacement thicknesses from the point of actuation. Such an actuator could either exacerbate or suppress streaks via superposition.

Around the same period a numerical investigation by Schoppa et al. showed that a large-scale actuation of spanwise velocity leads to the suppression of breakdown, and thus turbulence generation, of multiple streaks, arguably negating the need for a distributed millimetric control [96]. However the control effectiveness was significantly below that demonstrated by Sherman and Gad-El-Hak. A spanwise actuation of 6% of the centreline velocity was required to achieve a drag reduction of 20%, which highlighted the compromise between low effectiveness and implementation complexity. Another more recent work by Yao et al. [97] expanded on this principle using a single large actuator to suppress multiple streaks. Here a wall tangential force was used to

generate a spanwise surface velocity, which in turn suppressed boundary layer streaks. However, once again, the actuation of a larger volume of fluid than required to suppress an individual streak led to the control being sub-optimal in terms of effectiveness, with only a 17% net power saving being achieved.

A key advantage of an active control system is that they can be implemented periodically, and only when required. In 2003, Rathnasingham et al. expounded this possibility by developing an experimental control system which utilised synthetic jets and wall-based shear sensors [98]. This allowed sensors to detect the presence of oncoming unstable streaks, which could then be suppressed with the application of the control. This system was found to reduce bursting events on a smooth surface by 23% with a control efficiency of approximately 50:1. This use of precise non-continuous operation resulted in a significantly improved efficiency compared to the theoretical work of Schoppa et al.. Whilst a significant development, the use of synthetic jets requires the manufacture of a cavity into the design, and they have limited modes of operation. They could also introduce artifacts into the flow during passive operation. It should also be noted that this was a preliminary study and the distributed actuator array had only 3 actuators.

Despite this progress in MEMS based control there are still a number of challenges that need to be overcome before the technology can be feasible for real-world applications. MEMS requires the fabrication of sub-millimetric 3D structures, as well as the obvious complexity of microfabrication, these devices have very high surface area to volume ratios. This leads to difficulty modelling the multiple flow scales at the surface and can lead to unexpected changes in the flow field. Modelling down to the molecular scale is sometimes required which is infeasible for complicated flows. There is also a question of durability; MEMS often rely on the repetitive heating and cooling of components, leading to issues of thermal creep, as well as being sensitive to abrasion, icing etc. [93]. Plasma actuators can be produced at MEMS-like scales at a lower cost, and are significantly more robust. They retain the advantage of being fully elec-

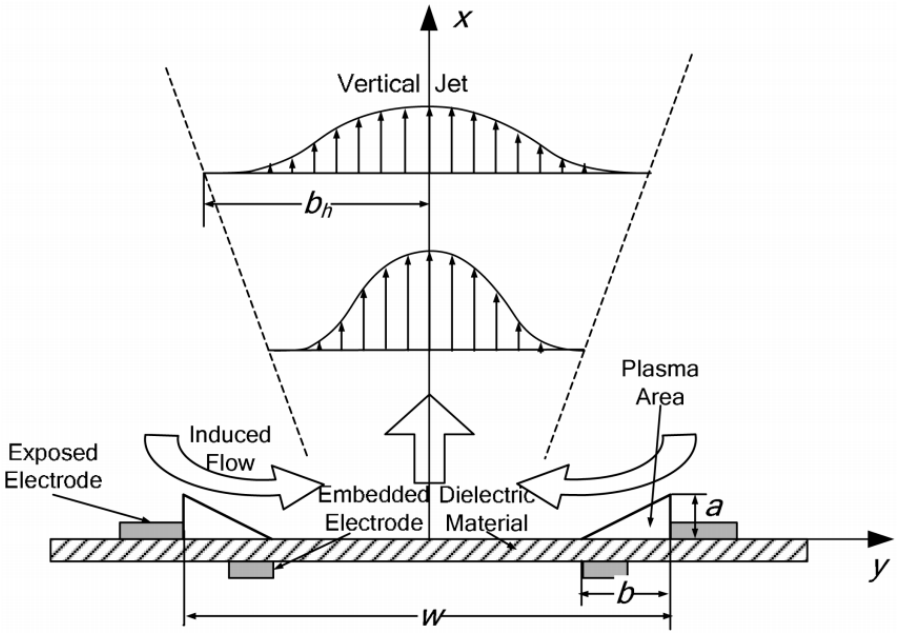

Figure 1.7: *Schematic of linear plasma synthetic jet in an outward jet configuration and induced flow field*

tronic, but without any moving parts, and are resistant to icing and abrasion. In fact in recent works plasma actuators have been shown to be effective at deicing [99, 100].

An example of a DBD plasma actuator capable of generating counter rotating vortex pairs is the linear synthetic plasma jet (LSPJ). Figure 1.7 shows an example schematic of this device, which produces a stream-wise wall-normal jet . Originally developed by [101], to combine the features of both plasma actuators and synthetic jets, a series of experimental and numerical investigations to characterise these jets have been conducted. LSPJs contain two linear exposed electrodes, and one electrode submerged below a dielectric sheet. The exposed electrodes are located adjacent to the submerged electrode, to ensure a strong electric field. When actuated, fluid is driven towards the centreline where it collides with the flow from the opposite electrode and is ejected as a perpendicular jet. This leads to the formation of a counter rotating streamwise vortex pair, although this is generally larger than the scale of most streaks. The actuator configuration was also shown to be reversible acting as a suction device [102].

Figure 1.8 shows the mean axial velocity distributions of a linear plasma synthetic jet obtained by Liu et al. [103] by solving the Reynolds-averaged Navier–Stokes equations with a phenomenological model for the plasma-induced body force. Here, the widths of the exposed and embedded electrode were 6.35 mm and 12.7 mm, respectively, and the streamwise length was 90 mm.

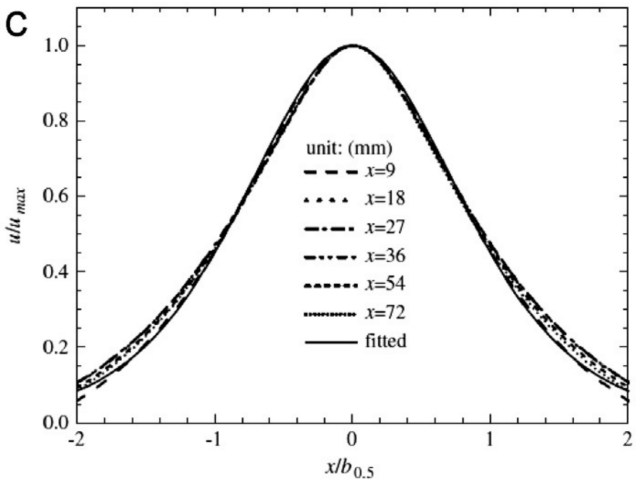

Figure 1.8: *Mean axial velocity distribution of a linear plasma synthetic jet operated with steady actuation in an outward jet configuration. [103]*

An array of actuators in the alternative suction configuration was demonstrated by [104], and is shown in figure 1.9. By utilising a much shorter exposed electrode, a downwash is generated as fluid is driven away from both edges of the exposed electrode. An array of these actuators induced a series of counter-rotating streamwise vortices near the surface. However, due to the scale of the actuators ($\lambda = 28\ mm$), the induced vortices were much larger than the scale of individual streaks. Therefore instead of attempting to suppress streaks, this actuator array was used to induce boundary layer mixing and reattach the downstream flow leading to a 67% drag reduction.

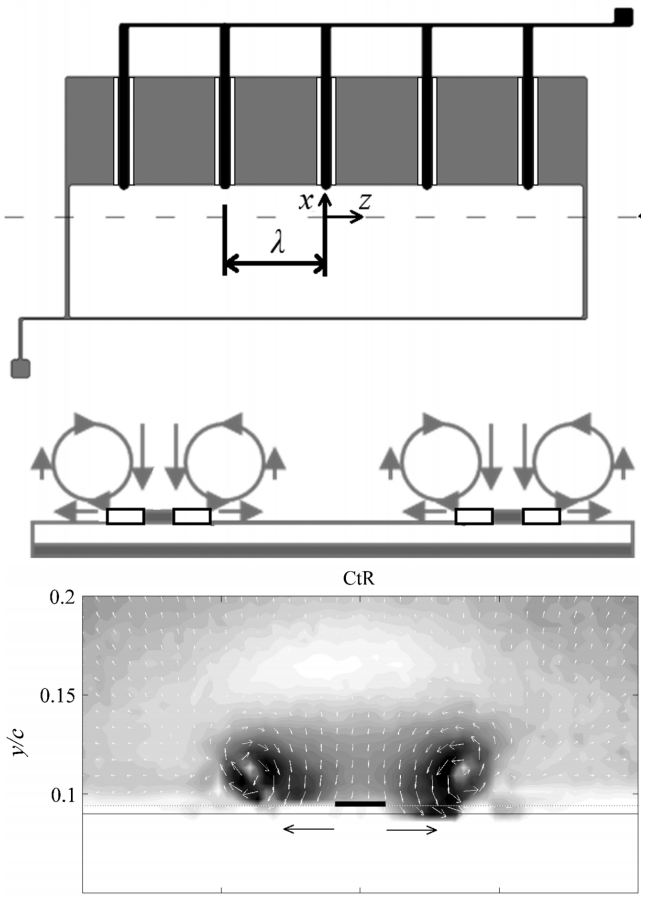

Figure 1.9: *Schematic of array of linear synthetic jets operating in a suction configuration, and resulting flow field in quiescent air. [104]*

Chapter 2

Numerical Modelling

2.1 Introduction

Numerical modelling is an important part of the design process for engineering solutions. It is also increasingly used to research physical phenomena occurring at scales which make experimental observation difficult. Dielectric barrier discharge actuators clearly fall into this category, with limited experimental observations available to elucidate the underlying small-scale mechanics. However, resolving the large range of spatial and temporal length scales means that a full resolution of the phenomena is numerically expensive.

To avoid this cost, phenomenological models have been developed, which use approximations of the plasma structure based on experimental observations to reduce the level of computation. These models generally restrictive for research, as they can only be used in situations, where the structure of the plasma matches the scenario where they have been validated. This work will examine small-scale actuators where the structure and behaviour of the discharge differs from their large-scale counterparts. Therefore a type of numerical model called a plasma-fluid model to examine the physical mechanisms of DBD actuators will be used. Such models track the distributions of each species and model the interactions between them.

This chapter will review the most relevant literature and scientific develop-

ments for the numerical modelling of non-thermal plasmas. It will then detail the plasma-fluid model used in this work, as well as any assumptions taken. Finally, the novel numerical schemes used to reduce the high numerical cost will be described.

2.2 Review of Empirical and Phenomenological Models

Without significant increases in computing power, fluid models will often be too time-consuming and computationally expensive to be used readily in industry. With the increased interest in DBD actuators, there is an increased need to develop an accurate model with a significantly reduced computational cost. To this end, there have been a number of efforts to develop phenomenological models, which use experimental observations to make assumptions about the macroscale structure of the gas discharge. This allows predictions of DBD actuator performance without the full simulation of the plasma mechanics, or slow and expensive experimental testing. However, there is a significant trade-off between the accuracy of the simulation and computational cost, and phenomenological models may not be valid for new actuator configurations.

The first phenomenological model was suggested by Roth and colleagues in [105] [106], soon after their initial development of the DBD actuator. Here the body force was taken to be proportional to the gradient of the squared electric field,

$$f_b = \frac{d}{dx}(\frac{1}{2}\epsilon_0 \boldsymbol{E}^2) \tag{2.1}$$

However, this model neglected the self-generated electric field of the charged species, which has been shown to be important, particularly for streamer generation. In fact, this model was later shown to be invalid for all cases except where $\boldsymbol{E} = E_x, E_y = E_z = 0$, and $\partial/\partial y = \partial/\partial z = 0$, which rarely occurs in

practical applications [107].

A model initially published by Peers [108], the so-called velocity inlet model, fits a 5th order polynomial to a velocity profile taken from an experiment, then used this polynomial as a velocity boundary condition at the surface where the actuator would be deployed. This reduced the computational cost of simulations as no additional PDEs needed to be solved. However, as this velocity profile was taken from one set of experiments, and performance can vary significantly with design, applied voltage and ambient conditions, it makes this model relatively inflexible and inaccurate. That said, this model has shown good agreement with some simple flows. This model is somewhat unusual in prescribing a velocity boundary condition. Most phenomenological models predict a cycle-averaged body forcing distribution, which can easily be implemented in modern Navier-Stokes solvers.

In 2002, Shyy et al. [109] developed one of the first such models, with the key assumption that the electric field strength varied linearly from the exposed electrode edge. The maximum value of the electric field was assigned in a calibration process, and a constant background charge density was also assumed. Whilst the model showed some qualitative agreement with experimental results, Orlov et al. later measured an exponential decay in electric field strength from the electrode edge, showing this assumption to be invalid [20]. Despite this, the model continued to be widely used even though it over-predicted the actuator thrust.

One of the most popular phenomenological models was developed by Suzen et al. in 2005 [110]. Instead of making an assumption about the electric field distribution, here an approximation of the charge density distribution was used. The logic behind this decision was that the electric potential, and thus the electric field can be quickly and accurately calculated for any geometry, making the model more versatile. The calculation of the particle density distribution was numerically expensive, and by reducing this to a simple approximation, significant computational savings were made. Suzen et al. opted for a Gaussian

distribution to agree with the experimental observations of Orlov et al [21]. In comparisons with experiments it was found that the two-dimensional (2D) distribution appeared physical, although the scaling with the applied voltage magnitude did not match experimental results.

Orlov et al developed another model in 2009 [111] using a lumped circuit approach. By treating the plasma volume as a series of resistors and capacitors in parallel, a time dependent boundary condition could be developed for the electric potential. The charge density was determined using the Boltzmann relation, which meant the body force distribution could be written as

$$\boldsymbol{F} = -(\frac{\epsilon_0}{\lambda_D^2})\boldsymbol{E} \tag{2.2}$$

where λ_D denotes the Debye length, and ϵ_0 is the permittivity of free space. This reduces the system to one unknown, which can determined by solving a Helmholtz equation. This led to a significantly reduced computation time. However the Boltzmann relation assumes the plasma is in thermal equilibrium which experimentally is not the case for DBD actuators. Unlike the previous models, this model gives a time-dependent approximation for the EHD body force. This model was validated by experimental Particle Image Velocimetry (PIV) measurements, although the forcing distribution was found to be disproportionately tangential to the surface. Mertz [112] expanded Orlov's model into a more general coordinate system, allowing for the grid dependence to be removed. This new formulation matched more closely with the experimentally measured forcing distribution.

Phenomenological models can accurately predict the resulting flow structures generated by DBD actuators, although they often need to be "calibrated" to a particular set-up, by manually choosing parameters to match a particular configuration. However, such models are unsuitable for predicting the performance of new configurations, as the assumptions underpinning these models are based on a narrow range of observed experimental results, and are unable

to make predictions outside of this range. Such models are also unsuitable for elucidating the underlying mechanics of a DBD discharge as they do not resolve the small scale mechanics, which are often of interest.

2.3 Review of Fluid Models

A plasma-fluid, or often simply fluid, model, tracks the distributions of macroscopic properties for each species, as well as modelling the interactions between them. Such a model can accurately describe the atmospheric and sub-atmospheric gas-discharge mechanics by resolving all the spatial and temporal length scales. However, as the temporal and spatial length scales can be $O(10^{-16}s)$ and $O(1\ \mu m)$ respectively, such models can be extremely computationally expensive. This high cost means fluid models are often too expensive and time-consuming for industrial applications, and has inhibited investigations into the gas-discharge mechanics for long time periods. However, there is a trade-off between reducing computational cost and maintaining accuracy. This section reviews the progress in developing an accurate fluid model, whilst reducing computational cost.

There were several early attempts at developing a fluid model for plasma modelling [113, 114]. However, such models were unable to capture the physics, or be validated by experimental works. This was due to the difficulties in resolving the full complexity of the problem, including the surface chemistry, as well as three-body attachment, and photoionisation.

One of the most successful early works was undertaken by Singh et al. [115]. This model simplified the gas chemistry by assuming a pure helium mixture at 40% of atmospheric pressure. It fully resolved the continuity and drift-diffusion equations for the electrons and positive ion species. This was coupled with a solution of the electric potential. However, several key physical mechanisms were neglected including secondary emission, recombination, and most crucially the deposition of surface charge on the dielectric. Despite this, the model was able

to give a qualitative approximation of the induced EHD forcing distribution. This model was then coupled with a fluid dynamic solver to resolve the resulting fluid dynamics. The resulting flow fields were found to mimic those observed in experiments as did several key gas discharge characteristics.

Another numerical work was undertaken by Boeuf et al.[116], which included both the charging of the dielectric and secondary emission. The model used pure Nitrogen gas to simplify the resolution of the required chemistry. The plasma dynamics were also decoupled from the fluid mechanics, assuming that the induced flow would not effect the resulting gas discharge. Initially, a constant voltage pulse was used, and a single plasma discharge over 100 ns was modelled. The work was later extended to include more practically relevant voltage profiles including sawtooth and sinusoidal waveforms [22, 25]. This was the first time the asymmetry between the positive and negative half-cycles was modelled. During the positive half-cycle, a series of corona discharges were observed sparsely interspersed with the formation of high-current positive streamers. The corona discharges were found to be responsible for the majority of the forcing due to the short time-period of the streamers, and the large volume of the corona discharges. During the negative half-cycle repetetive microdischarges were observed with significantly reduced current pulses compared to the positive streamers.

Another two-species plasma-fluid model was developed by Jayaraman et al. [117]. Similar to Boeuf et al.'s model, this modelled only the ionisation and recombination, but the behaviour of the neutral fluid was not decoupled. A novel finite-volume operator-split algorithm was used to overcome the stiffness of this coupling. In this study the relationship between applied voltage and induced EHD force was characterised, and validated with experimental results. The relationship between the size of the submerged electrode was also investigated [118, 119]. It was found that the plasma volume cannot exceed the size of the submerged electrode, and concluded that a larger electrode size was beneficial as this prevented the thrust and actuator performance from being

limited. The applied voltage profile and dielectric thickness were also found to have a strong effect on the induced EHD force.

Likhanskii et al. later developed a 4-species model [23], which allowed for negative ions to be modelled and their importance investigated. This work expanded on Boeuf et al.'s [28] results, describing the EHD force's temporal and spatial distribution within each half-cycle. It demonstrated the significant role of the negative ions in EHD force development during the negative half-cycle.

To further investigate the role of the negative ions in the discharge, Boeuf et al. conducted a complimentary parametric study [120], that showed that the effect of negative ions increased when the applied voltage is of high amplitude and low frequency. Since this work, a number of other 4-species models have been developed as the technique captures the full physics of the discharge without the additional computational cost of treating multiple positive species or multiple negative species separately.

The computational cost of a 4-species fluid model is still too high to be practically used in most industrial settings. To address this, Unfer [121] developed a semi-implicit scheme for the resolution of the electric potential and drift-diffusion equations. This allowed for a larger less-restrictive time-step to be used, by approximating the future space charge density of the next iteration to overcome the dielectric relaxation time constraint. However, the macroscopic quantities of interest can be linked to this physical time, so care must be taken to ensure the formulation is valid and stable for particular cases. An asynchronous scheme of sub-cycling time-steps was also used to reduce the computational cost.

The models described above all used a two-dimensional plasma distribution with an assumption of spanwise uniformity. This is primarily to reduce the computational cost, with $3D$ simulations largely intractable with the current computing power available. However, numerous experiments have shown gas discharges with a complicated spatio-temporal structure e.g. when operating

in the streamer regime. Nishida et al. [122] conducted a three-dimensional plasma model across very short time periods to test the assumption of spanwise uniformity. It was found that, whilst the discharge during the negative half-cycle was stable in three dimensions, minute numerical noise led to a streamer regime during the positive discharge, which became rapidly non-uniform and led to a lack of stability in the spanwise direction. However, the span-wise averaged EHD body force and plasma macroscopic properties were found to have the same spatial and temporal characteristics as their 2D counterpart.

2.4 Numerical Modelling of Non-Thermal Plasmas

Several models have been developed which focus on the behaviour of individual energised particles [123]. However, in most practical applications, plasmas will contain sufficient particles that tracking them individually is unnecessary and challenging. Models which treat plasmas as continuous distributions of particles are called "plasma-fluid" or simply "fluid" models and are desirable for many scenarios. In this study, COPAIER, a 4-species fluid model developed by Office National d'Etudes et de Recherches Aérospatiales (ONERA) and described in detail in [124] was used. It uses advanced numerical methods to reduce computational cost and make the relatively long simulations $O(10^{-3}s)$ tractable [125] , and has been used to give detailed breakdown of the forcing for linear DBD plasma actuators [34].

2.4.1 The Boltzmann Equation

The governing equations for all fluid models are derived from the Boltzmann equation, which describes the evolution of particle distributions with time. However, as the velocity of the charged species is a key driver of plasma dynamics, generating magnetic fields and dictating the rate of ionisation (see

Chapter 1), plasmas cannot be fully described as a continuous spatial distribution of particles.

The solution is to describe a plasma distribution as a 6-dimensional phase space $f(\boldsymbol{x}, \boldsymbol{v}, t)$ which is a function of space, velocity and time. It describes the probability of finding a particle at a particular location, with a particular velocity, at a particular time. The Boltzmann equation was formulated to describe the evolution of such phase space with time. The partial derivative version of this equation is shown below.

$$\frac{\partial f}{\partial t} + (\boldsymbol{v} \cdot \boldsymbol{\nabla}_x f) + \frac{q}{m}(\boldsymbol{E} + \boldsymbol{v} \times \boldsymbol{B}) \cdot \boldsymbol{\nabla}_v f = \left.\frac{\partial f}{\partial t}\right|_c \tag{2.3}$$

Here f is the particle distribution function in phase space, $\boldsymbol{v}$ is the velocity vector, $\boldsymbol{\nabla}_x = \{\partial/\partial x, \partial/\partial y, \partial/\partial z\}$, $\boldsymbol{\nabla}_v = \{\partial/\partial v_x, \partial/\partial v_y, \partial/\partial v_z\}$, and $\boldsymbol{E}$ and $\boldsymbol{B}$ are the electric and magnetic fields respectively. The $\left.\frac{\partial f}{\partial t}\right|_c$ term describes the effect of particle collisions, whether the increased production or destruction of charged species, or their acceleration. In situations where particle collisions can be neglected, this term is set to zero, and this equation becomes the collisionless Boltzmann equation or Vlasov equation [126].

By taking moments of the phase-space distribution, several useful macroscopic quantities can be derived.

$$\text{The Particle Density} \quad n(\boldsymbol{x}, t) = \int f d^3v \tag{2.4}$$

$$\text{The Particle Flux} \quad \Gamma(\boldsymbol{x}, t) = n\boldsymbol{v} = \int \boldsymbol{v} f d^3v \tag{2.5}$$

$$\text{The Particle Volumetric Kinetic Energy} \quad w = \tfrac{m}{2} \int \boldsymbol{v}^2 f d^3v \tag{2.6}$$

These identities, when combined with the Boltzmann equation, can be used to derive the governing conservation equations for all plasma-fluid models, and are described in the following sections.

2.4.2 The Continuity Equation

As discussed above, the zero-th moment of the Boltzmann equation is the foundation of the first governing equations for a plasma-fluid model. It can be derived by integrating the Boltzmann equation over velocity space.

$$\frac{\partial n}{\partial t} + \nabla \cdot (n\boldsymbol{v}) = S \tag{2.7}$$

The right hand term S describes the creation and destruction of species via chemical reactions e.g. ionisation. The accurate description of this term, is a key difficulty in developing an accurate plasma-fluid model. The probability of a single ionisation event is a non-linear function of electron energy. Additionally, the electron energy distribution is often non-Maxwellian with a disproportionate abundance of high speed electrons. To calculate an approximate distribution of electron energies, the local field approximation (LFA) is often used. The LFA assumes energy gained by the accelerating electrons is lost locally due to the large number of collisions, and thus the gain in electron energy is not transported throughout the plasma. Whilst this holds for highly collisional plasmas, it is limited as the electron-ion mass difference will lead to largely elastic collisions and thus an extremely large number of collisions is required to sufficently decelerate the electrons.

Such an approximation is useful, however, as it allows the electron energy to be calculated purely as a function of the reduced electric field $\boldsymbol{E}/N$. It is therefore common for the the source term S to be calculated as

$$S = n_e \boldsymbol{v_e} \alpha \tag{2.8}$$

where α is the Townsend coefficient, calculated using an empirical function of the reduced electric field [13]. Such an approach is limited by the accuracy and number of experimental observations for each gas (or mixture of gases) in the desired operating range.

However, the more modern approach is to use a two-term approximation of the homogenous Boltzmann equation, to calculate the ionisation coefficients for a range of reduced electric field strengths, from molecular collision cross-section data. BOLSIG+ is an open-source solver developed by Hagelaar et al. for this purpose [127]. This allows the rate coefficient for electron-impact reactions to be calculated as

$$k_i = \frac{4\pi}{n} \int_0^\infty \sigma_i \boldsymbol{v}^3 f_0 dv \tag{2.9}$$

where k_i and σ_i are the rate coefficient (in m^3/s) and the momentum transfer cross-section taken from experimental data for the i-th species respectively, and f_0 is the isotropic part of the phase space distribution. This in turn gives

$$S = \sum_i N_i n_{1i} n_{2i} k_i \tag{2.10}$$

where n_1 and n_2 are the number densities of the colliding particles, and N is the number of particles created in one collision. Some important reactions, especially the formation of negative ions, involve three particles. In such a case n_3 is required and the units of the rate coefficient adjusted accordingly. In this work, to reduce computational cost, the number of kinetic reactions considered have been reduced to four, describing the interaction between electrons and three heavy species n_+, n_- and n_n, standing for the positive, negative and neutral particles, respectively. These four processes can be summarised below

$$n_n + e = n_+ + 2e \qquad \text{(Ionisation)}$$

$$n_n + e = n_- \qquad \text{(Attachment)}$$

$$n_+ + e = n_n \qquad \text{(Electron-Ion Recombination)}$$

$$n_+ + n_- = n_n \qquad \text{(Ion-Ion Recombination)}$$

The collision cross-section data from the LXCat databases [128, 129] were combined with BOLSIG+ to calculate the rate coefficients for each interaction, for various mixtures of nitrogen and oxygen.

Photoionisation does not play a significant role in atmospheric discharges, other than to provide the seed electrons for Townsend breakdown. It does however introduce additional computational complexity and cost [130]. As the scope of this thesis is limited to atmospheric discharges, photoionisation is therefore neglected and a minimum density for each species is used to represent the spontaneous production of free electrons. During our simulations the number density of all particles always exceeds this floor value.

2.4.3 The Drift-Diffusion Equations

Particle Fluxes are a key driver of the discharge process. It is therefore important they are modelled accurately and efficiently. Taking the first-order moment of the Boltzmann equation, gives the momentum equation, which describes how momentum is transported through the domain.

$$mn[\frac{\partial v}{\partial t} + (v \cdot \nabla)v] = qn(\boldsymbol{E} + \boldsymbol{v} \times \boldsymbol{B}) - \nabla \cdot P + f\Big|_c \tag{2.11}$$

where m is the particle mass, n is particle number density, $\boldsymbol{v}$ is the particle velocity, and P is the pressure tensor. For atmospheric discharges we can neglect inertial terms and unsteady terms assuming that the ionic species are in thermal equilibrium with the background neutrals. This leads to the reduced set of equations

$$n_e \boldsymbol{v_e} = -n_e \mu_e (\boldsymbol{E} + \boldsymbol{v_e} \times \boldsymbol{B}) - D_e \nabla n_e \tag{2.12}$$

$$n_i \boldsymbol{v_i} = n_i \mu_i (\boldsymbol{E} + \boldsymbol{V_i} \times \boldsymbol{B}) - D_i \nabla n_i \tag{2.13}$$

where μ and D are the mobility and diffusion coefficients. Similar to the

ionisation coefficients described in subsection 2.4.2, these coefficients depend on the electron mean energy. As previously, the BOLSIG+ solver can be used to generate a table of coefficient values at different $\boldsymbol{E}/N$ which can be interpolated to give accurate mobility and diffusion coefficients [131].

Under typical operation, the gas discharge formed by a DBD plasma actuator will not be magnetised. This allows a further reduction to the drift-diffusion form:

$$n_e \boldsymbol{v_e} = -n_e \mu_e \boldsymbol{E} - D_e \nabla n_e \tag{2.14}$$

$$n_i \boldsymbol{v_i} = n_i \mu_i \boldsymbol{E} - D_i \nabla n_i \tag{2.15}$$

It is also possible to go further and neglect the diffusive term, as the strong electric fields and high mobility ensure that DBDs are advection dominated.

The Electric Field, $\boldsymbol{E}$, can be found with the resolution of a Poisson equation.

$$-\nabla \cdot (\varepsilon \boldsymbol{E}) = \rho_c \tag{2.16}$$

$$\boldsymbol{E} = -\nabla \phi \tag{2.17}$$

$$\rho_c = \sum_i n_i q_i \tag{2.18}$$

where ρ_c is the space charge from the accumulated charged species, ε is the material permittivity, and ϕ is the Electric Potential.

2.4.4 Modelling DBD Dynamics

It is important to model some DBD-specific dynamics. Firstly, secondary emission plays a role in the propagation of a corona discharge. As incident ions collide with the dielectric surface and electrode, a proportional flux of electrons

is produced. Different forms of boundary conditions have to be imposed at the dielectric surfacec for electrons (subscript e) compared to the heavier species (subscript s) to account for this.

$$n_e \boldsymbol{v_e} = \frac{1}{2} n_e \boldsymbol{v_{th}} - \alpha \sum_s \gamma_s n_s \boldsymbol{v_s} \cdot \hat{\boldsymbol{n}} \tag{2.19}$$

$$n_s \boldsymbol{v_s} = \frac{1}{2} n_s \boldsymbol{v_{th}} - \alpha_s \mu_s (\boldsymbol{E} \cdot \hat{\boldsymbol{n}}) \tag{2.20}$$

where γ_s is the secondary emission coefficient of a heavy species s, and is taken from experimental observations. α is taken as 1 when the flux is directed towards the surface and zero otherwise, whilst the thermal velocity $\boldsymbol{v_{th}}$ can be calculated as

$$\boldsymbol{v_{th}} = \sqrt{\frac{8 k_B T_s}{\pi m_s}} \cdot \hat{\boldsymbol{n}} \tag{2.21}$$

where k_B is the Boltzmann constant, m_s is the species' mass, and T_s is the heavy species temperature. The heavy ion temperature is sometimes approximated as the ambient gas temperature T_g due to the low energy transfer between ions and electrons. However it is more accurate to calculate it as

$$k_b T_s = k_b T_g + \frac{m_s + m_g}{5 m_s + 3 m_g} m_g (\mu_s E)^2 \tag{2.22}$$

where m_s and m_g are the mass of the heavy species and gas particles respectively.

These incident fluxes lead to the deposition of charge on the dielectric surface, and thus a discontinuity in the electric potential in the surface normal direction. It important to consider this effect to ensure the quenching behaviour is accurately modelled. The surface charge density σ is calculated as the accumulated total of the incident plasma current density $\boldsymbol{j}$

$$\sigma = \int \boldsymbol{j} \cdot \hat{\boldsymbol{n}} \, dt \tag{2.23}$$

assuming instant recombination and no surface diffusion. The plasma current density is equivalent to the sum of the incident charge fluxes of all species

$$\boldsymbol{j} = \sum_i n_i \boldsymbol{v_i} q_i \tag{2.24}$$

The discontinuity in the electric field can then be calculated as

$$[\![\varepsilon \boldsymbol{E} \cdot \boldsymbol{n}]\!] = \sigma \tag{2.25}$$

2.5 Resolution of the Multi-Scale Physics

As stressed previously, resolving all the length scales of this model is the fundamental challenge facing the numerical modelling of low-temperature plasma. There is no easy resolution to this problem, several works have tried to tackle it with novel numerical schemes [121, 132] but each are limited in their own way.

To understand why this problem is inherently multiscale, it is important to investigate the different time and length scales involved. A key attraction of DBD plasma actuators is their small scale ($O(mm)$), and to induce a gas discharge a strong electric field must be used. This necessitates strong variations in electric field over sub-millimetric distances. Additionally, the exposed electrode geometry is often sharp leading to a discontinuity and exacerbated field gradients. To model such a steep variation requires a number of very small characteristic lengths, smaller than the exposed electrode thickness which is often $O(\mu m)$. However, a full resolution of the plasma mechanics requires the resolution of the exceedingly high drift velocity of electrons $\boldsymbol{v_e}$

$$\boldsymbol{v_e} = \mu \boldsymbol{E} = O(10^{-2}\ m^2 s^{-1} V^{-1}) \cdot O(10^6\ V m^{-1}) = O(10^4\ m s^{-1}) \tag{2.26}$$

The Courant–Friedrichs–Lewy (CFL) constraint on the maximal time-step can

Phenomenon	Characteristic time scales
Transport of Electrons	From 1 ns to 1 ps
Electric field variations	From 1 μs to 0.01 ns
Kinetics	From 0.1 to 10 ns
Transport of heavy species (ions)	From 0.1 to 1 ns
Plasma dynamics	From 0.01 to 0.1 ms
Ionic wind	About 1 ms

Table 2.1: Characteristic timescales for an atmospheric plasma discharge [124]

be severe. This can be expressed in the one-dimensional case as

$$C_{max} \geq \frac{v_e \Delta t}{\Delta x} \tag{2.27}$$

where Δx is the characteristic length, Δt is the characteristic time-step, and C_{max} is Courant number which is usually ≤ 1 for explicit schemes. Rearranging gives a characteristic time step of the order of picoseconds.

$$O(\Delta t) = \frac{O(C_{max})O(\Delta x)}{O(v_e)} = \frac{O(10^{-1})O(10^{-6}m)}{O(10^{4}ms^{-1})} = O(10^{-12}s) \tag{2.28}$$

Table 2.1 summarises the different time scales that need to be resolved for a full resolution of a DBD actuator operating at atmospheric pressure.

This restrictive constraint is not only limited to the plasma near the exposed electrode edge. At high-enough charge density another characteristic length must be considered. The Debye length, λ_D can be formulated as

$$\lambda_D = \sqrt{\frac{\varepsilon k_B T_e}{n_e q_e}} \tag{2.29}$$

where k_B is the Boltzmann constant, T_e the electron temperature, and q_e the atomic unit of charge. Under the typical operation of a DBD actuator, the electron density can exceed $10^{18}m^{-3}$, whilst temperature will often exceed $1eV \approx 11000K$. The characteristic Debye length can therefore be reduced to $O(< 1\mu m)$. This 3 order difference in scale between the actuator geometry

and the electric field distribution, requires a dense mesh and thus increases the computational costs.

Dealing with the range of time scales is the fundamental challenge facing the numerical modelling of plasma. It is clearly intractable to resolve all these different scales using the most constrained time-step. The resolution of the multiple PDEs, especially the numerically expensive Poisson equation, makes this too computationally expensive. For this reason, COPAIER subdivides the problem into three parts: resolving the electric field distribution, resolving the drift-diffusion equations, and resolving the molecular kinetics, each of which utilises an individual numerical method. This subdivision allows for an individual timestep for each, and both adaptive time stepping and subcycling to be implemented. These solutions are coupled together using the Strang splitting strategy, which guarantees a second order accuracy in time. Maintaining the second order accuracy of the numerical methods used in COPAIER, which are briefly summarised below.

The drift-diffusion mechanics are governed by conservation equations so can be resolved with a finite volume approach. The Monotonic Upstream-centered Scheme for Conservation Laws (MUSCL) [133] is implemented to model the species' fluxes at the edges of the mesh with a second order space-wise accuracy. To allow for adaptive and iterative sub-cycling (the primary method used to reduced computational cost), the time-integration scheme must be conditionally stable. To this end, the Heun method [134] is implemented as it is both second-order accurate and is conditionally stable based on the classical CFL condition.

To resolve the electric potential distribution, the finite element method is used with a Q1 formulation. This is combined with a non-overlapping Schur Method [135], allowing for parallelisation and a reduction in simulation time. The Schur method generates a linear system of equations equal to the number of nodes on the interface, N_{interf} which needs to be solved at each time step. A matrix inversion of N_{interf} is therefore required at every timestep. Although, as this

interface geometry remains constant, a LU decomposition can be performed during preprocessing, speeding up this calculation. It is imperative to minimize the size of the interface to ensure reasonable solution times. Practically this prohibits using this method to resolve 3D plasma dynamics. Finally, to resolve the plasma kinetics a second order Runge-Kutta method is used.

Throughout the discharge cycle of a DBD actuator, there are periods of intermittent or low activity. The electron CFL time constraint is a function of the plasma density and electric field, both of which vary enormously and continuously during the cycle. There is therefore a large variation in the time constraint throughout any numerical simulation of a DBD actuator.

It is therefore unwise to restrict a numerical time-step to a single value. By choosing the fully explicit Huen scheme, with an exact conditional stability, the maximal stable time-step can be recalculated and used for each step [136]. This repetitive recalculation introduces an overhead at each step, but this is more than off-set by not being over-constrained throughout the entire simulation based on the most restrictive time-step encountered. An additional advantage is that the guaranteed stability eliminates the need for pre-simulation predictions of the plasma dynamics and corresponding time-step constraint.

By subdividing the solution into multiple levels, each with a characteristic time-step, they can be integrated independently using a time-step dependent on its own stability constraints. The computationally expensive solution of the Poisson equation therefore needs to be solved far less often.

2.6 Periodic Steady-state

The discharge of an AC DBD actuator is periodic, and depends on the residual charge deposited by the previous cycle. To achieve representative results, it is important to establish when a periodic steady state is achieved. However, due to the high computational cost in computing each cycle it is also prudent to minimize the total number of cycles calculated for each case.

The deposited surface charge is used to test whether an actuator has reached steady-state. This value is initialised at zero at the start of the simulation but will progress to having an average net positive or net negative charge once periodic steady state is achieved. In this work, we assume steady state is achieved when there is less than a 2% change in the cycle-averaged total surface charge.

Chapter 3

Flow Reversal Mechanism in Millimetric Annular DBD Plasma Actuators

3.1 Introduction

Dielectric Barrier Discharge (DBD) plasma actuators can produce flows of up to 10 m/s [137]. In order to maximally utilise this control effect under different conditions, a variety of electrode configurations have been investigated [138, 139]. One such example is the annular DBD plasma actuator, the axisymmetric counterpart to the more common linear DBD plasma actuator. The annular device produces axial jets perpendicular to the surface and has suggested promise as so-called virtual roughness elements used to control cross-flow instability [78, 140]. Here they mimic passive physical roughness elements by exciting subcritical wavelengths and thus increase the stability of the mean velocity profile in the cross flow. However, they have the potential to be significantly more versatile, as their effective element height, to which the stability mechanism is very sensitive, can be actively controlled.

Their ability to be readily manufactured into millimetric (even sub-millimetric) devices is one of the most promising advantages of DBD actuators over me-

chanical actuators. This provides the opportunity to directly control milli and microscale coherent structures and transition modes, resulting in a distributed active control with an unprecedented efficiency and effectiveness. At present, DBD actuators represent probably the only active control method that can be implemented in this way without a prohibitive cost.

Whilst investigating the behaviour of these millimetric annular actuators a surprising phenomenon was reported [38]. For millimetric actuators below a certain diameter, the direction of the perpendicular axial jet was reversed. This phenomenon has since been demonstrated for a variety of setups with an actuator diameter D $\leq$ 3 mm [140]. However, the mechanism behind this reversal remained unclear. This underscores the current limited understanding of how a millimetric geometry affects DBD discharge structure, whilst also highlighting the unexplored potential and versatility of these actuators. In part, this can be ascribed to the challenges of investigating discharge mechanics at extremely small time and length scales, often $O(\sim 10^{-13}\ s)$ and $O(\sim 1\ \mu m)$, respectively.

To overcome these challenges, the 4-species kinetic model discussed in Chapter 2 was used to reproduce this phenomenon and examine its underlying mechanisms. In all numerical cases described below the applied voltage was 2 kV at a frequency of 40 kHz, the dielectric constant, ε_r, was taken to be 3.5, and the electrode and dielectric thicknesses were 50 μm and 150 μm, respectively.

3.2 Flow Reversal

In this section the model is used to examine the reversal of axial flow direction due to the diameter of the actuator D. Figure 3.2 compares the contrasting velocity fields at various D. There are two distinct flow regimes, which can be designated as the outward flow regime, where the axial jet is directed away from the actuator, and the inward flow regime, where the axial jet is directed towards the actuator. An outward flow regime was observed for diameters

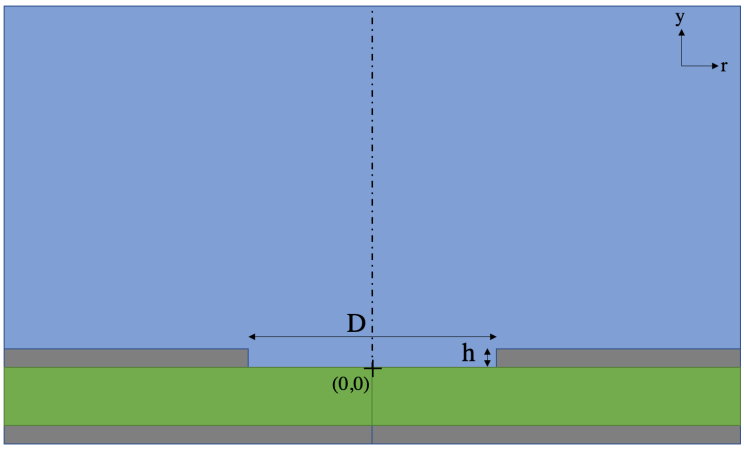

Figure 3.1: *The computational domain for the simulation of an actuator with diameter D and thickness h. Blue: fluid, Green: dielectric material, and Grey: electrodes. The full computational domain for an actuator with $D = 1\ mm$ and $h = 50\ \mu m$ extends from $(r, y) = (0\ mm, -0.15\ mm)$ to $(6.5\ mm, 8\ mm)$ and contains 58796 elements of which 46136 are in the fluid domain.*

$D \geq 2\ mm$, whilst an inward flow regime was present when $D \leq 1.5\ mm$ with no smooth transition being observed in between. In the outward regime, fluid near the exposed electrode edge is accelerated towards the dielectric generating a jet tangential to the surface. However, due to the axisymmetric geometry the colliding tangential jets are redirected as a positive axial jet [102]. On the other hand, in the inward regime the flow near the electrode is accelerated away from the dielectric surface leading to the formation of a quasi-stationary vortex ring, as well as the striking reversal of the axial jet. The reversal of flow direction near the electrode edge where the induced EHD force is generated indicates this phenomenon results from a change in the discharge structure, which will be confirmed in the following sections. The formation of small recirculation zones attached to the surface, near the electrode edge, at $D = 1.5\ mm$ is observed as the threshold diameter for the flow reversal is approached. It will be shown in §3.3 that this is due to the balance of the inward and outward EHD forcing components.

In each regime, the jet flow at various diameters shows a self-similar pattern. To confirm, the radial distributions of the axial velocity are normalised by their absolute maximum, as shown in figures 3.3(a) and (b). The outward jets approach a self-similarity at $y/D = 2$, and can be approximately fitted

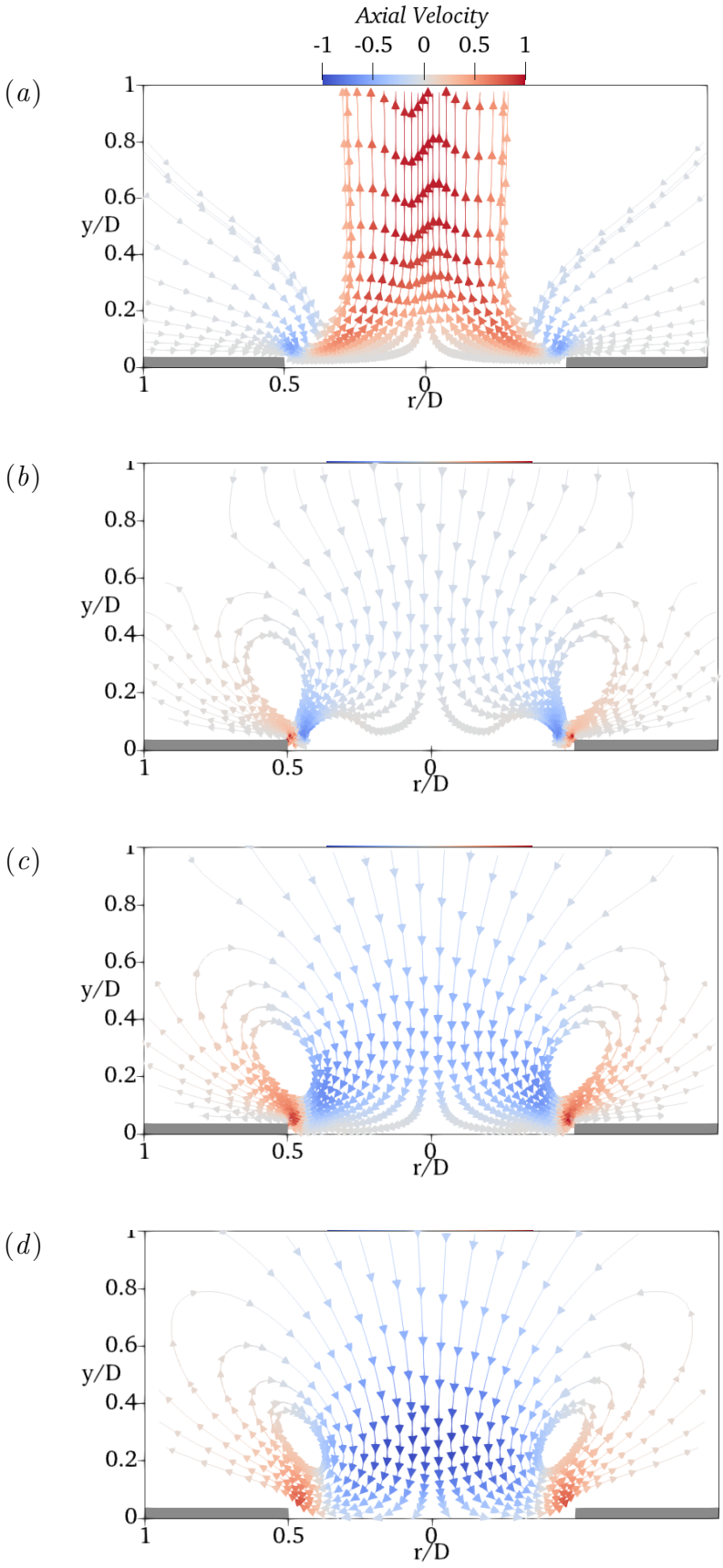

Figure 3.2: *Flow induced by annular DBD actuators with diameters $D = 2$ mm, 1.5 mm, 1 mm, and 0.5 mm for (a)−(d), respectively. The ambient gas-fraction is $O_2 = 20\%$ and the thickness of the electrode is $h = 50$ µm. The grey regions denote the exposed electrode positions. The velocity is normalized by its absolute maximum.*

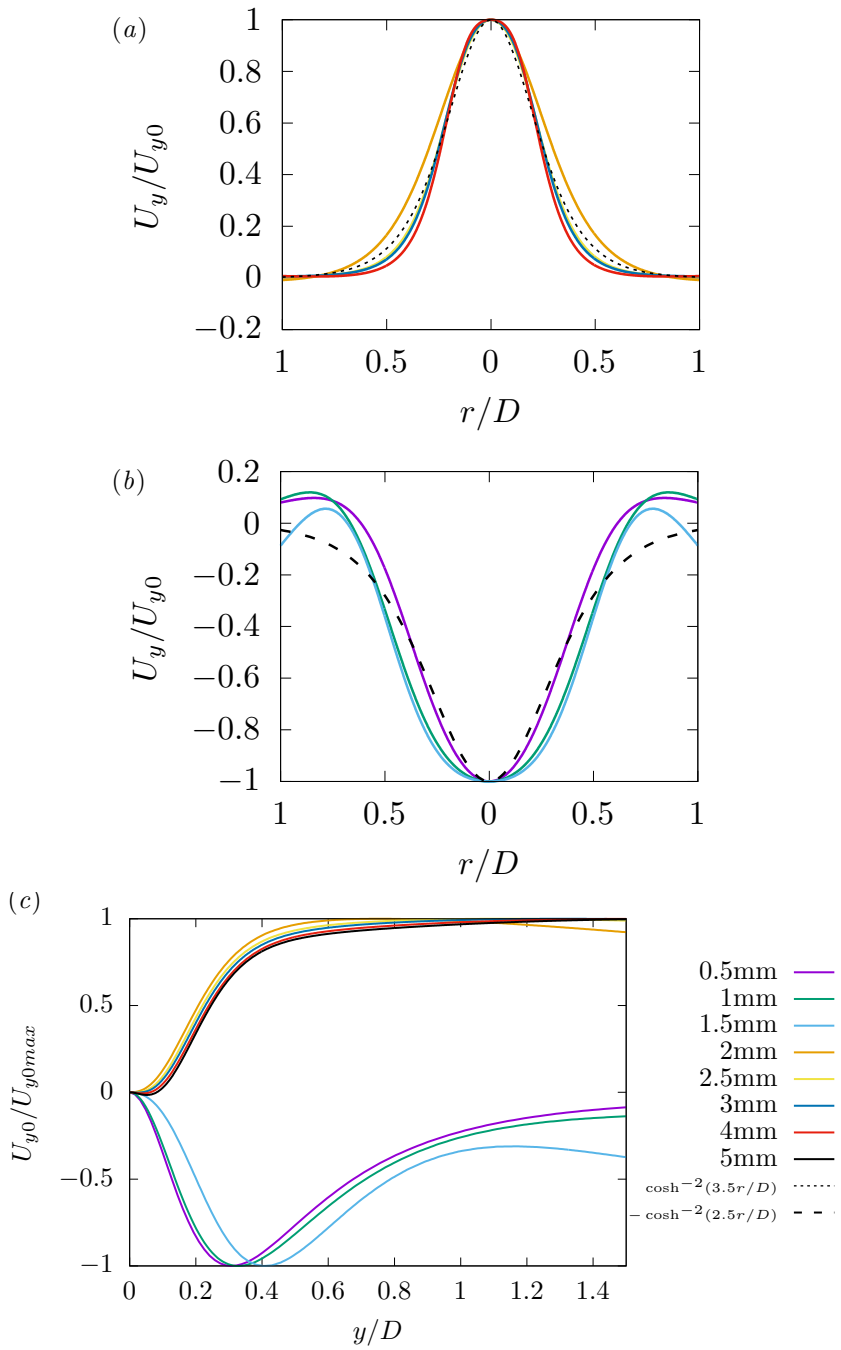

Figure 3.3: *The axial velocity normalized by its absolute maximum at $O_2 = 20\%$, $h = 50\ \mu m$ and $D = 0.5 \sim 5\ mm$. (a) The radial distributions in the outward regime at $y/D = 2$, (b) the radial distributions in the inward regime at $y/D = 0.5$, and (c) the axial distributions at $r = 0$.*

by $\cosh^{-2}(Ar/D)$ with $A = 3.5$, agreeing well with previous works on plasma induced jets [103], as well as mechanical synthetic jets [141]. The inward regimes also show reasonable self-similarity at $y/D = 0.5$ although there is a strong deviation as r/D approaches 1 at the threshold diameter $D = 1.5\ mm$. The axial distribution of the normalised centreline velocity is shown in figure 3.3(c). Once more strong self-similarity between the regimes can be observed. The outward jet accelerates rapidly until approximately $y/D = 0.5$, after which the velocity plateaus. The decay of the centreline velocity is not observed with the domain of our simulation. On the other hand, the inward flow approaches its maximum magnitude at $y/D = 0.35$, then begins to decay.

To examine the development of each jet with the distance from the surface, the cross-sectional distributions of the axial velocity U_y for various D are shown in figures 3.4(a)-(d). Close to the surface, the jets exhibit a double peak structure with the maximum axial velocity occurring off-centre. As the jet develops further from the surface these peaks merge, and the jet becomes fully developed. At $y/D = 0.5$ the inward jet is fully developed with the maximum axial velocity occurring at $r = 0$, whilst the outward jet does not become fully developed until $y/D = 2$.

To quantify the effect of D on the induced flow, the wall-normal velocity distributions are plotted in figure 3.4(e). The maximum outward jet velocity was achieved for $D = 2.5\ mm$, whilst the maximum inward jet velocity was achieved for $D = 0.5\ mm$ (the smallest actuator tested), suggesting a potential for further improvements at smaller diameters. However, in general, the control magnitude is significantly reduced for the inward regime with the representative velocity ($\approx 0.2\ m/s$) significantly below that of the outward regime ($\approx 2\ m/s$), matching well with experiments [38, 140]. It should be noted that the threshold diameter for a reversal in flow direction was found to be less than those found in experiments ($\approx 3 - 5\ mm$) [38, 140], due to the differences in the discharge regime, as well as actuator geometries, dielectric material and operating conditions.

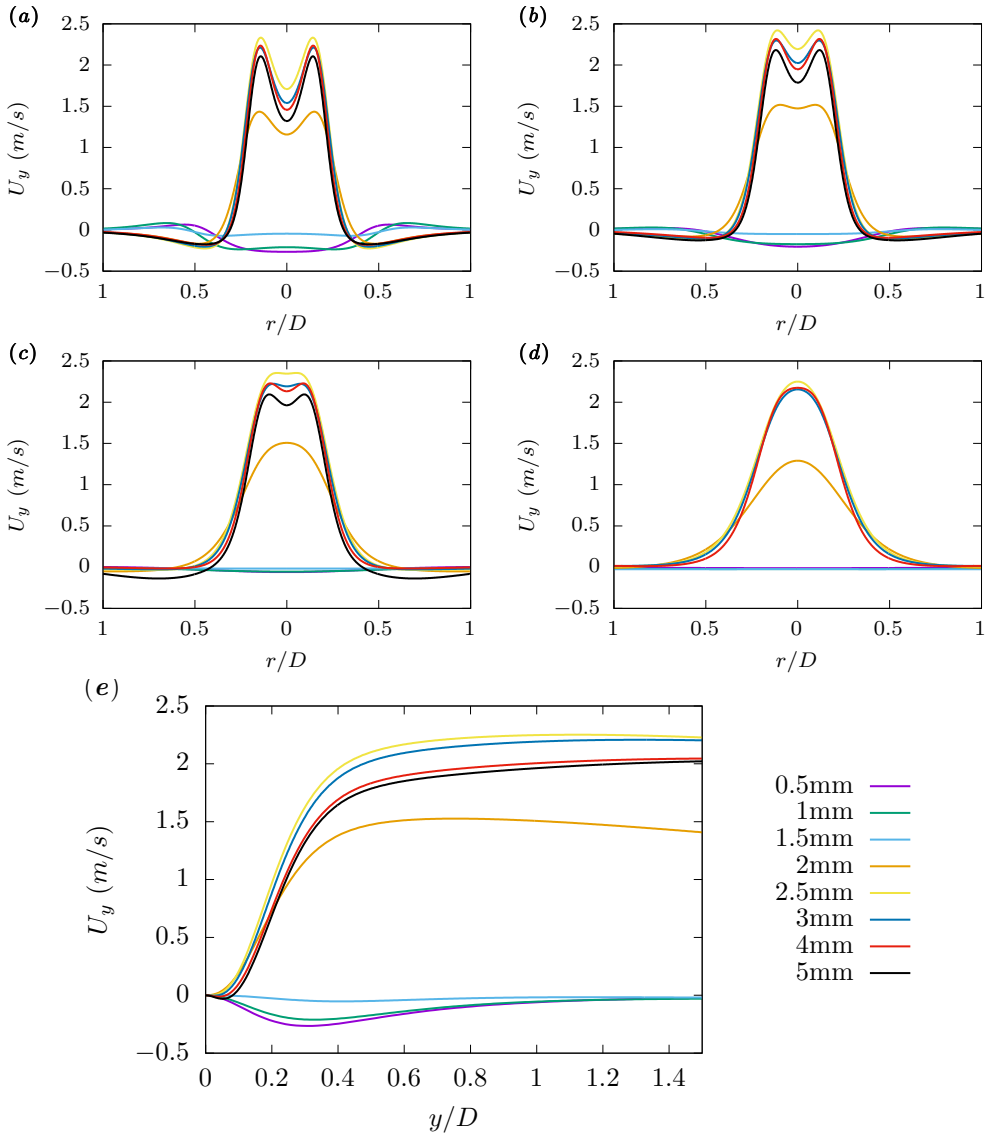

Figure 3.4: *The dimensional axial velocity at* $D = 0.5 \sim 5\ mm$, $O_2 = 20\%$ *and* $h = 50\ \mu m$. *(a)-(d) The radial distributions at* $y/D = 0.3,\ 0.5,\ 1$ *and* 2, *and (e) axial distributions at* $r = 0$.

3.3 Forcing Distributions

As the Navier-Stokes equation is driven by the cycle-averaged EHD forcing term $\bar{\boldsymbol{F}}$, the flow reversal has to be from the variation of the forcing. In this section, the spatial distribution of this forcing will be examined to track the flow reversal.

The cycle-averaged radial and axial EHD forcing distributions denoted as $\overline{F_r}$ and $\overline{F_y}$ are shown in figure 3.5 for annular actuators of different diameters. It is apparent that there are opposing regions of substantial forcing in close proximity. As there is an overlap for each forcing component, it can be useful to define two principal regions: the "inward forcing" with $\overline{F_r} > 0$ and $\overline{F_y} > 0$ located close to the exposed electrode edge, and the "outward forcing" with $\overline{F_r} < 0$ and $\overline{F_y} < 0$ along the dielectric surface. If imposed independently, the inward forcing would produce an axial jet towards the actuator whilst the outward forcing would produce an axial jet away from the actuator. Therefore the competition between these two forcings results in the two distinct flow regimes. As the actuator diameter drops below 2 mm, there is a significant suppression of the outward forcing, whilst the inward forcing expands, albeit to a lesser extent, resulting in the eventual domination of the inward forcing. We also note a small region of negative axial forcing at the corner of the exposed electrode, which is also suppressed at small diameters.

The forcing components of figure 3.5 are then integrated over the entire domain. As shown in figure 3.6, for DBD plasma actuators with large diameters, both the spatial-integrated radial and axial forcing components are negative and approximately constant with diameter, with the radial forcing significantly larger. As such, large diameter actuators produce outward jets as they generate a negative radial forcing. However, as the actuator diameter decreases below 2 mm there is a sudden decrease in the magnitude of both the negative radial and negative axial forcing components, leading to a positive net radial forcing, and a small negative net axial forcing. Here the two opposing forcings

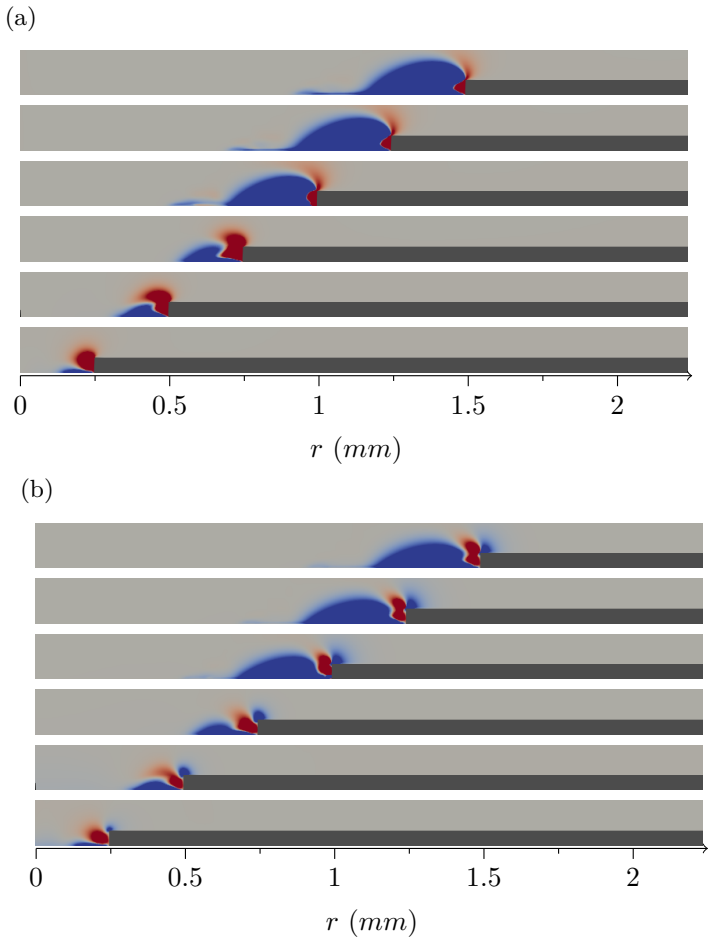

Figure 3.5: *Cycle-averaged distributions of (a) radial EHD forcing component* $\overline{F_r}$ *and (b) axial EHD forcing component* $\overline{F_y}$ *for actuators with* $h = 50$ μm *and* $O_2 = 20\%$. *The thickness is* $D = 0.5$, 1, 1.5, 2, 2.5, *and* 3 mm *from top to bottom. Red:* ≥ 10 $kNmm^{-3}$, *Blue:* ≤ -10 $kNmm^{-3}$.

are closer in magnitude, suggesting that the actuators become inefficient in generating the control, which will be further discussed in §4.4.

3.4 Discharge Structure

By their nature DBD discharges are cyclical and largely antagonistic. Therefore, to fully understand how this forcing topology is generated it is important to investigate how the forcing varies over an AC cycle as shown in figure 3.7. There are two periods of significance: the positive-going positive quarter cycle and the negative-going negative quarter cycle. These periods are termed the "positive discharge" and "negative discharge", respectively. During both periods, the potential difference across the electrode is continuously increasing allowing for successive discharges to occur and then subsequently be quenched by a build-up of dielectric surface charge. However, it is the imbalance of these discharges which leads to the resultant EHD force [18]. Due to the relatively low applied voltage used in this study, transition to a streamer regime, where the developed space charge generates a significant additional electric field resulting in a 3D finger-like discharge structure, was not observed in our investigation [142].

The discharge in the positive sub-cycle becomes intermittent for small diameter plasma actuators. Whereas, for large diameter annular actuators there is a continuous smooth positive glow regime unless interrupted by streamer discharges (which only occur above a threshold applied voltage). In contrast the negative discharge is always dominated by a small number of successive microdischarges. As the diameter decreases these microdischarges become more numerous and less intense. For small diameter actuators, the increased fragmentation of the positive discharge produces a greater reduction in the radial forcing magnitude leading to the cycle forcing being dominated by the negative discharge.

To explain the different discharge characteristics during the positive and neg-

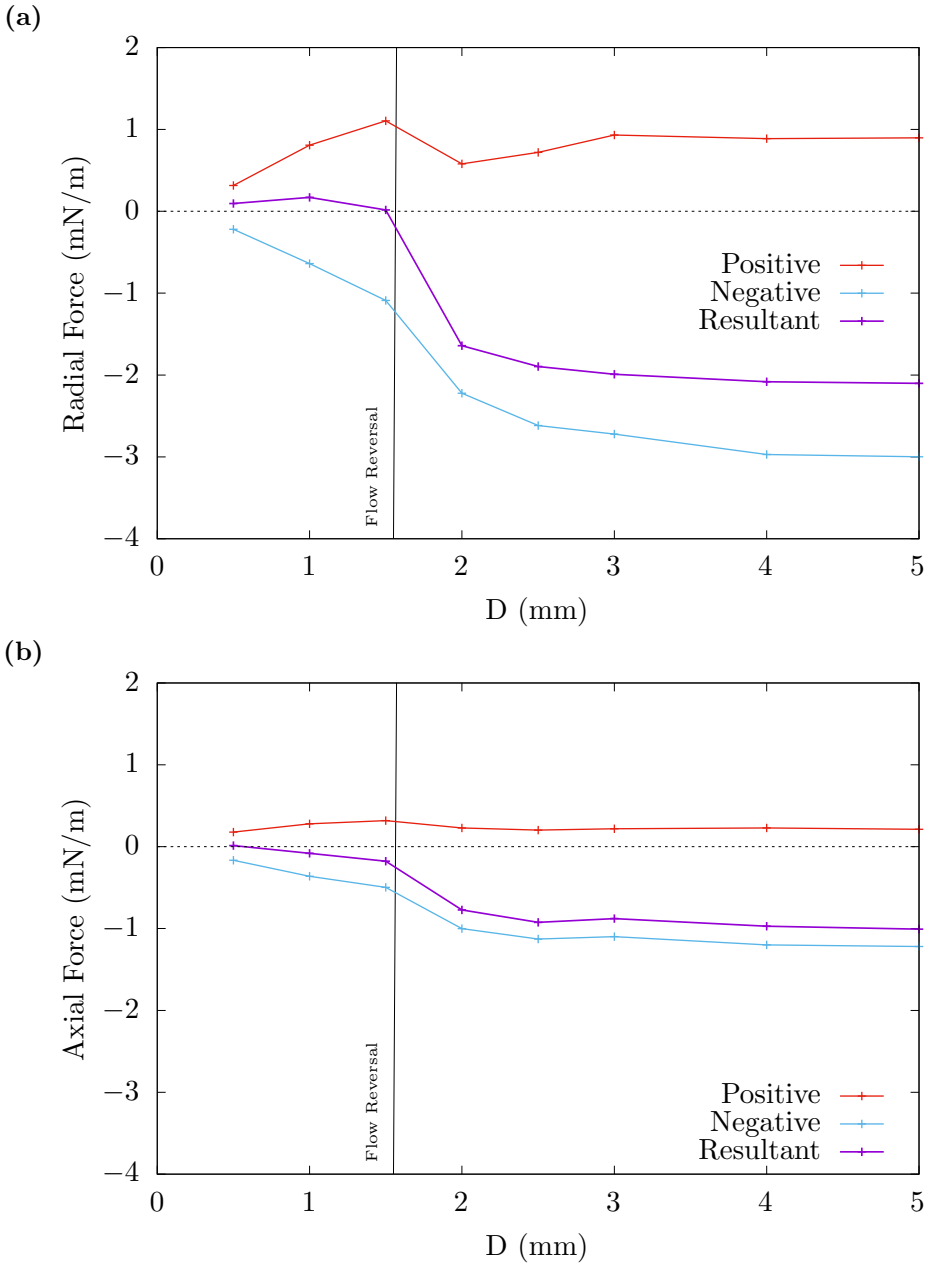

Figure 3.6: *Cycle-averaged and space-integrated (a) radial and (b) axial forcing components with $h = 50$ μm, $O_2 = 20\%$ and various diameter. Each forcing is broken into a positive and a negative component.*

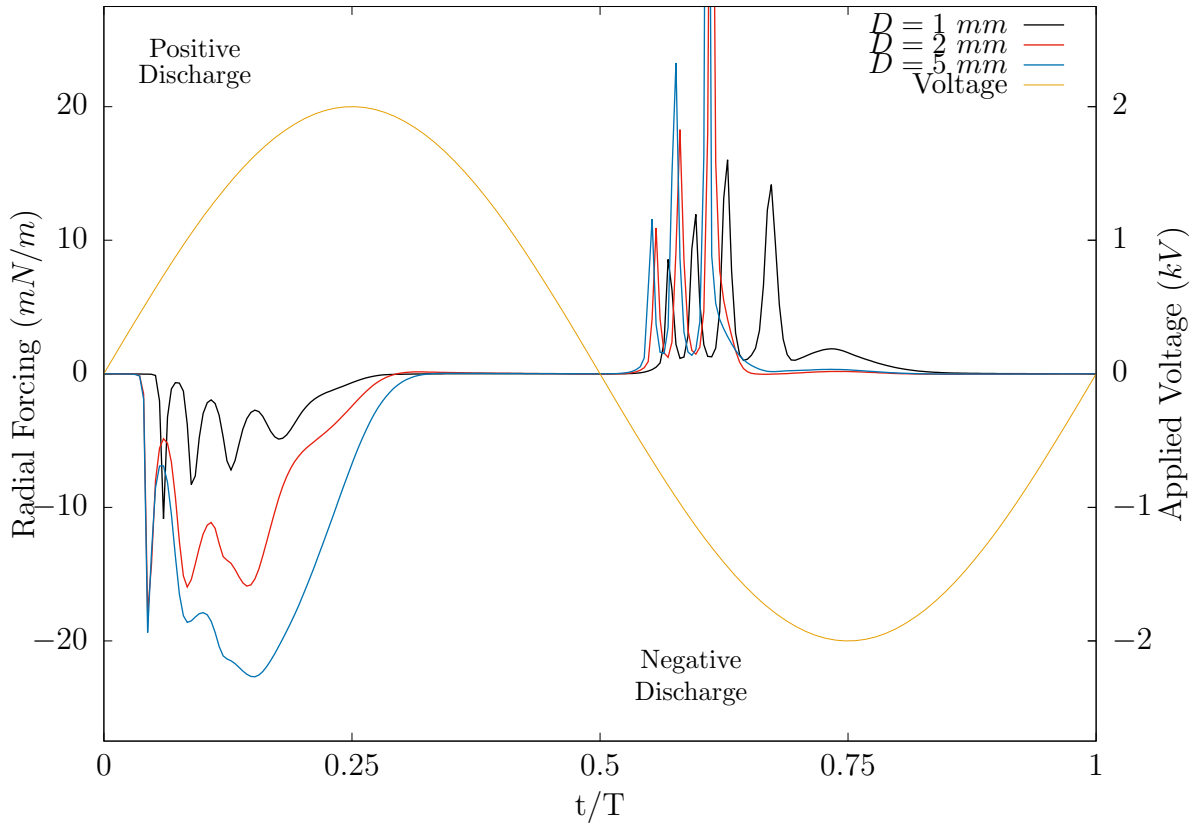

Figure 3.7: *Radial EHD forcing per unit circumference over a single AC cycle, with excitation voltage represented by the yellow line.*

ative discharge, it is useful to decompose the cycle-averaged EHD Forcing distribution $\boldsymbol{F}$ into the contributions of the different species as

$$\boldsymbol{F} = (n_+ - n_- - n_e)e\boldsymbol{E} = \boldsymbol{F_+} + \boldsymbol{F_-} + \boldsymbol{F_e} \tag{3.1}$$

where n_i is the number density of the i-th species, e is the atomic unit of charge, and $\boldsymbol{E}$ is the instantaneous electric field. The forcing field can then be averaged over each quarter-cycle. Figure 3.8 shows the forcing contributions of the positive ions $\boldsymbol{F_+}$ and negative ions $\boldsymbol{F_-}$, as well the combined contributions of all species $\boldsymbol{F}$, averaged over the positive and negative discharges. The forcing contribution from the electrons is found to be small, so is not included for brevity.

During the positive discharge, a positive ion cloud expands along the dielectric surface generating a large negative radial forcing volume. Simultaneously, the negative ions are driven towards the electrode contributing to the positive radial forcing. However, due to the larger number of positive ions, the negative radial forcing dominates the positive sub-cycle. Conversely, during the negative sub-cycle, the highly mobile electrons charge the dielectric much more rapidly, repeatedly quenching the discharge. This leads to short repetitive cycles of localised discharge formation and extinction. In this sub-cycle, we observe the positive ions are responsible for the majority of the forcing, and therefore this sub-cycle is dominated by localised positive radial forcing. Crucially, as the diameter is increased, we observe a large difference in forcing volume during the positive discharge, whilst only a limited change during the negative discharge. Whilst more negative ions are present during both the positive and negative sub-cycles for the $D = 3\ mm$ diameter case. The positive discharge has the largest increase in the forcing volume contributed by the negative ions compared to the 1 mm case. This leads to a more antagonistic forcing, with regions of positive radial forcing forming near the electrode edge.

An alternative way to visualise a discharge is a Lissajous or VQ plot as shown in

(a) The Positive Discharge

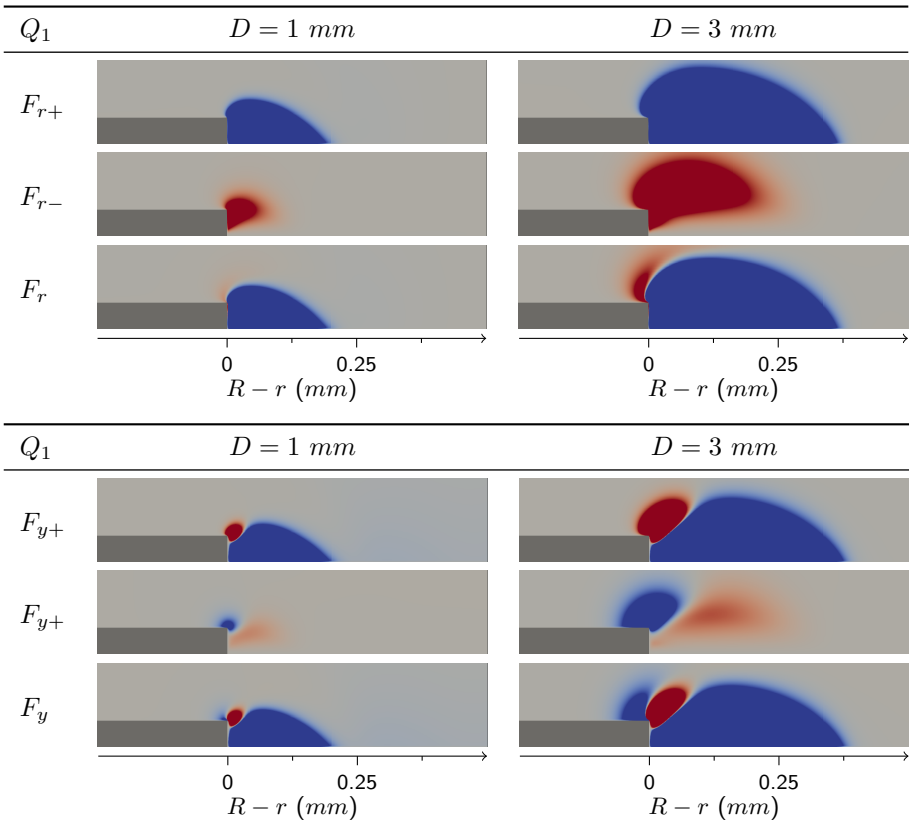

(b) The Negative Discharge

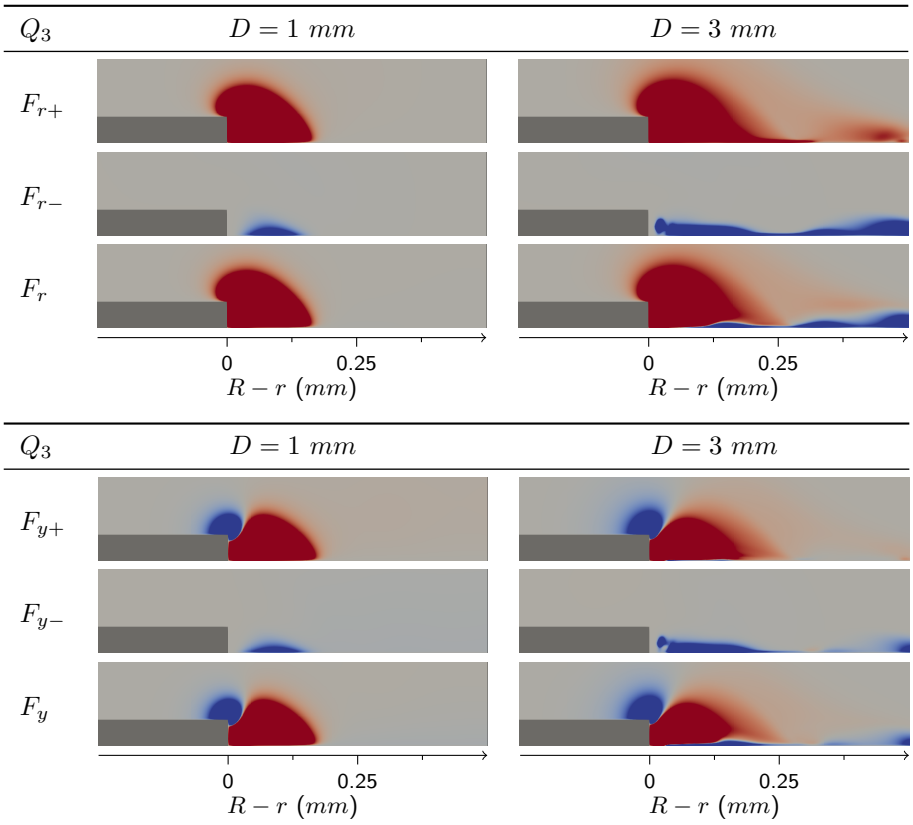

Figure 3.8: *The forcing contributions of the positive (F_+) and negative (F_-) ions to the total induced EHD force (F), averaged over (a) the positive discharge and (b) the negative discharge for both the $D = 1\ mm$ and $D = 2\ mm$ cases.*

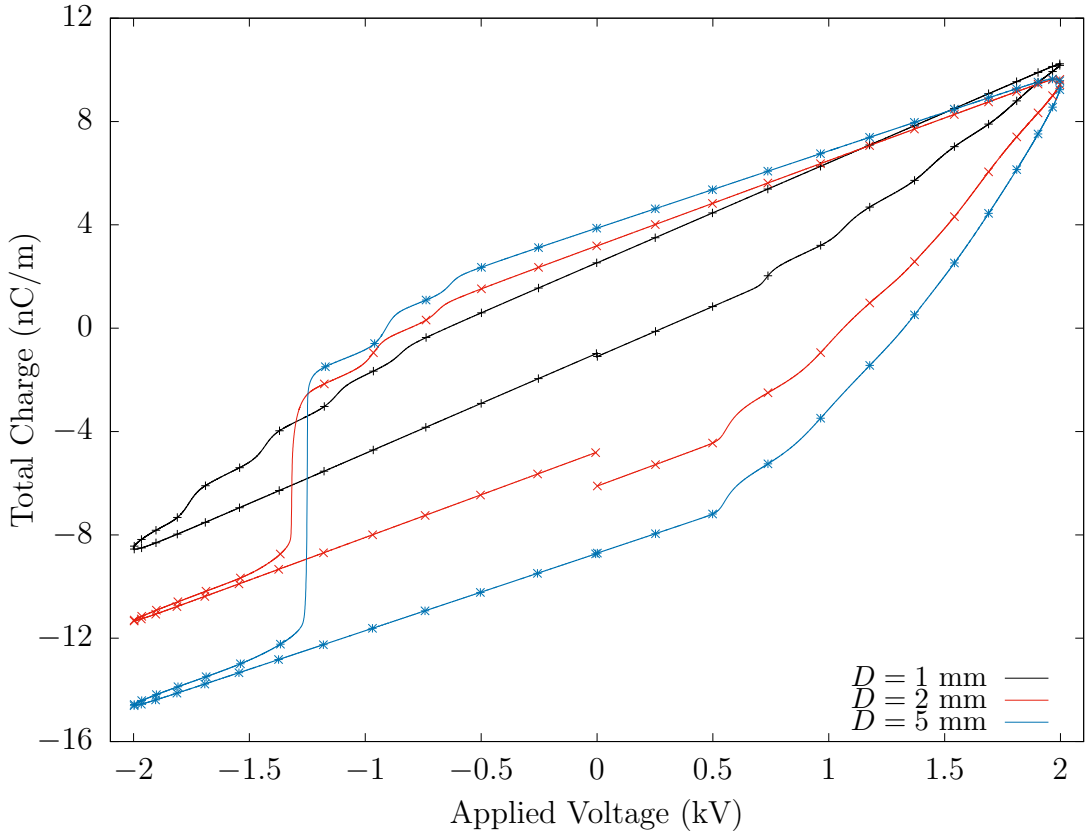

Figure 3.9: *Total charge against applied voltage over a single AC cycle with* $h = 50\mu\ m$ *and* $O_2 = 20\%$

figure 3.9 [143]. Here, the total charge is calculated by cumulatively integrating the current, whilst the voltage is taken from the applied boundary conditions. When the imposed electric field is too small for plasma generation, the actuator acts as a capacitative cell and the total charge varies linearly with the applied voltage. However, if the voltage amplitude increases enough for the electrical breakdown of air to occur, the gradient increases, and for a filamentary DBD discharge such a plot forms a parallelogram. For a glow regime discharge, the small number of current pulses mean that this parallelogram becomes increasingly stepped [144]. The area enclosed by the parallelogram gives the energy dissipated per cycle, while effective capacitances can be calculated from the plot gradients.

The most obvious difference between different diameter actuators is the presence of the increasingly intense microdischarges during the negative subcycle for outward-flow cases ($D = 2$ and $5\ mm$). The extra negative charge on the dielectric from these intense microdischarges causes the electrical breakdown of air, and subsequently the gradient increase to occur slightly earlier ($\approx 0.5\ kV$) for large diameter cases compared to $\approx 0.6\ kV$ for small diameter cases. After the breakdown, the dielectric begins to charge until a maximum value is reached. For small diameter actuators the negative cycle is largely symmetric with the positive discharge. On the other hand, for large diameter actuators the microdischarges are significantly more energetic, rapidly charging the dielectric. The extent of the negative charging of the dielectric is determined by the discharge intensity, which increases with actuator diameter. Despite their intensity, these microdischarges did not significantly increase the average positive radial forcing component due to their short timescales. This is consistent with previous observations that the low-current glow regime, rather than high-current microdischarges, is responsible for the majority of EHD force production in a DBD discharge [145]. The presence of these intense microdischarges also prevents the cycle being perfectly periodic, as their intensity oscillates aperiodically, leading to small discontinuities in the VQ plot. To ensure the

cycle is representative of periodic steady state, for all cases the cycle-averaged dielectric surface charge was examined to ensure it fulfilled the steady-state criterion described in section 2.6. Figure 3.10 examines the total surface charge over five AC cycles for a 1 mm and 5 mm diameter annular DBD actuator. The 1 mm diameter case achieves a periodic steady state very quickly, and by the second period is representative of periodic steady state. Meanwhile, for the 5 mm diameter case, the discharge takes a number of cycles to achieve periodic steady state.

The deposited dielectric surface charge is initialised at zero at the start of the simulation. Whilst the absence of residual negative charge on the dielectric, reduces the initial positive discharge, it also allows for the dielectric to be charged strongly, leading to a more intense negative discharge. This process continues, with the intensity of each discharge increasing due to the increased deposition of charge from the previous cycle, until an equilibrium is reached. In this work, steady state is said to be achieved when there is less than a 2% change in the cycle-averaged total surface charge, therefore the third period of the 1 mm diameter case was used, whilst the fifth period was used for the 5 mm diameter case.

Although the intense microdischarges identified in figure 3.9 do not appreciably modify the resultant forcing, the dielectric surface charging changes significantly. Figure 3.11 shows how the surface charge is distributed across the dielectric after each period of activity. The discharge propagation in both subcycles is suppressed for smaller diameter actuators. However, the presence of residual positive/negative charge from the previous discharge cycle indicates that the positive discharge propagates further than the negative discharge for small diameter actuators. Whereas the opposite is true for actuators where $D \geq 2\ mm$. The increased propagation of the negative charging for large diameter actuators is a result of the microdischarges rapidly charging the dielectric. As intense microdischarges are not present for smaller diameter actuators, the diffuse positive ion cloud generated during the positive discharge propagates

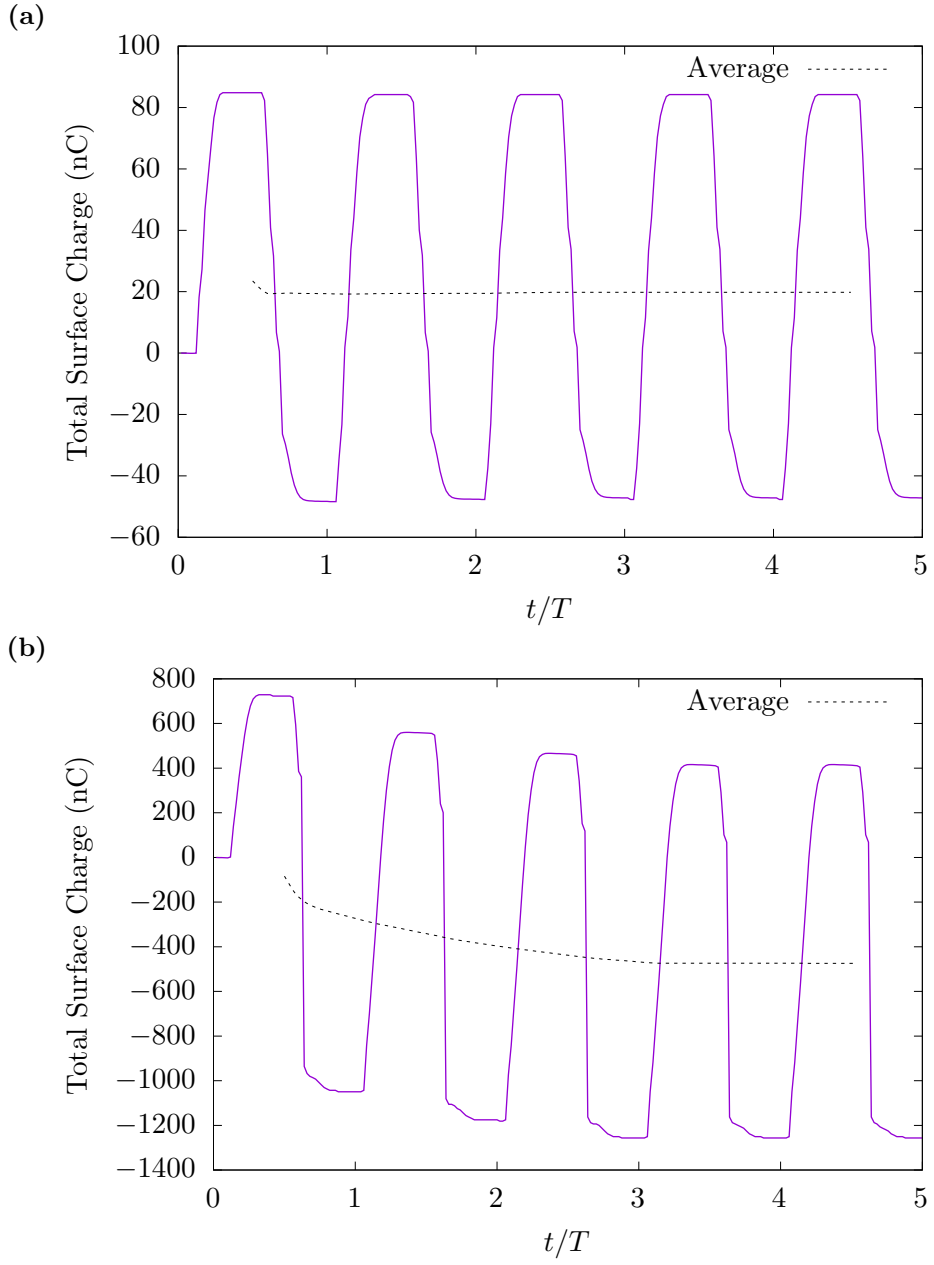

Figure 3.10: *The total surface discharge of (a) 1 mm and (b) 5 mm diameter annular DBD actuator over the first 5 AC cycles of an applied sinusoidal voltage ($V_{max} = 2kV$, $f = 40kHz$). The periodic rolling average is shown by the dashed black line*

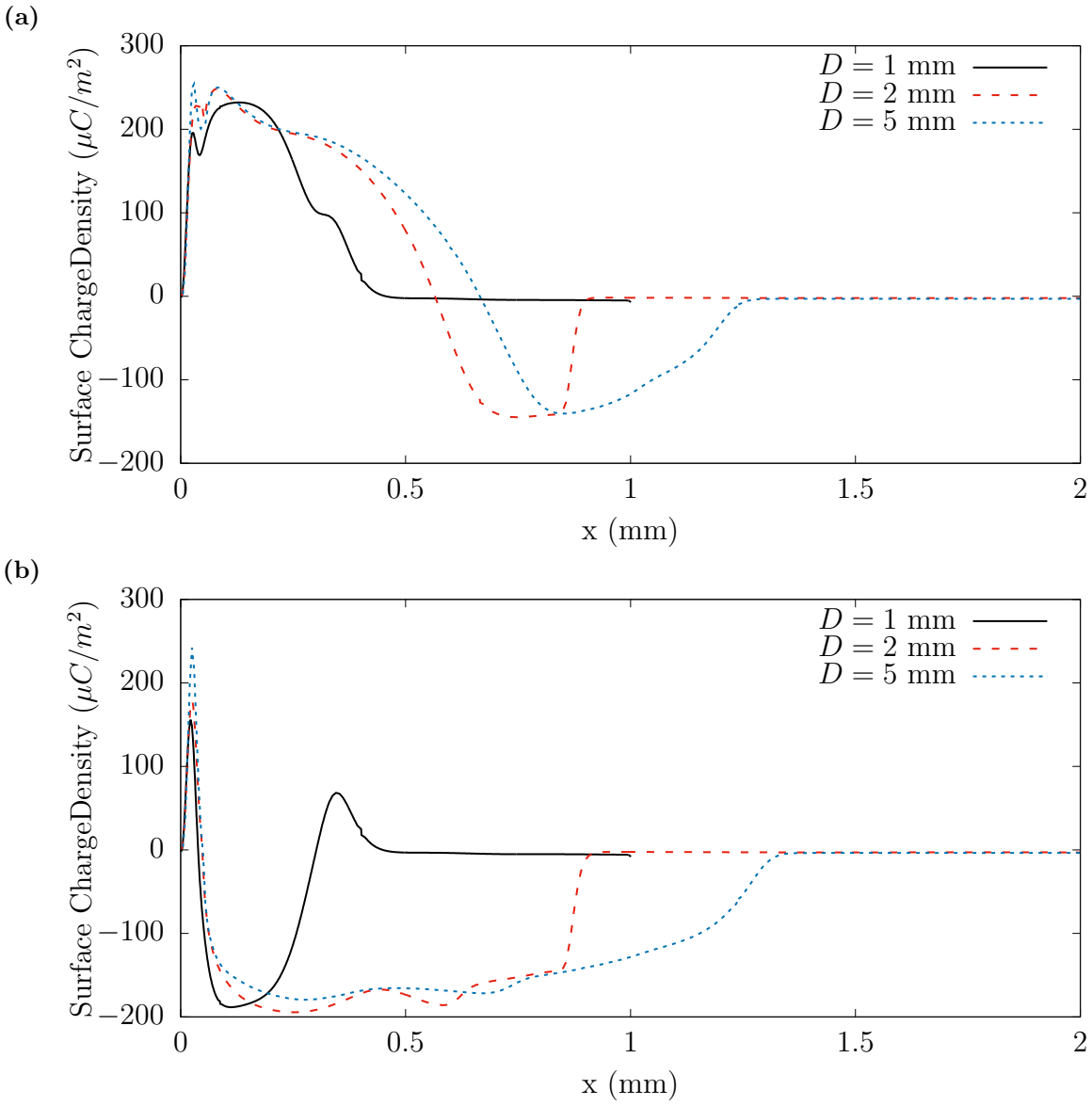

Figure 3.11: *Spatial distributions of surface charge of different diameter actuators at (a) $t = T/4$ and (b) $t = 3T/4$. Where x is the distance from the exposed electrode edge.*

further along the surface than the equivalent negative discharge. The extent of this propagation is reduced for smaller diameter actuators, due to the repetitive quenching of the positive discharge.

Figure 3.12 examines how the maximum extent of each discharge changes with diameter. As the diameter increases, both the positive and negative discharges propagate further. However, at 1.5 mm (the threshold for flow reversal) there is a much more significant increase in the propagation of the negative discharge. This increase in propagation is due to the formation of the intense and

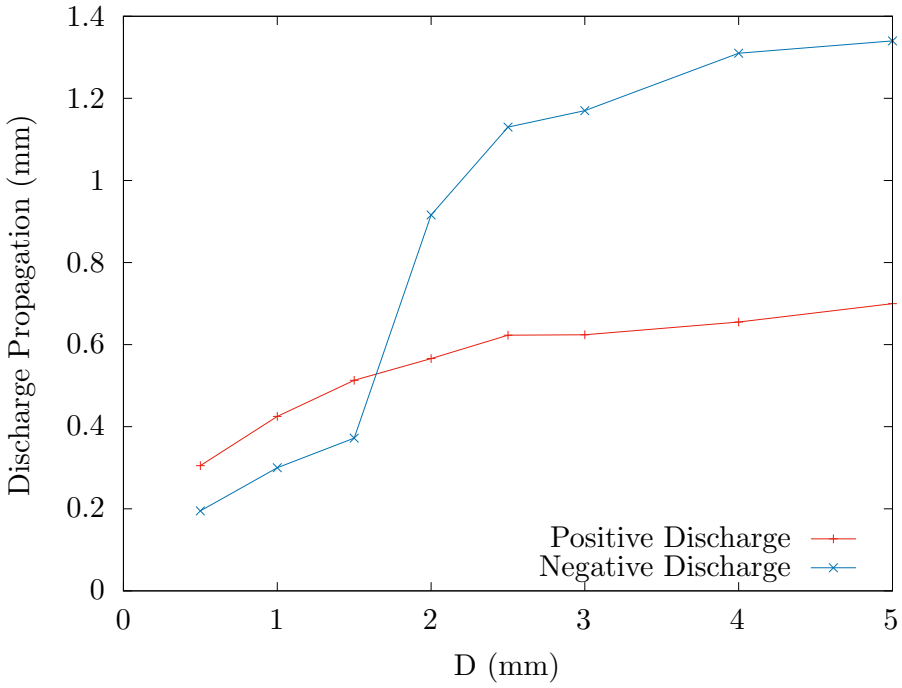

Figure 3.12: *Maximum extent of discharge propagation against actuator diameter D*

constricted microdischarges during the negative discharge. The constricted nature of these intense microdischarges allow for the surface charging to be increased without significantly increasing the forcing volume during the negative discharge as shown in figure 3.8. However, this increase of negative charge deposited on the surface, increases the potential difference and delays quenching during the subsequent positive discharge. This leads to an increase in the forcing volume produced during the positive discharge. At large diameters, the propagation of both discharges plateaus, indicating there will be consistent behaviour for larger actuators.

At constant applied voltage profile, gas properties, and dielectric constant, these changes in discharge structure come from the electric field modification caused by geometrical differences in the actuator layout.

As the DBD discharges are advection dominated, especially at high frequencies, the current density can be well approximated by a scalar multiple of the electric field. We denote the current density as $\boldsymbol{J} = \{J_r, J_y\}$, where J_r and J_y are the radial and axial components, respectively. As the actuator diameter

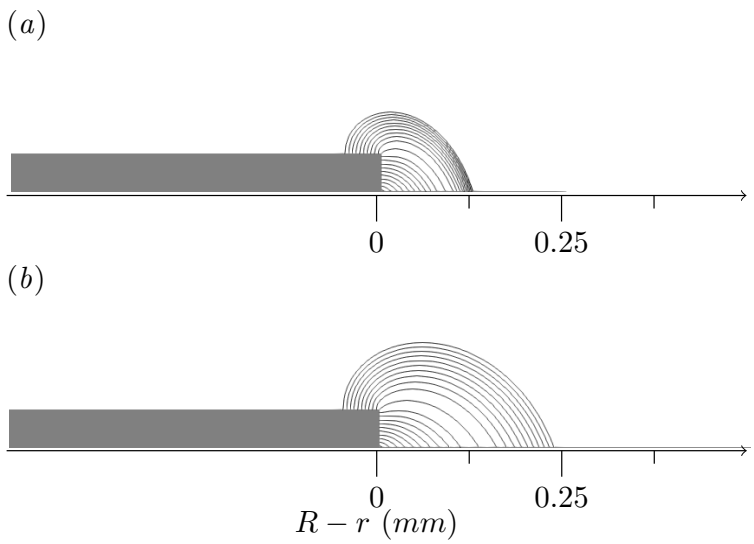

Figure 3.13: *The electric field lines for annular DBD actuators with* $h = 50\ \mu m$*,* $O_2 = 20\%$ *and (a)* $D = 0.5\ mm$ *and (b)* $D = 5\ mm$*.*

decreases, the electric field lines become increasingly curved (see figure 3.13), directly affecting the proportion of these current density components. Figure 3.14 shows that as the actuator diameter decreases, the increased curvature of the electric field lines increases the proportion of the current driven towards the surface. This leads to a relative increase in J_y and the rate of dielectric charging, whilst the proportion of charge driven downstream from the electrode decreases.

It is suggested that this affects the positive and negative discharges unevenly. For the negative discharge the increased charging quenches the electric field, reducing the microdischarge intensity, which dramatically reduces the extent of dielectric charging below $D = 2\ mm$. However as the short-timescales of microdischarges prevent effective force generation, the development of less intense and more numerous current and forcing peaks leads to a limited reduction in the positive radial forcing. On the other hand, the more rapid build-up of surface charge repeatedly quenches the positive discharge, making it increasingly intermittent for small diameter actuators. This reduces the time the positive ion cloud can propagate along the dielectric surface, significantly reducing the space charge volume and thus the EHD forcing volume. The overall result is a positive radial force led by the negative discharge which dominates the cycle

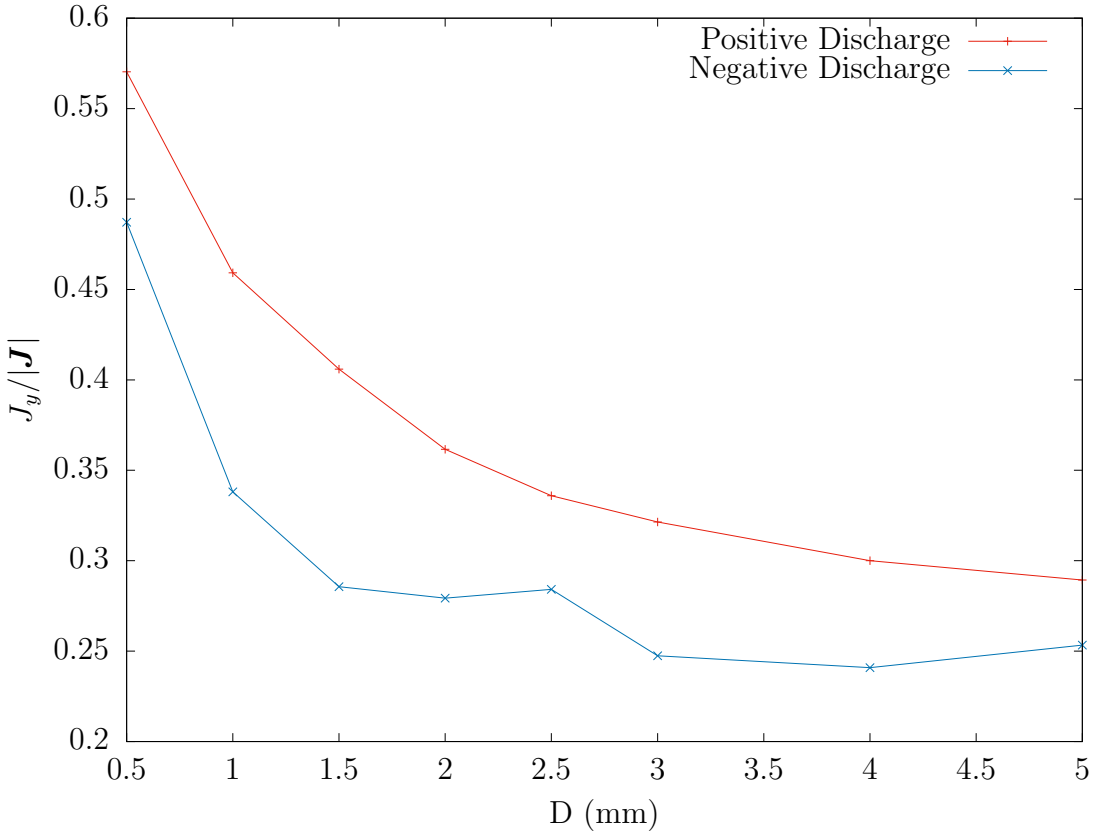

Figure 3.14: *The proportion of the total current which is directed axially for different diameter actuators*

for small diameter actuators.

3.5 Concluding Remarks

The flow reversal effect initially identified by [38] has been investigated using a 4-species numerical model, and the underlying mechanism revealed. It is confirmed that the reversal of flow direction over small diameter DBD actuators results from a change of discharge structure. For millimetric annular DBD actuators there exist regions of opposing forcing in close proximity that are generated during the two significant periods of an AC cycle, resulting in two distinct flow regimes. These periods are the positive-going positive one and the negative-going negative one, which are dominated by the negative and positive radial EHD forcing, respectively. It is found that the radial forcing dictates the direction of the axial jet, with negative radial forcing leading to an outward jet, and positive radial forcing leading to an inward jet. The inward jet was characterised as having a reduced magnitude (approximately 10% of the outward jet), and significantly reduced vertical penetration. It is considered that the mechanism behind the reversal of axial flow is the increased field line curvature of small diameter actuators, which leads to a relative increase in the dielectric charging and increased quenching. This impedes ion cloud growth over the surface during the positive sub-cycle, and reduces microdischarge intensity during the negative sub-cycle. The reduced microdischarge intensity has a limited effect on the positive radial force generated during the negative sub-cycle, but significantly reduces the negative charging of the dielectric. Both were found to suppress the negative radial forcing generated during the positive sub-cycle resulting in a net positive radial cycle-averaged force and thus the development of the inward jet.

Chapter 4

Parameter Study of Millimetric Annular DBD Plasma Actuators

4.1 Introduction

The sensitivity of DBD plasma actuator performance to operating conditions and actuator geometry has been widely discussed in literature [146, 147]. In order for millimetric annular plasma actuators to effectively be deployed, their performance across a range of operating conditions must be understood. In this section two parameters: the electrode thickness h, and the oxygen gas-fraction O_2 are independently varied, to identify their effect on actuator performance. These parameters have been less studied than, for example, changes to the applied voltage profiles, and it is by examining their effects on the underlying discharge structure, that new insights into the mechanisms of both millimetric and non-millimetric DBD plasma actuators can be developed. Chapter 3 has demonstrated that the scale of an annular DBD plasma actuator can significantly affect the discharge mechanics. Two base cases are therefore utilised, one operating in an inward configuration ($h = 50\ \mu m$, $O_2 = 20\%$, $D = 1\ mm$) and one operating in an outward configuration ($h = 50\ \mu m$, $O_2 = 20\%$, $D = 2\ mm$). Section 4.2 details how modifications to the exposed electrode thickness h affect the different aspects of the discharge structure and

resulting flow fields for both base cases. Section 4.3 then undertakes a similar investigation for the oxygen gas-fraction. Finally, section 4.4 summarises how key performance parameters vary with D, h, and O_2.

4.2 The Effect of Electrode Thickness on the Discharge Structure

One of the advantages of DBD actuators is their low-profile. The thickness of the exposed electrode in the previous chapter is 50 μm, significantly larger than those used in experiments (down to $\approx$ 1 μm) due to numerical limitations. The local field approximation is used, the validity of which is limited when the spatial resolution drops much below 1 μm, and the electron energy is transported between cells. Despite this numerical limitation preventing accurate simulation down to a 1 μm thickness, it is important to investigate how such a change in geometry would affect the discharge, above and below the threshold of axial flow reversal. In this section therefore, an investigation into the effect of reducing the electrode thickness from 50 μm down to 10 μm had on both a 1 mm and a 2 mm diameter annular DBD actuator was carried out. During the investigation, it was found that a reversal from an inward jet to an outward one can be induced at a constant diameter by reducing the electrode thickness h. As shown in figure 4.1, where $D = 1$ mm and $O_2 = 20\%$, the flow transitions from an inward flow regime at $h = 50$ μm to an outward flow regime at $h \leq 15$ μm. At $h = 25$ μm, recirculation zones near the exposed electrode edge are formed and spread across the surface until the axial flow direction reverses.

There are some differences between the velocity fields of outward flow regimes at low electrode thicknesses and those of the larger diameter cases as shown in figure 3.2. Instead of being drawn tangentially from close to the surface, the flow has a significant wall-normal component forming a vortex close to

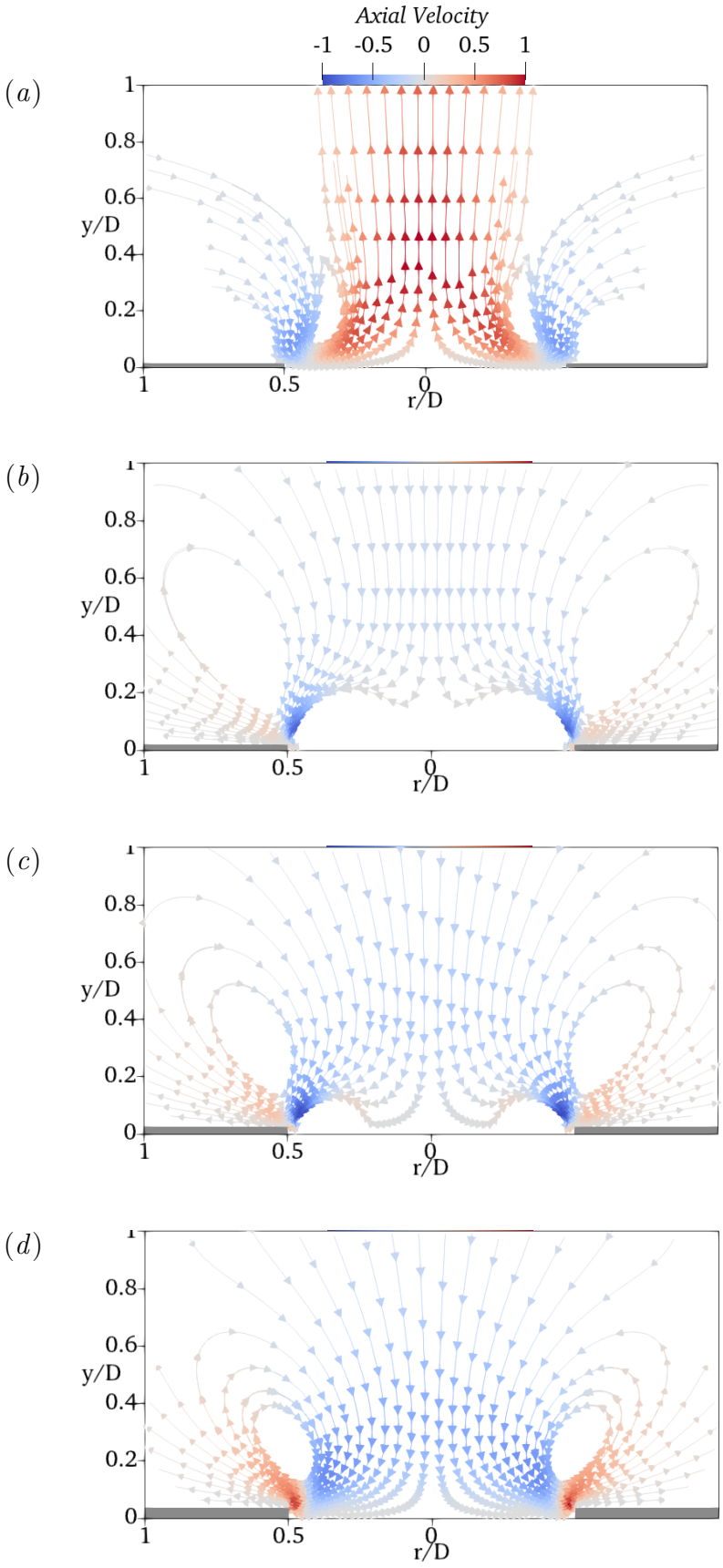

Figure 4.1: *The axisymmetric flow induced by annular DBD actuators operating at* $O_2 = 20\%$ *with* $D = 1$ *mm and* $h = 15$ μm, 20 μm, 25 μm *and* 50 μm *for (a)−(d), respectively. The grey regions denote the exposed electrode positions. The velocity is normalized by its absolute maximum.*

the electrode edge. However, no reversal was observed in the flow field of the 2 mm diameter actuator, as the exposed electrode thickness was reduced. The figures for the 2 mm diameter actuator are therefore omitted for brevity.

The variation of the cycle-averaged EHD forcing with respect to the electrode thickness h is examined for both the $D = 1$ mm and $D = 2$ mm cases, and shown in figures 4.2 and 4.3, respectively. As in Chapter 3, we identify an inward forcing region, where both the axial and radial components are positive encouraging an inward axial flow, as well as an outward region where both the axial and radial forcing are negative encouraging the development of an outward jet. For the $D = 1$ mm case, as h reduces, the outward forcing region increases, whilst the inward forcing reduces slightly, similar to the trend as D is increased (shown in figure 3.5). At $h = 15$ μm, there is a sudden growth of both regions, however, as the outward forcing region increases significantly more, this results in the dominance of the outward flow regime and the reversal of the axial jet. A small region of negative axial forcing at the electrode edge is also observed. At small h this region grows disproportionately compared to the inward forcing and accounts for an increased entrainment behaviour as shown in figure 4.1.

For the $D = 2$ mm case, a reduction in h leads to an increase in both the inward and outward forcing, with a sudden increase in both forcing volumes observed at $h = 20$ μm. However, as the thickness is reduced to $h = 10$ μm, the volumes of both forcing volumes reduce slightly. The region of negative axial forcing is again observed near the electrode edge, and grows disproportionately as h is reduced.

For a more quantitative investigation, these cycle-averaged forcing distributions are integrated over the entire domain and are shown in figures 4.4 and 4.5, respectively. Here key differences can be observed between the $D = 1$ mm and $D = 2$ mm cases. For the $D = 1$ mm case, there is only a limited increase in the inward forcing at small h, which is overcompensated by the large increase in the outward forcing. Meanwhile, for the $D = 2$ mm case, the in-

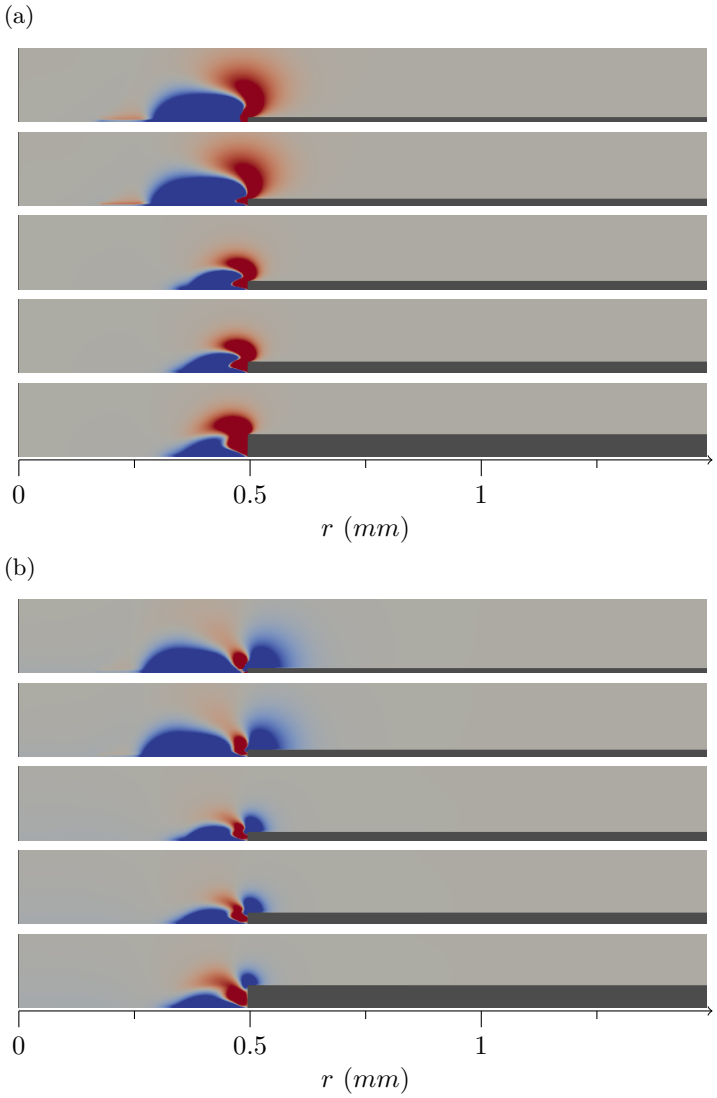

Figure 4.2: *Cycle-averaged distributions of (a) radial EHD forcing component* $\overline{F_r}$ *and (b) axial EHD forcing component* $\overline{F_y}$ *with* $D = 1$ *mm and* $O_2 = 20\%$*. The electrode thickness is* $h = 10$ *μm, 15 μm, 20 μm, 25 μm, and 50 μm from top to bottom. Red:* ≥ 10 $kNmm^{-3}$*, Blue:* ≤ -10 $kNmm^{-3}$*.*

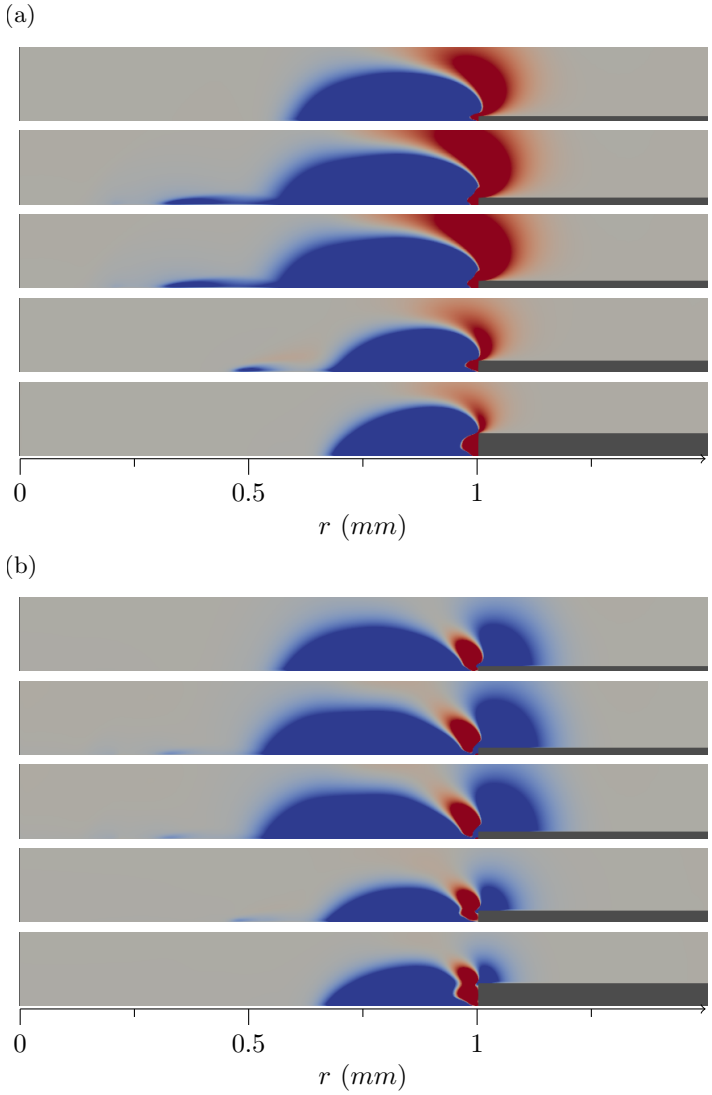

Figure 4.3: *Cycle-averaged distributions of (a) radial EHD forcing component* $\overline{F_r}$ *and (b) axial EHD forcing component* $\overline{F_y}$ *with* $D = 2$ *mm and* $O_2 = 20\%$*. The electrode thickness is* $h = 10$ μm*,* 15 μm*,* 20 μm*,* 25 μm*, and* 50 μm *from top to bottom. Red:* ≥ 10 $kNmm^{-3}$*, Blue:* ≤ -10 $kNmm^{-3}$*.*

crease in the inward forcing is proportionately more significant, leading to a reduction in the resultant forcing.

For a more detailed examination of the discharge, the forcing contributions of each species during each sub-cycle were calculated, as described in §3.4. Figures 4.6 compares these contributions for the $h = 10\ \mu m$, $D = 1\ mm$, $O_2 = 20\%$ and the $h = 50\ \mu m$, $D = 1\ mm$, $O_2 = 20\%$ cases. As the thickness is reduced, there is a significant increase in the volume of both positive and negative ions during the positive discharge. Meanwhile, there is limited change in the forcing volumes generated during the negative half-cycle.

Figure 4.7 shows the same decompositions for the $D = 2\ mm$ case. In a similar manner to the $D = 1\ mm$ case, the majority of the increased forcing volume generated during the positive discharge, whilst there is only a limited change in the forcing volume generated during the negative cycle. However, in this case a much larger volume of negative ions was produced during the positive sub-cycle. This lead to the resultant forcing decreasing with reducing thickness for the $D = 2\ mm$ case, instead of increasing as for the $D = 1mm$ case. In both cases, the region close to the electrode edge sees an increase in negative ions during the positive discharge. Combined with the increase in positive ions during the negative discharge, this leads to the growth of the negative axial forcing region, resulting in the increased entrainment behaviour identified in figure 4.1.

It is proposed that the cause of this change in discharge structure is that the thinner electrode leads to an increased local maxima at the sharp electrode corner. This increases the local production of ions and therefore encourages a more energetic discharge. As with the larger diameter cases illustrated in Chapter 3, this leads to a significant increase in the intensity of the negative-cycle microdischarges, making the negative cycle discharge more intermittent, but increasing the volume of the subsequent positive cycle discharge. The stronger local electric field near the electrode edge also leads to the increased production of negative ions, and thus the increased positive radial forcing

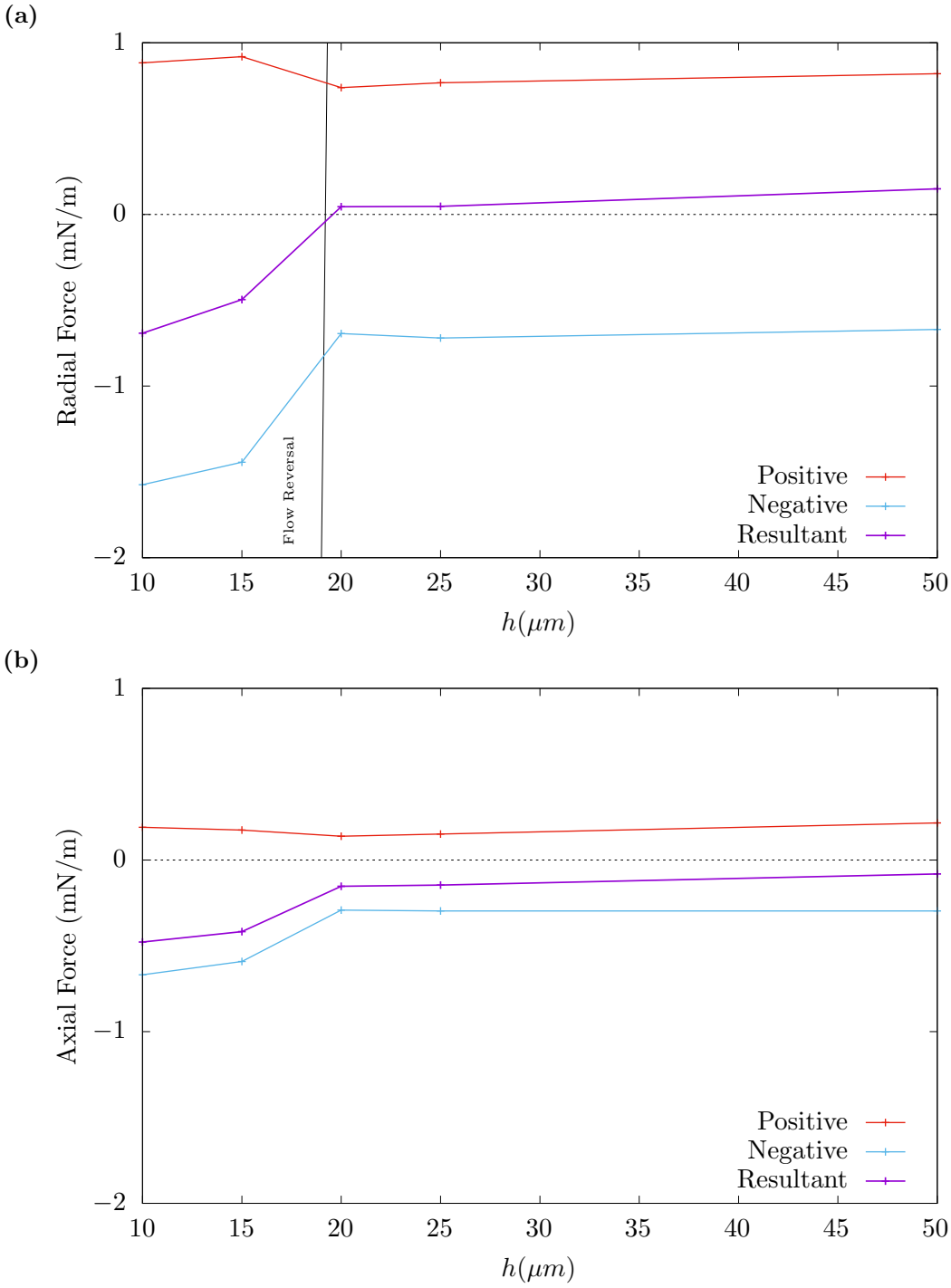

Figure 4.4: *Cycle-averaged and spatially-integrated (a) radial and (b) axial forcing components with $D = 1\ mm$, $O_2 = 20\%$ and various exposed electrode thicknesses. Each forcing is broken into a positive and a negative component.*

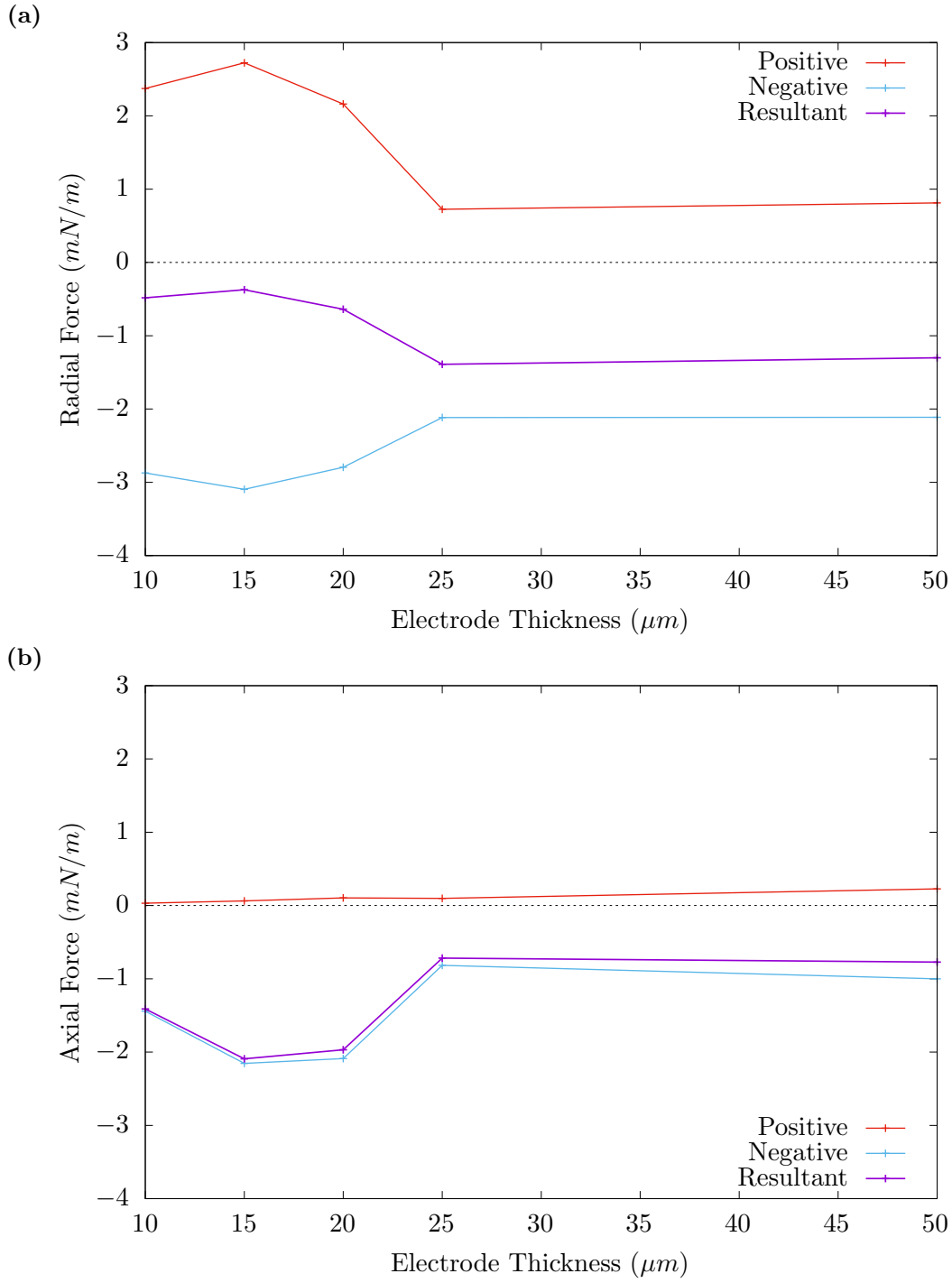

Figure 4.5: *Cycle-averaged and spatially-integrated (a) radial and (b) axial forcing components with $D = 2$ mm, $O_2 = 20\%$ and various exposed electrode thicknesses. Each forcing is broken into a positive and a negative component.*

(a) The Positive Discharge

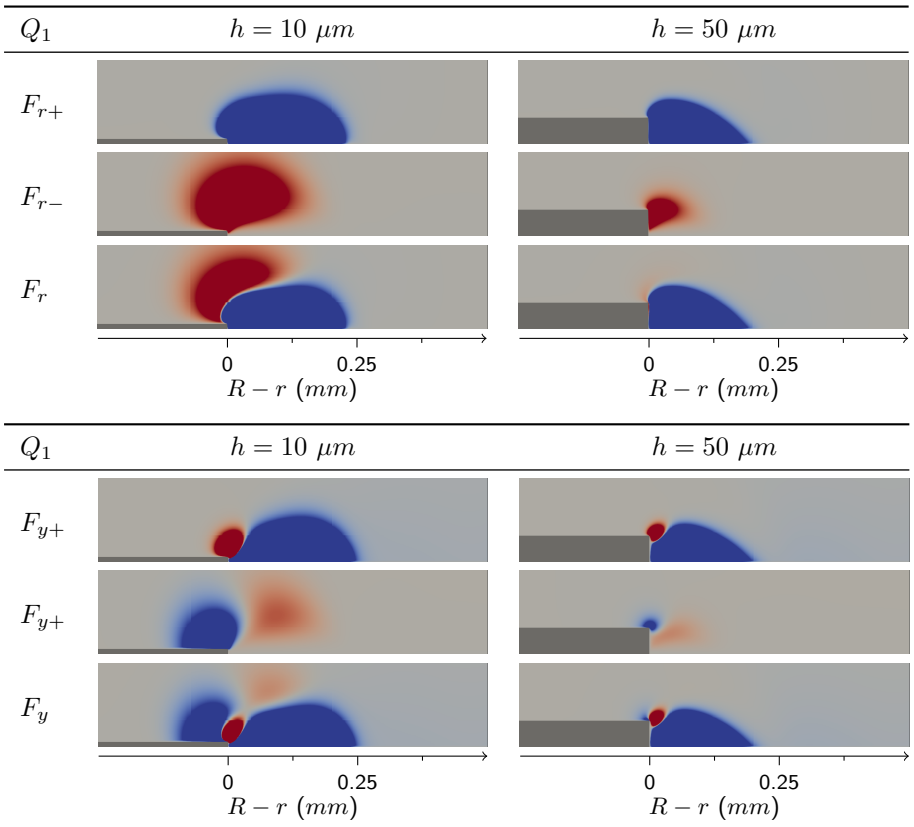

(b) The Negative Discharge

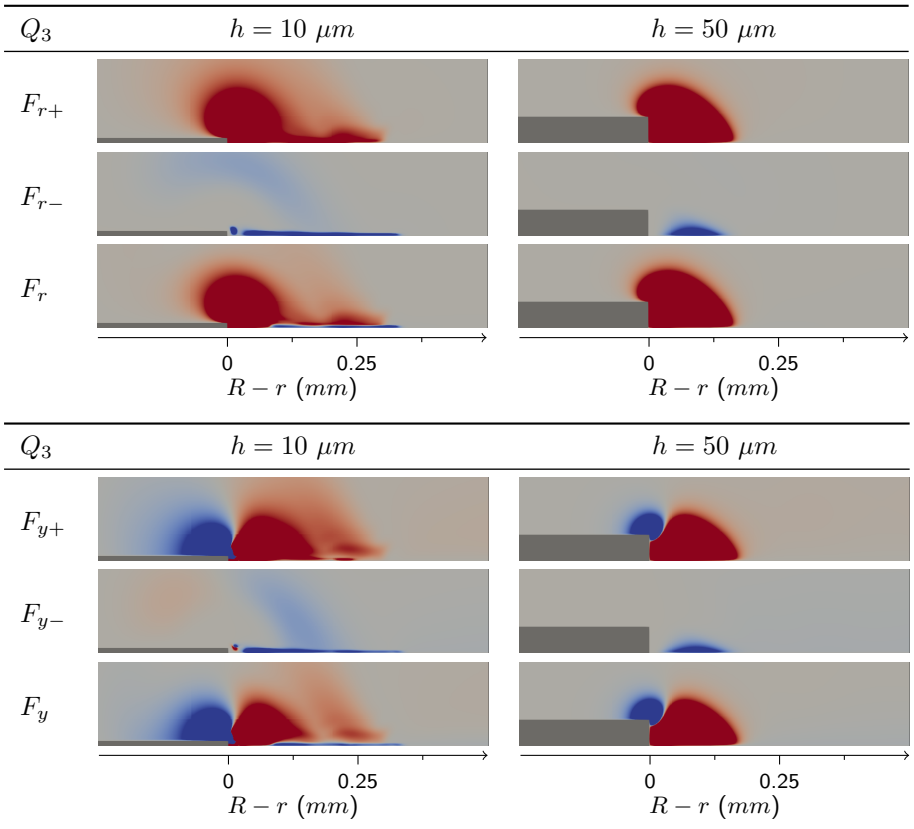

Figure 4.6: *The forcing contributions of the positive (F_+) and negative (F_-) ions to the total induced EHD force (F), averaged over (a) the positive discharge and (b) the negative discharge for both the $h = 10\ \mu m$, $D = 1\ mm$, $0_2 = 20\%$ and the $h = 50\ \mu m$, $D = 1\ mm$, $O_2 = 20\%$ cases.*

(a) The Positive Discharge

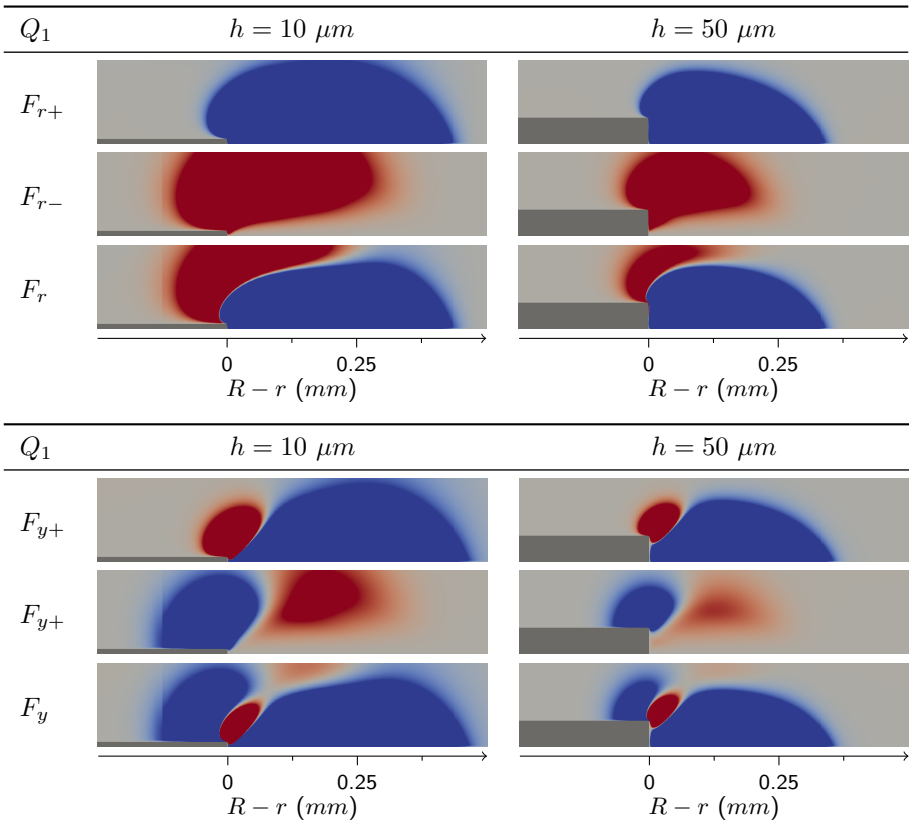

(b) The Negative Discharge

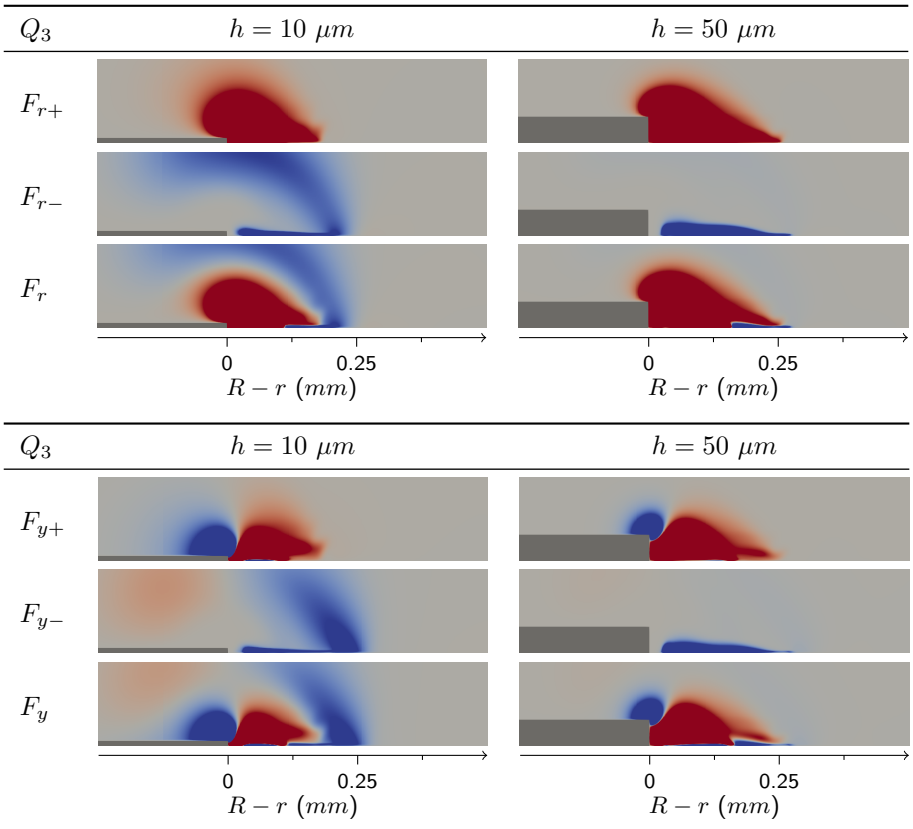

Figure 4.7: *The forcing contributions of the positive (F_+) and negative (F_-) ions to the total induced EHD force (F), averaged over (a) the positive discharge and (b) the negative discharge for both the $h = 10\ \mu m$, $D = 2\ mm$, $0_2 = 20\%$ and the $h = 50\ \mu m$, $D = 2\ mm$, $O_2 = 20\%$ cases.*

during the positive discharge

4.3 The Effect of Ambient Gas-Fraction on the Discharge Structure

The threshold for the reversal of axial flow direction is not only defined by the actuator geometry but is dependent on the gas-fraction at which the actuator is operated. In this section, the effect of the ambient gas-fraction on the DBD actuator performance is examined. With the operating gas assumed to be a pure mixture of N_2 and O_2, the concentration of electronegative oxygen will allow the role of negative ions to be investigated.

Figure 4.8 shows the velocity fields induced by actuators with $D = 1\ mm$ and $h = 50\ \mu m$ operating at different ambient gas-fractions. A transition from an outward to an inward regime can be observed. As the oxygen content increased to 50%, recirculation regions formed near the electrode edge, indicating that the threshold for the flow reversal is being approached. Finally, the full reversal of the axial jet occurred as the oxygen gas-fraction reached 60%, with vortices close to the surface and flow drawn largely vertically, similar to the entrainment behaviour of the low electrode thickness cases shown earlier in figure 4.1.

Figure 4.9 shows the resulting fluid flow when $D = 2\ mm$ and $h = 50\mu m$, as the ambient gas-fraction is varied. Initially, when the oxygen gas-fraction is increased, the outward jet becomes stronger and more concentrated. However, for cases with $O_2 \geq 60\%$ there is a sudden reversal of the axial flow direction. It seems contradictory that both a reversal from an inward to an outward jet, and a reversal from an outward to an inward jet, can be induced at the same oxygen gas-fraction for different actuator diameters. However, the resulting flow structure is not fully comparable to other inward cases, with multiple recirculation zones being observed, one near the exposed electrode edge and another near the centre axis.

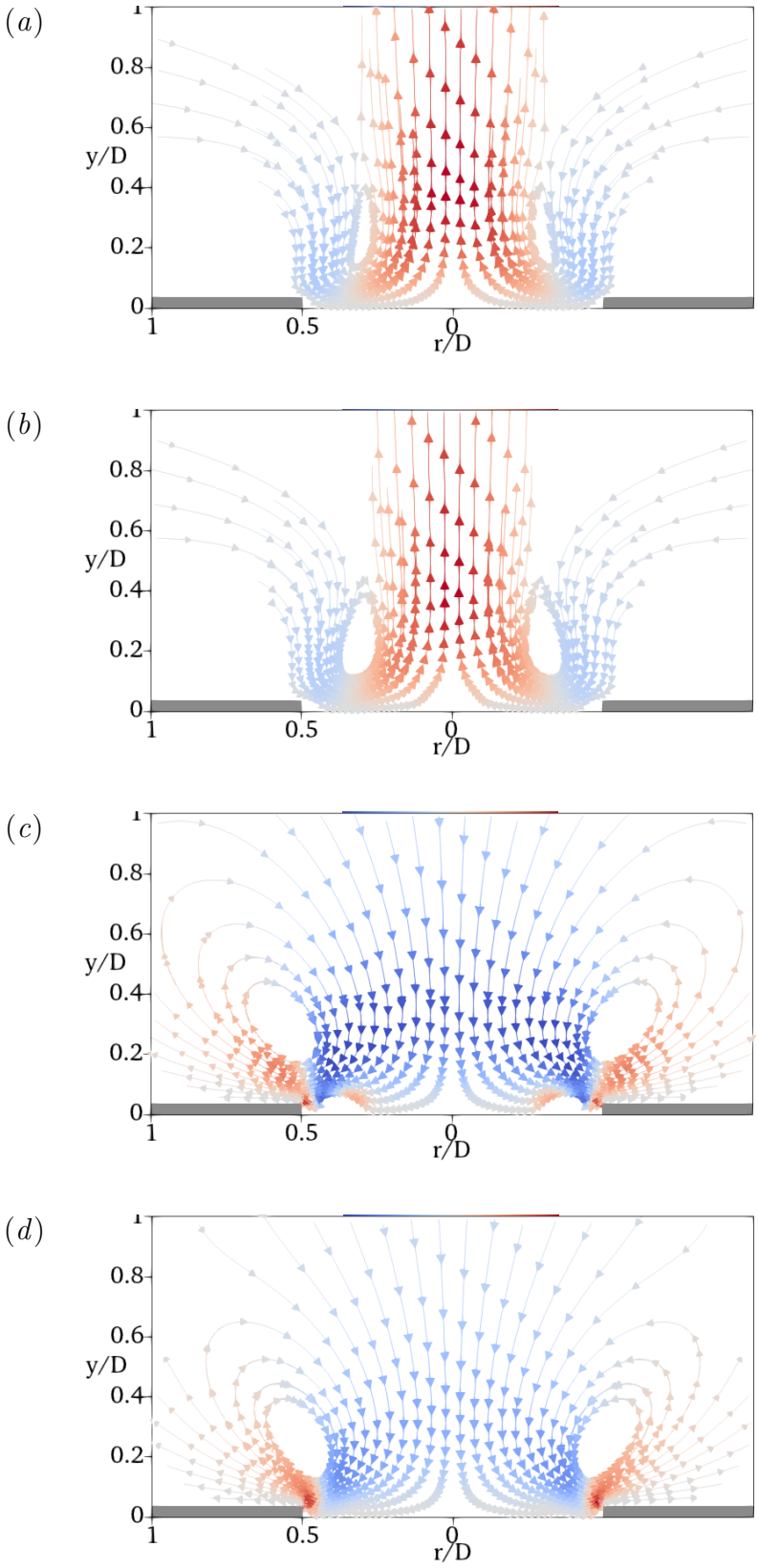

Figure 4.8: *The axisymmetric flow induced by annular DBD actuators with* $D = 1\ mm$ *and* $h = 50\ \mu m$*, operating at* $O_2 = 70\%$*,* 60%*,* 50% *and* 20% *for (a)−(d), respectively. The grey regions denote the exposed electrode positions. The velocity is normalized by its absolute maximum.*

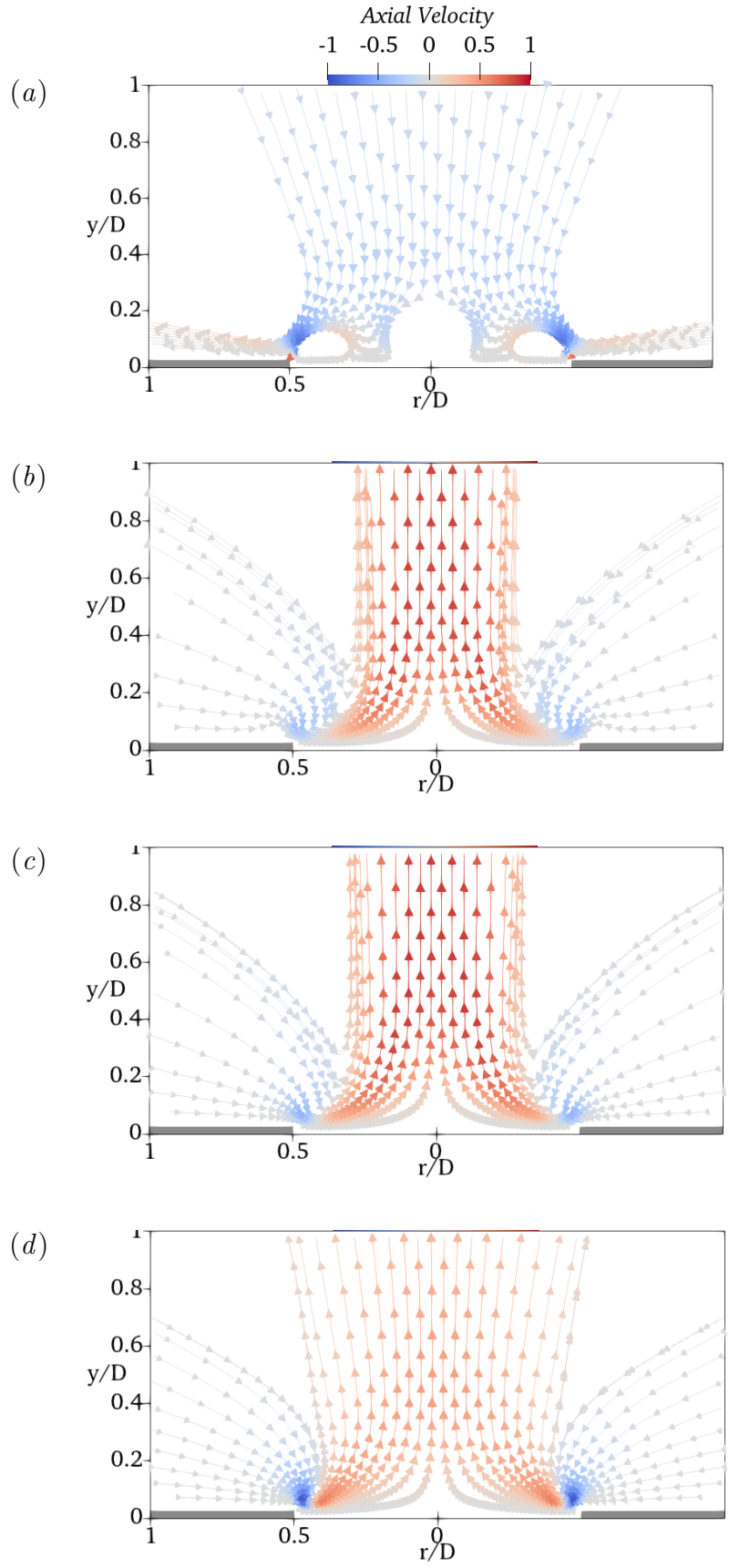

Figure 4.9: *The axisymmetric flow induced by annular DBD actuators with D = 2 mm and h = 50 μm, operating at O_2 = 70%, 60%, 50% and 20% for (a)−(d), respectively. The grey regions denote the exposed electrode positions. The velocity is normalized by its absolute maximum.*

Figure 4.10 shows the cycle-averaged EHD forcing distributions for the $D = 1\ mm$, $h = 50\mu m$ case operating at different ambient gas-fractions. Both the inward and outward forcing regions grow with increased oxygen content, and once a threshold of $O_2 \geq 50\%$ is reached, the volume of the outward forcing, dramatically and disproportionately increases. For comparison, figure 4.11 shows the cycle-averaged EHD forcing distribution for 2 mm diameter actuators operating at the same range of different ambient gas-fractions. In this case, both the outward and inward forcing regions increase in volume and intensity as before. However, after the threshold of $O_2 = 60\%$ is reached, the volume of the outward forcing region suddenly decreases, whilst the inward forcing region even more dramatically increases. There is also evidence of a new streamer-like structure close to the dielectric surface, beyond which there is a secondary smaller outward forcing volume. It is this unusual distribution which accounts for the flow field observed in figure 4.9(a).

These distributions are spatially integrated and shown in figures 4.12 and 4.13 for the $D = 1\ mm$ and $D = 2mm$ cases, respectively. Figure 4.12, the $D = 1\ mm$ case, shows a gradual increase in both the outward and inward forcing. However, as the increase in the negative forcing component is greater, the resultant forcing decreases. Once a threshold of $O_2 \geq 60\%$ is reached there is a significant increase in the negative radial component, leading to a negative radial resultant force and the reversal of the axial flow direction.

Below the threshold of $O_2 = 60\%$, the behaviour of the $D = 2\ mm$ case with increasing $O_2\%$ is similar, with an increasing negative radial component leading to an stronger negative resultant force. However, once $O_2 \geq 60\%$ is reached there is a simultaneous collapse of the negative forcing, and a dramatic increase in the the positive forcing component. This leads to the resultant radial forcing transitioning from strongly negative to strongly positive, corresponding to the reversal of axial flow observed in figure 4.9. The strong difference in the behaviour between the $D = 1\ mm$ and $D = 2\ mm$ cases, with a reversal from an inward to an outward jet for the $D = 1\ mm$ being observed at the same

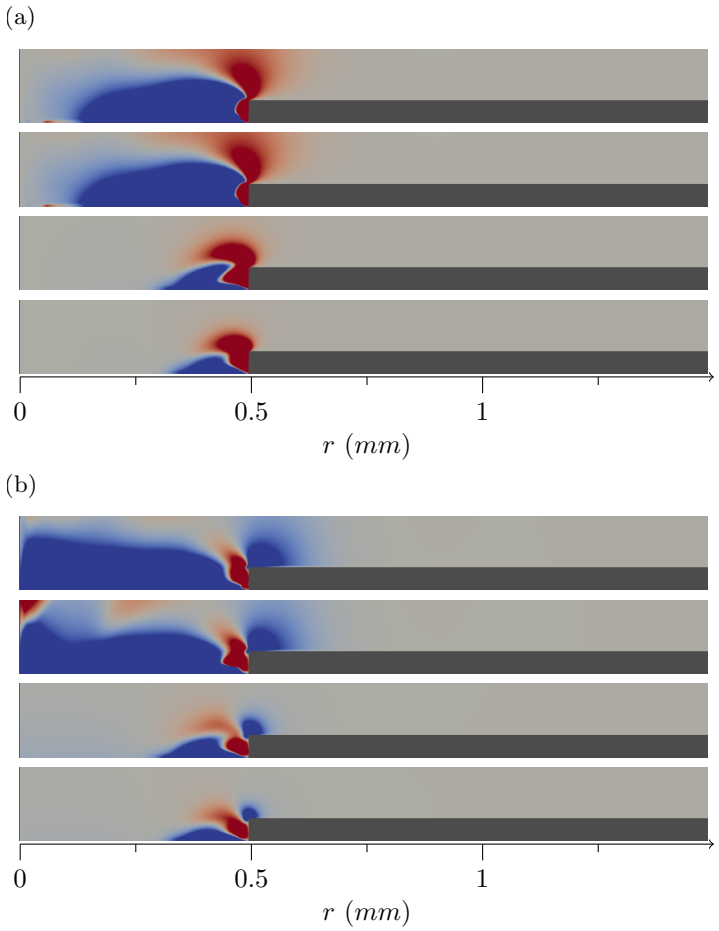

Figure 4.10: *Cycle-averaged distributions of (a) radial EHD forcing component* $\overline{F_r}$ *and (b) axial EHD forcing component* $\overline{F_y}$ *with* $D = 1\ mm$ *and* $h = 50\ \mu m$*. The oxygen gas-fraction is* $O_2 = 70\%$*,* 60%*,* 50%*, and* 20% *from top to bottom. Red:* $\geq 10\ kNmm^{-3}$*, Blue:* $\leq -10\ kNmm^{-3}$*.*

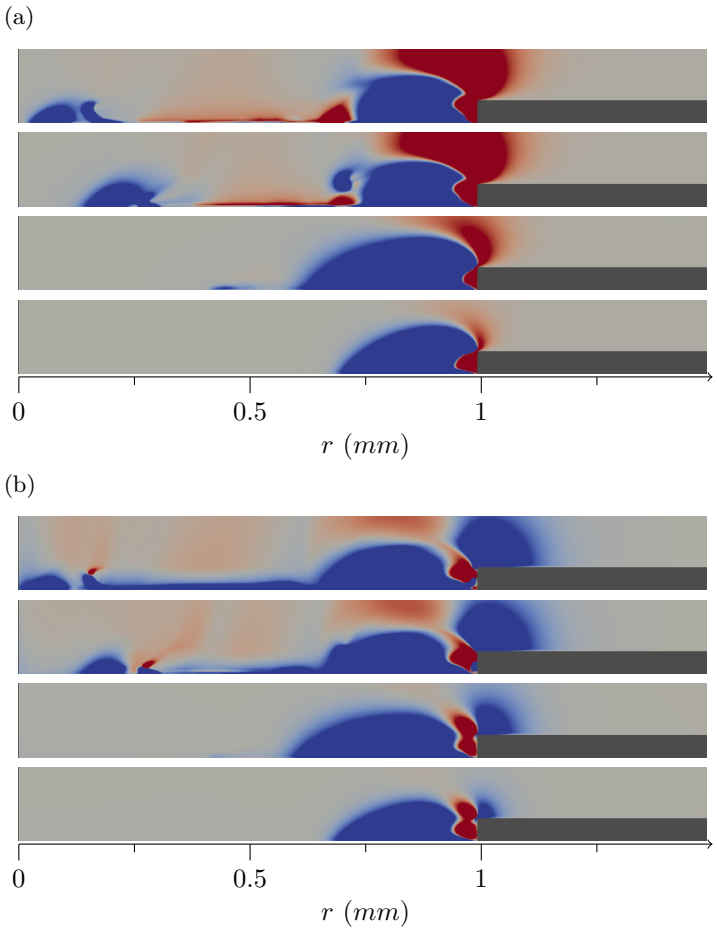

Figure 4.11: *Cycle-averaged distributions of (a) radial EHD forcing component* $\overline{F_r}$ *and (b) axial EHD forcing component* $\overline{F_y}$ *with* $D = 2$ *mm and* $h = 50$ μm*. The oxygen gas-fraction is* $O_2 = 70\%$*,* 60%*,* 50%*, and* 20% *from top to bottom. Red:* ≥ 10 $kNmm^{-3}$*, Blue:* ≤ -10 $kNmm^{-3}$*.*

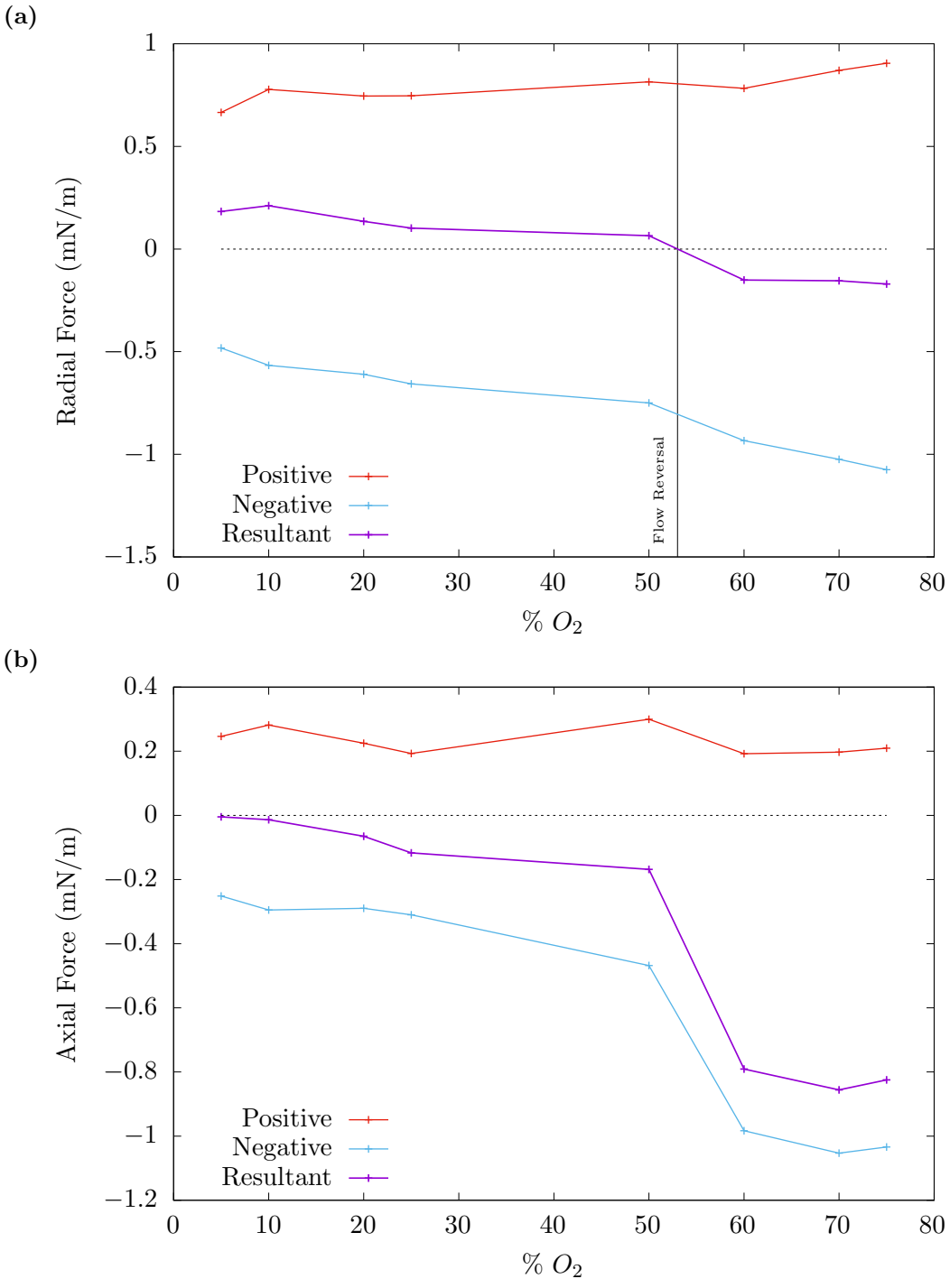

Figure 4.12: *Cycle-averaged and spatially-integrated (a) radial and (b) axial forcing components with $D = 1$ mm, $h = 50$ μm operating at various oxygen gas-fractions. Each forcing is broken into a positive and a negative component.*

oxygen gas-fraction, as the reversal of an outward jet to an inward jet for a $D = 2\ mm$ is emphasised.

To examine the mechanisms behind this behaviour, the cycle averaged forcing distributions are decomposed into the contributions of the positive and negative ions during each discharge sub-cycle, as above. Figure 4.14, compares these contributions for a $D = 1mm$, $h = 50\ \mu m$ actuator operating at both $O_2 = 20\%$ and $O_2 = 70\%$ and thus generating two different axial flow directions. We observe that the bulk of the increase in forcing volume is generated during the positive discharge, and although significant increases in both the positive and negative ion volumes are observed, the contribution from the negative ions increases proportionately more. Meanwhile, there is a limited increase in the forcing volume observed during the negative discharge. A large volume of weak residual charge from the previous positive discharge can also be observed.

Figure 4.15 shows the same forcing decompositions for a 2 mm diameter actuator. Here the axial flow direction transitions from outward to inward as the oxygen gas-fraction increases. During the positive discharge of the $O_2 = 60\%$ case both the positive and negative ions have both positive and negative radial forcing components. This indicates a more energetic discharge with the local charge density modifying the global electric field.

Unlike the previous case, the largest increase in plasma volumes are during the negative discharge, with the contributions of both ions increasing dramatically. As before, there is also a disproportionate growth in the negative ion volumes during both half-cycles.

The reason for this dramatic change in the discharge structure is the formation of positive streamers during the positive discharge cycle. Figure 4.16 shows how the spatially-integrated radial forcing varies across the AC cycle for both the $0_2 = 50\%$ and the $O_2 = 60\%$ cases. The formation of a new intense radial forcing peak during the positive discharge can be seen for the $O_2 = 60\%$ case. After this intense peak there is a reduction in the radial forcing during this

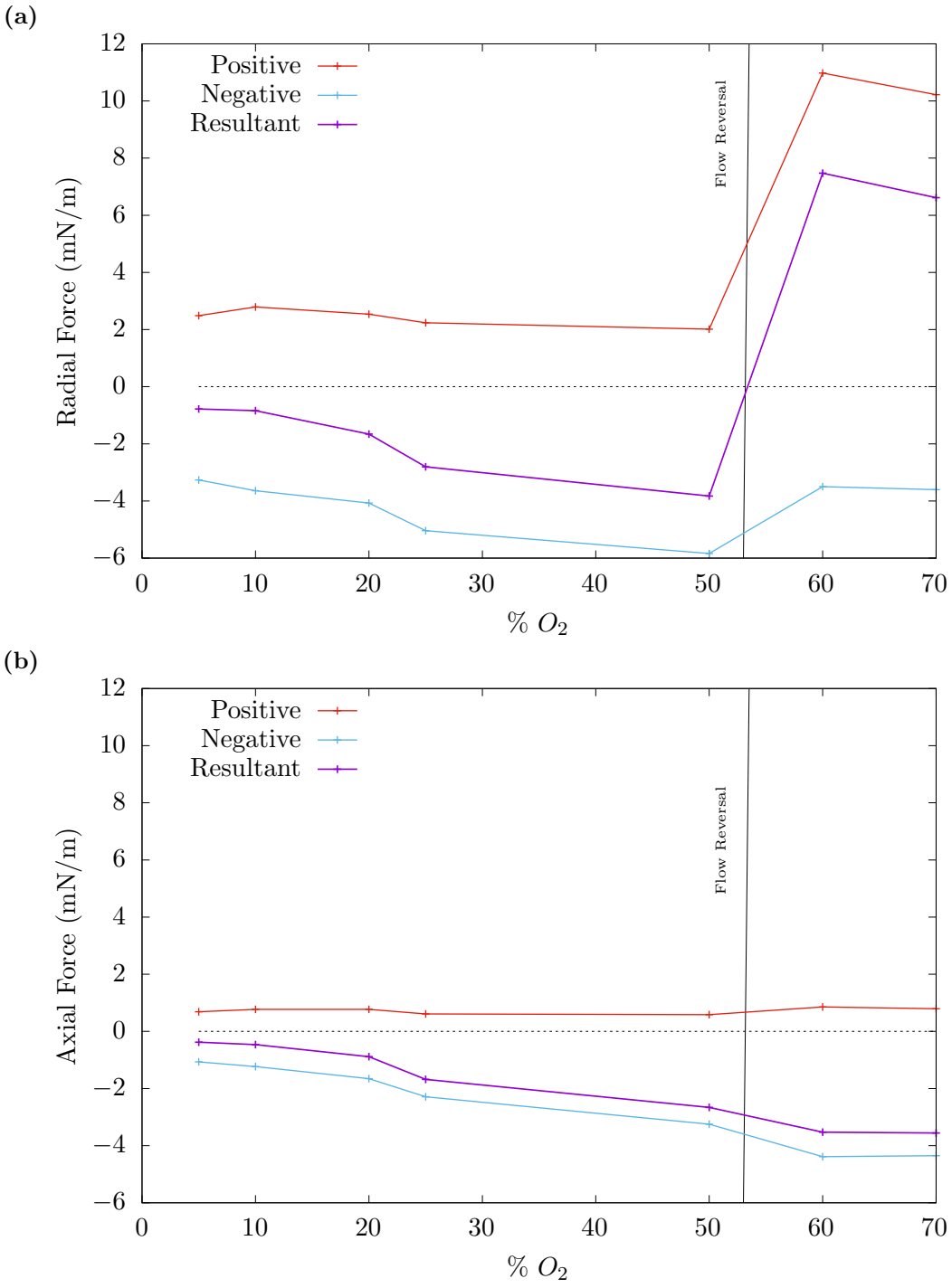

Figure 4.13: *Cycle-averaged and spatially-integrated (a) radial and (b) axial forcing components with $D = 2$ mm, $h = 50$ μm operating at various oxygen gas-fractions. Each forcing is broken into a positive and a negative component.*

(a) The Positive Discharge

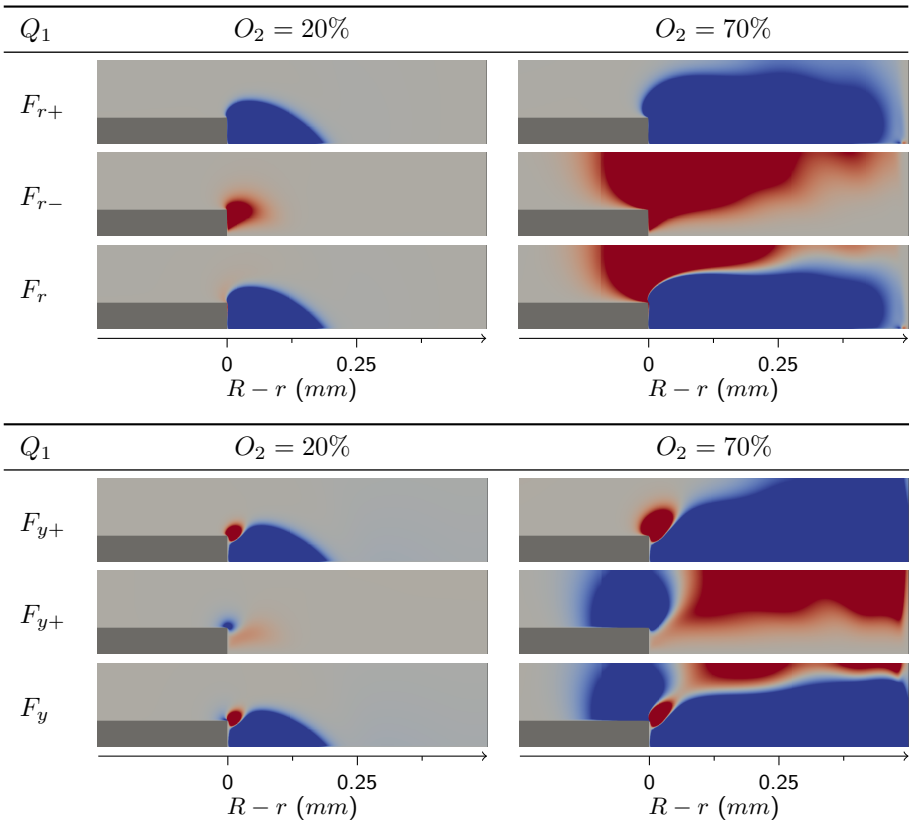

(b) The Negative Discharge

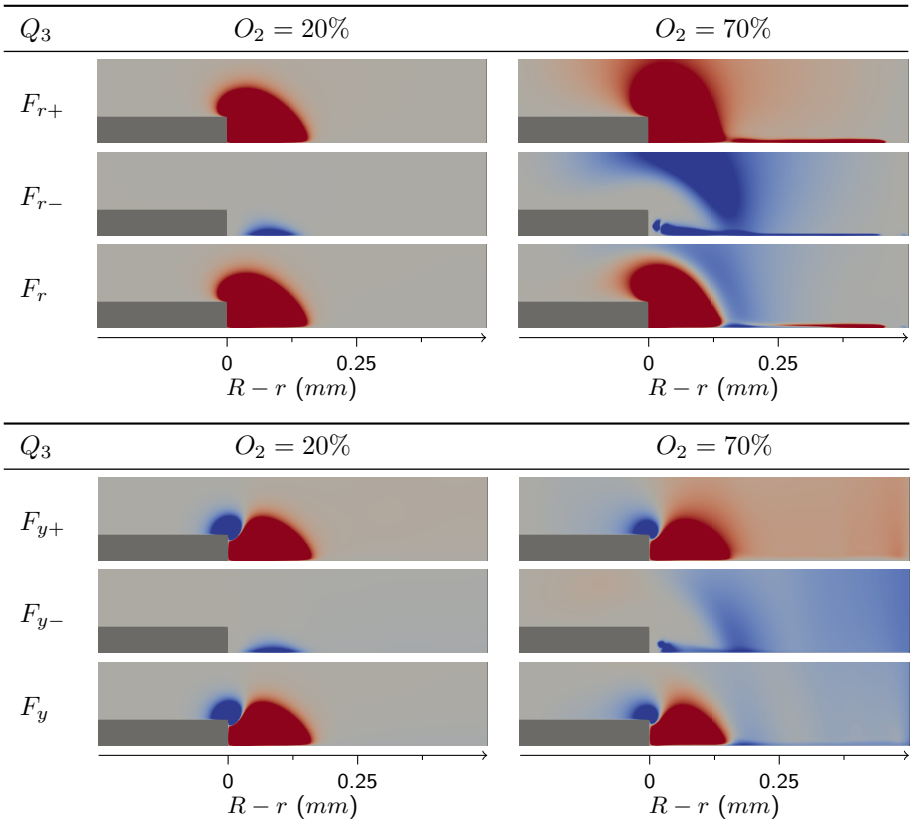

Figure 4.14: *The forcing contributions of the positive (F_+) and negative (F_-) ions to the total induced EHD force (F), averaged over (a) the positive discharge and (b) the negative discharge for both the $h = 50$ μm, $D = 1$ mm, $0_2 = 20\%$ and the $h = 50$ μm, $D = 1$ mm, $O_2 = 70\%$ cases.*

(a) The Positive Discharge

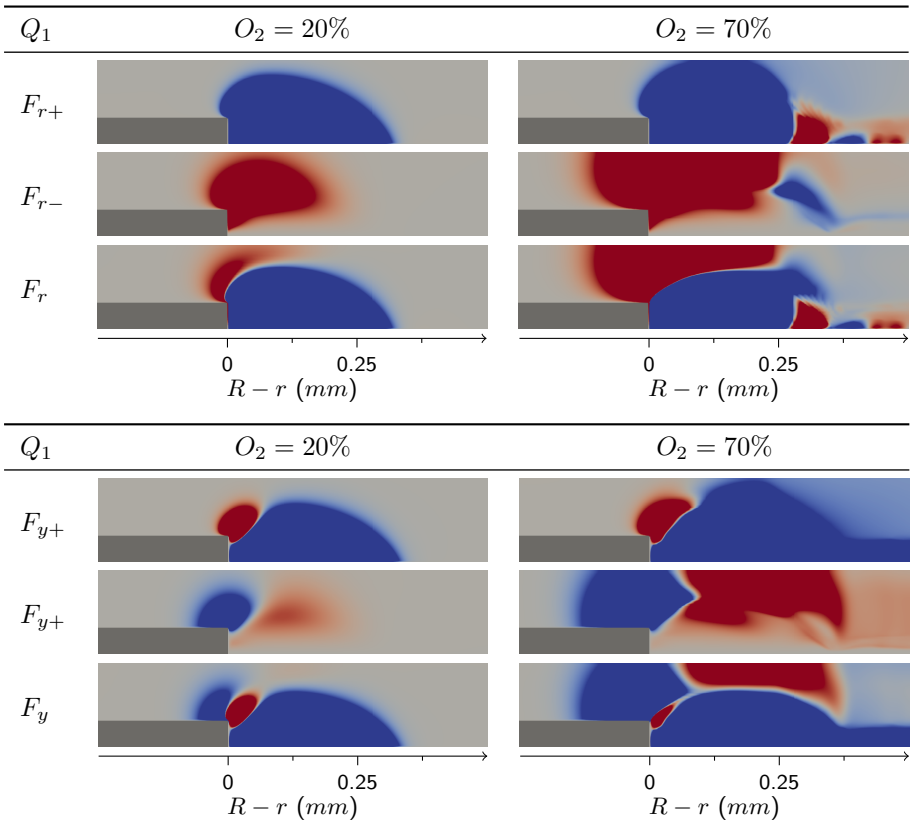

(b) The Negative Discharge

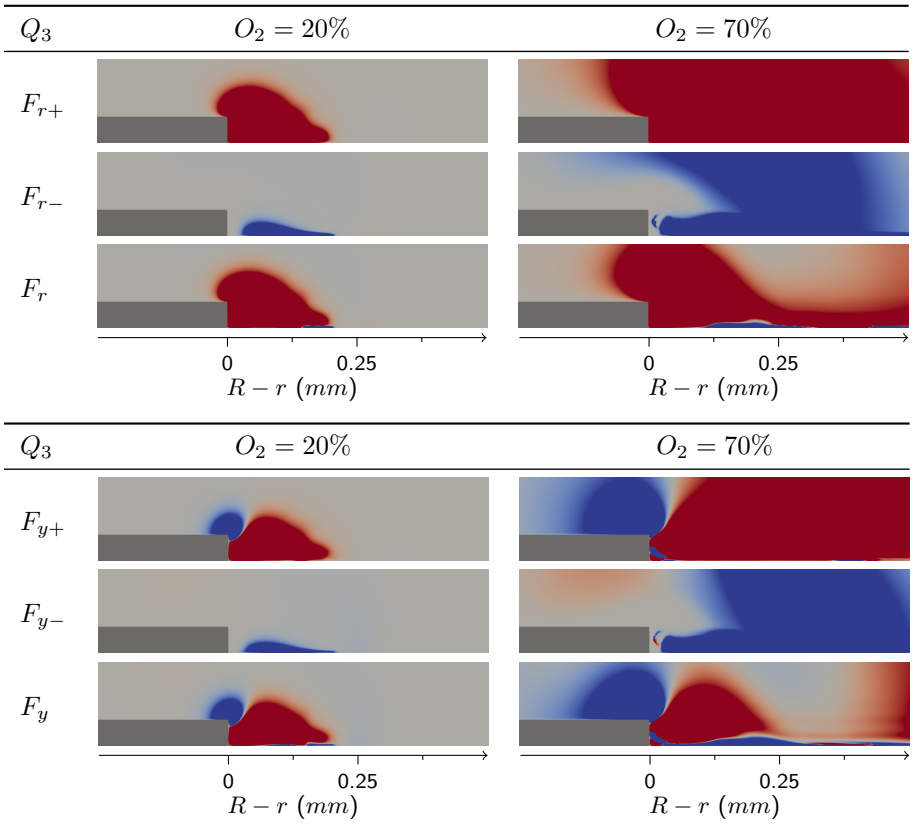

Figure 4.15: *The forcing contributions of the positive (F_+) and negative (F_-) ions to the total induced EHD force (F), averaged over (a) the positive discharge and (b) the negative discharge for both the $h = 50$ μm, $D = 2$ mm, $0_2 = 20\%$ and the $h = 50$ μm, $D = 2$ mm, $O_2 = 70\%$ cases.*

sub-cycle. There is also an increase in the EHD forcing generated during the negative discharge, with more diffuse peaks and an elevated positive radial forcing encouraging an inward jet.

It is proposed that the formation of the positive streamer is caused by the lower ionisation coefficient of oxygen leading to a stronger local ion production rate as the concentration of oxygen is increased. This increased space charge leads to the production of a strong local electric field and further induced ionisation. This leads to the formation of streamers as described in Chapter 1. These constricted high-current streamers rapidly charge the dielectric, quenching the discharge and reducing the forcing volume during the positive discharge. Conversely, the intense charging of the dielectric inhibits quenching and encourages a stronger discharge during the subsequent negative cycle. Thus the formation of positive streamers during the positive half-cycle leads to a reduction in forcing during the positive half-cycle but an increase in forcing produced during the negative half-cycle. This leads to the domination of the inward forcing and the reversal of the axial jet. That positive streamers encourage an inward flow explains why the reversal from an outward jet to an inward jet occurs at larger diameters for annular actuators operating in the streamer regime [38, 140].

It is important to note that the streamer regime is not uniform in the azimuthal direction. Therefore, using a $2D$ axisymmetric model, which assumes no azimuthal variation is therefore not strictly valid for the streamer regime. However, previous works have shown that a 2D axisymmetric geometry gives a good approximation of the spanwise-averaged distribution [122]. Additionally, the transient and intense nature of streamers, mean that they are not perfectly periodic. The strong localised forcing evident in figure 4.11, would likely be reduced into a more representative forcing distribution if the forcing was averaged over many cycles. However this is left to future work due to the high computational cost required.

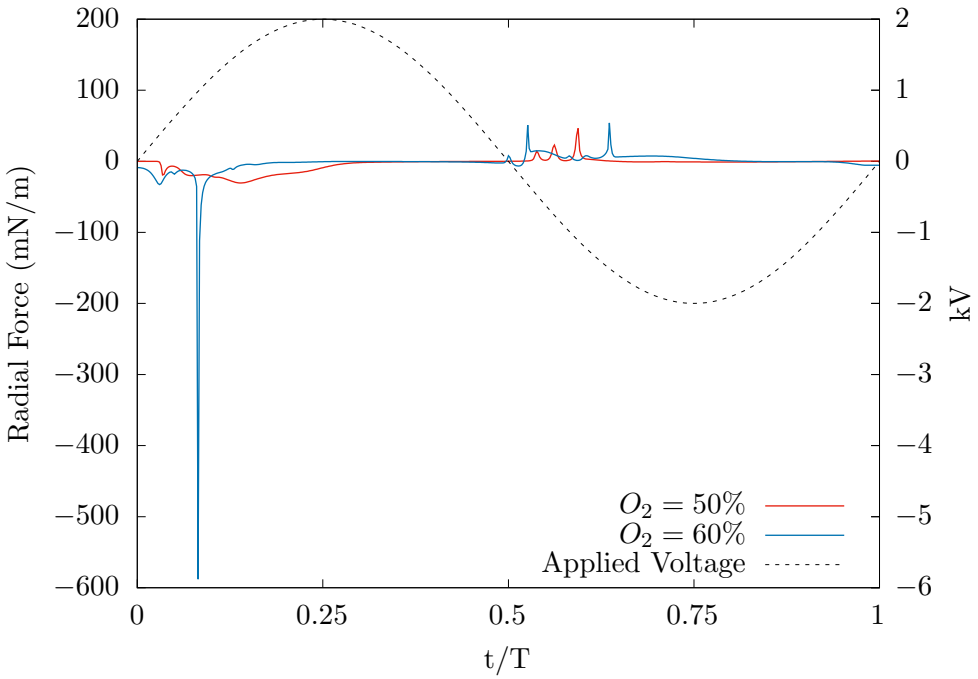

Figure 4.16: *Radial EHD forcing per unit circumference over a single AC cycle for the $h = 50$ μm, $D = 2$ mm, $0_2 = 50\%$ and $h = 50$ μm, $D = 2$ mm, $0_2 = 60\%$ cases, with excitation voltage represented by the dashed line.*

4.4 Summary of Effects on Actuator Performance

In this section, the effects that the actuator diameter D, the electrode thickness h and the oxygen gas-fraction O_2 have on actuator performance are summarised. To characterise an actuator's performance, first the key performance parameters must be identified. The performance of a DBD plasma actuator is dependent on the discharge asymmetry between positive and negative subcycles, as well as the discharge intensity. The EHD forcing can be directly linked to the current density as

$$\boldsymbol{F} = \sum_i \boldsymbol{J_i}/\mu_i \tag{4.1}$$

where i indicates the charged species, whilst $\boldsymbol{J_i}$ and μ_i are the species' current density and mobility, respectively. In order to give an independent measure of the discharge intensity which is not affected by changes to the discharge

asymmetry, it is useful to define the absolute radial force

$$\overline{F_{abs}} = \overline{F_+} + |\overline{F_-}| \tag{4.2}$$

where $\overline{F_+}$ and $\overline{F_-}$ are the time-averaged radial forcing in the positive and negative sub-cycles, respectively. This allows for the definition of the absolute forcing efficiency as

$$\eta = \overline{F_{abs}}/P \tag{4.3}$$

and the forcing effectiveness as

$$\epsilon = \overline{F_r}/\overline{F_{abs}} \tag{4.4}$$

where P and $\overline{F_r}$ are the power consumption and resultant radial forcing, respectively.

This section examines how the absolute and resultant radial forcing, as well as the associated absolute forcing efficiency and effectiveness of the two base cases ($D = 1\ mm$, $h = 50\ \mu m$, $O_2 = 20\%$ and $D = 2\ mm$, $h = 50\ \mu m$, $O_2 = 20\%$) change with the independent variation of D, h and O_2.

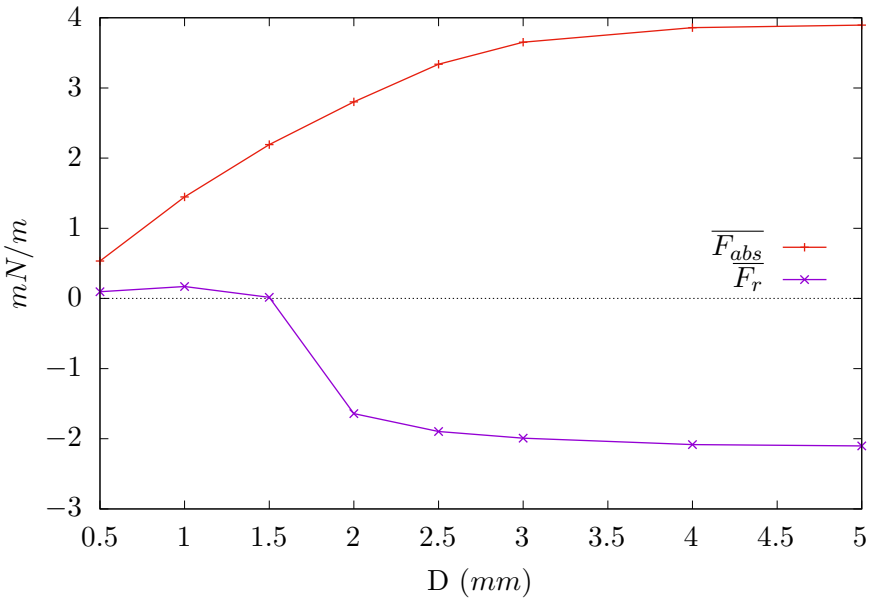

Figure 4.17: *The absolute and resultant radial force for $h = 50\mu m$ and $O_2 = 20\%$ for different actuator diameters.*

Figure 4.17 examines how the absolute and resultant radial forcing varies with diameter. As the actuator diameter increases, the absolute forcing increases up to a maximum of $\approx 3.9\ mN/m$, plateauing at $D = 3\ mm$. As described in §3.4, the increase in diameter leads to a smaller proportion of the current being directed towards the surface. This leads to an increased discharge intensity in both sub-cycles and thus an increase in the absolute radial force. Whilst the absolute forcing is related to the discharge intensity, it is the resultant forcing which determines the direction and strength of the axial jet as shown in §3.3. As well as the discharge intensity, the resultant radial forcing is a function of the asymmetry between the positive and negative discharges. For small diameter actuators, the resultant radial forcing is small, positive, and approximately constant. As the actuator diameter increases to $D = 2\ mm$, there is a sudden decrease in the resultant radial forcing caused by the increasing intensity of the negative-cycle microdischarges, motivating an increased forcing volume during the positive discharge, as described in §3.4.

Figure 4.18 examines the variation of the absolute and resultant radial forcing with exposed electrode thickness for both a 1 mm and a 2 mm diameter actuators. As the exposed electrode thickness is reduced, the absolute radial forcing remains approximately constant for both diameters, until a threshold is reached. For the 1 mm case this threshold is 20 μm, after which there is a sudden increase in the absolute radial forcing. This is due to an increased contribution of both the positive and negative ions during the positive discharge. However, the greater increase in positive ions leads to more negative radial forcing being generated during the positive discharge. This causes the resultant radial forcing to decrease and become negative leading to the reversal of the axial jet from inward to outward. For the 2 mm case, the threshold is 25 μm, after which there is a strong increase in the absolute forcing. Whilst the contribution of both the positive and negative ions increased, the negative ions increased the most, leading to a reduction in the magnitude of the resultant forcing. It should also be noted that the absolute forcing decreases as h

is reduced from 15 μm to 10 μm.

Figure 4.19 examines variation of the absolute and resultant radial forcing with the oxygen gas-fraction for the $D = 1\ mm$ and the $D = 2\ mm$ cases. As the oxygen content increases, F_{abs} increases for both diameter actuators, whilst the resultant force decreases. However, for the $D = 1\ mm$ case, when the oxygen gas-fraction reaches 60% the resultant forcing becomes negative for the first time, leading to a reversal from an inward to an outward axial jet. For the $D = 2\ mm$ case the formation of positive streamers at $O_2 = 60\%$ leads to a dramatic increase in the positive radial forcing. This causes a dramatic positive increase of both the absolute and resultant forcing, and a reversal of the axial flow from outward to inward.

Figure 4.20 examines the absolute forcing efficiency η and effectiveness ϵ for different diameter actuators. The absolute forcing efficiency η measures how efficiently the input power is converted into discharge intensity. It increases with actuator diameter up to a value of 8 $\mu N/W$ at $D = 4\ mm$. An actuator's effectiveness ϵ is a function of discharge asymmetry, with a more asymmetrical, less antagonistic discharge leading to an increased effectiveness, whilst the effectiveness will be zero at the point of axial flow reversal, as no resultant radial force is generated. Smaller diameter actuators generating inward flows, have a more antagonistic discharge cycle with a reduced plasma volume, leading to a lower effectiveness and lower efficiency. The presence of intense negative-cycle microdischarges significantly increase the effectiveness for actuators with large diameters generating an outward jet, by encouraging discharge asymmetry.

Figure 4.21 illustrates the variation in efficiency and effectiveness with exposed electrode thickness for both a 1 mm and a 2 mm diameter actuator. For the 1 mm diameter actuator the efficiency is largely constant until at low h the increasingly intense microdischarges lead to a reduced efficiency. However, as these microdischarges increase the discharge asymmetry, this also leads to an increased effectiveness. For the 2 mm diameter actuator there is a gradual decrease in efficiency as h is reduced. However, the increasing proportion

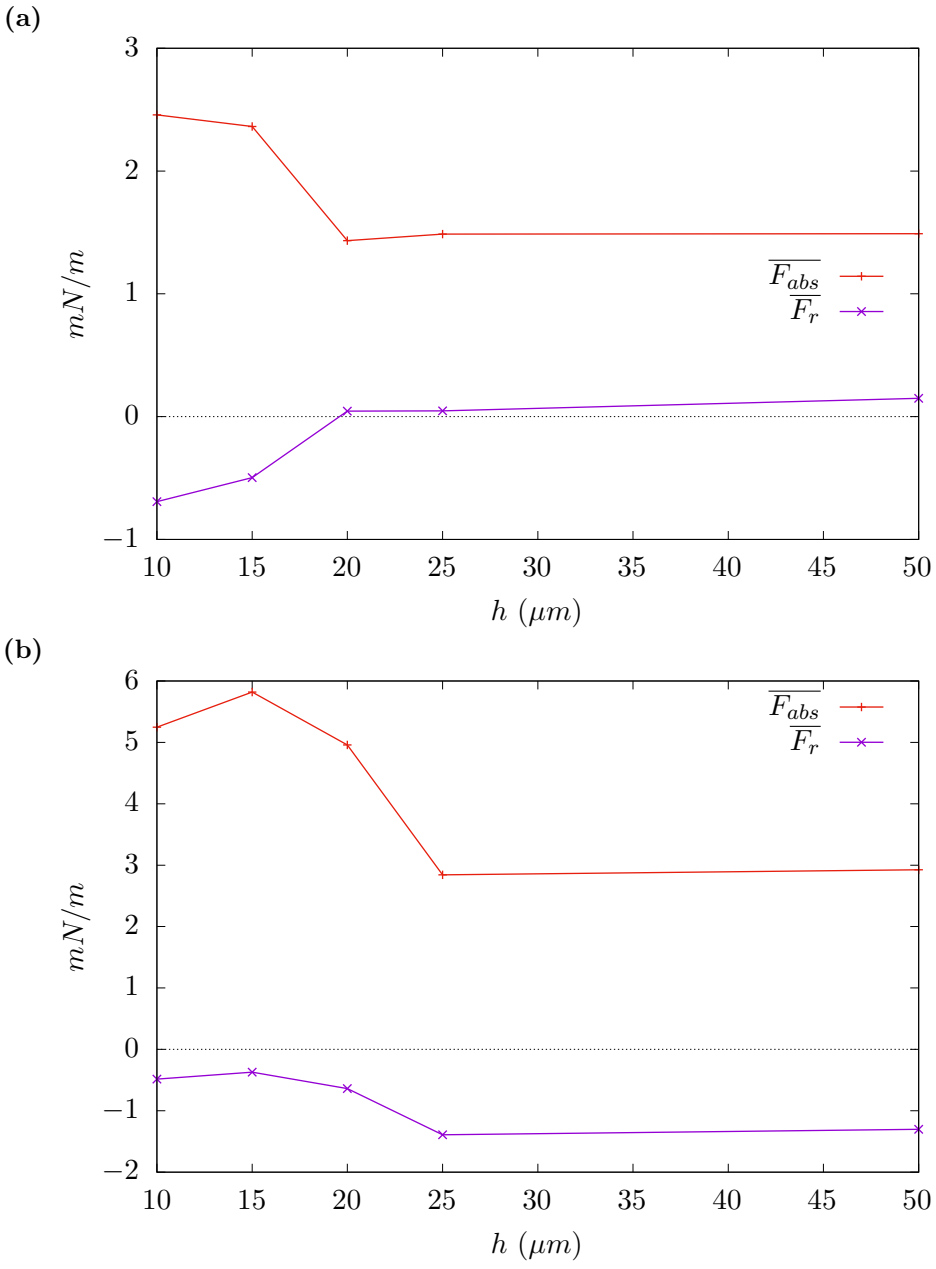

Figure 4.18: *The absolute and resultant radial force for (a) $D = 1$ mm, $O_2 = 20\%$ and (b) $D = 2$ mm, $O_2 = 20\%$ cases for different exposed electrode thicknesses.*

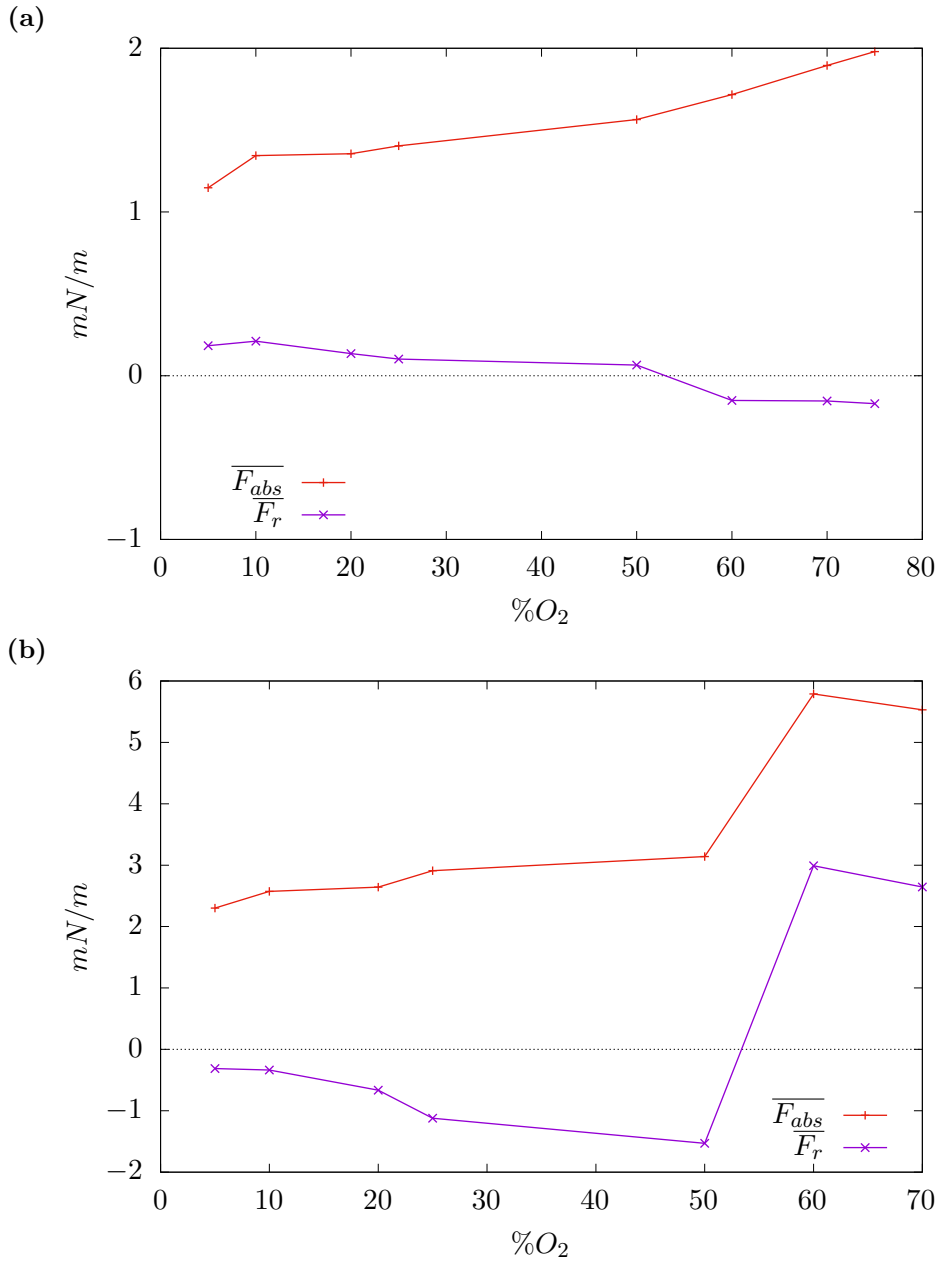

Figure 4.19: *The absolute and resultant radial force for (a) $D = 1$ mm, $h = 50$ μm and (b) $D = 2$ mm, $h = 50$ μm cases operating at different oxygen gas-fractions.*

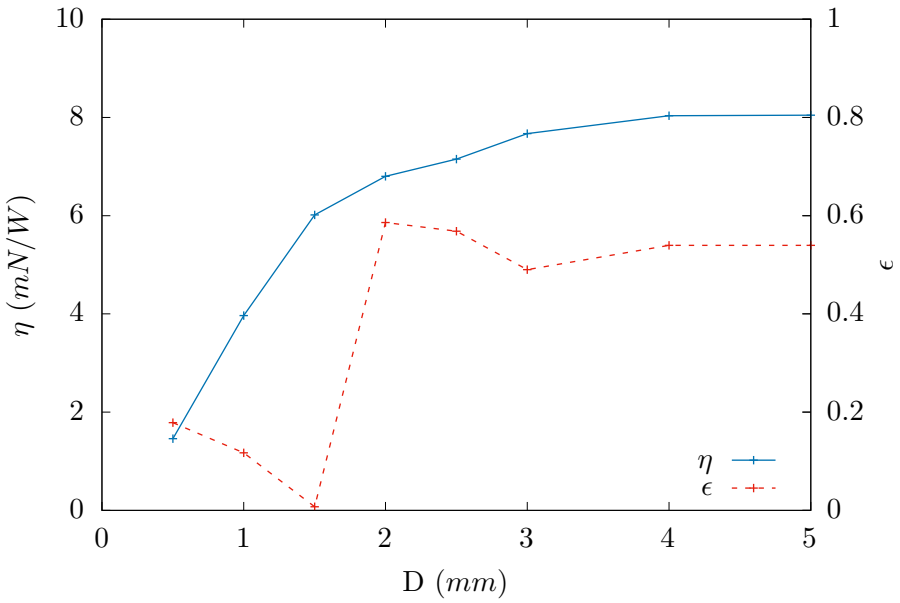

Figure 4.20: *The efficiency η and effectiveness ϵ for $h = 50\mu m$ and $O_2 = 20\%$ for different actuator diameters.*

of antagonistic negative ions leads to a reduction in the resultant force, and therefore the effectiveness necessarily decreases at low h.

Figure 4.22 examines the variations in the efficiency and effectiveness of the 1 mm and 2 mm diameter actuators as the oxygen gas-fraction is varied. For both cases, there is a gradual increase in the effectiveness as the oxygen content increases. For the 1 mm case, the effectiveness of the outward jet is not significantly larger than that of the inward jet. It is proposed that this is due to the increased proportion of antagonistic negative ions.

The efficiency initially increases with oxygen content, for both cases. However, with the formation of the positive streamers the efficiency dramatically reduces at the higher O_2 contents for the 2 mm.

4.5 Concluding Remarks

This parameter study would therefore suggest that the millimetric annular DBD plasma actuator performance, control effect, efficiency and effectiveness are improved for outward jets indicating that they would be better suited for flow control applications. An outward jet can be induced for small diameter

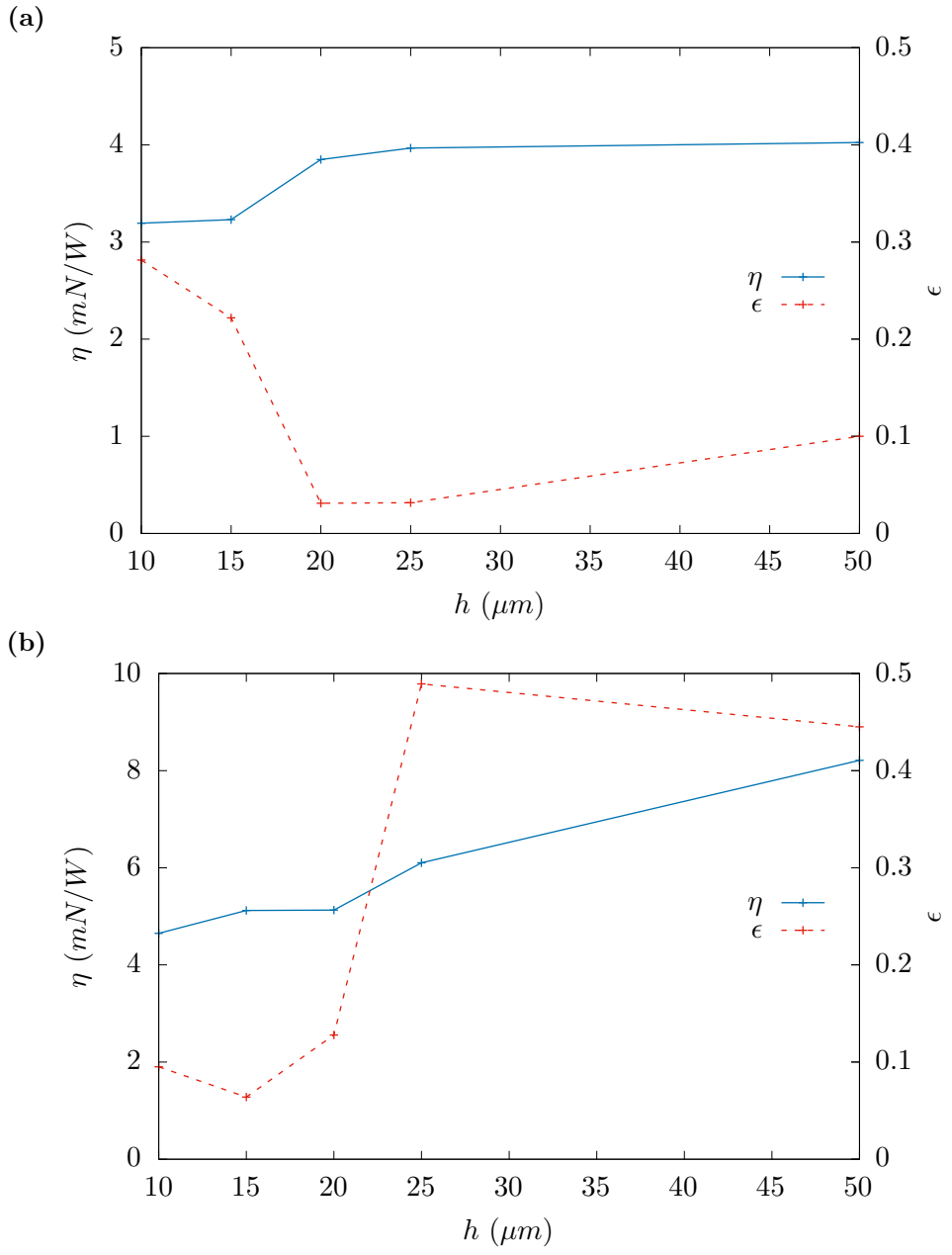

Figure 4.21: *The efficiency η and effectiveness ϵ (a) $D = 1$ mm, $O_2 = 20\%$ and (b) $D = 2$ mm, $O_2 = 20\%$ cases for different exposed electrode thicknesses.*

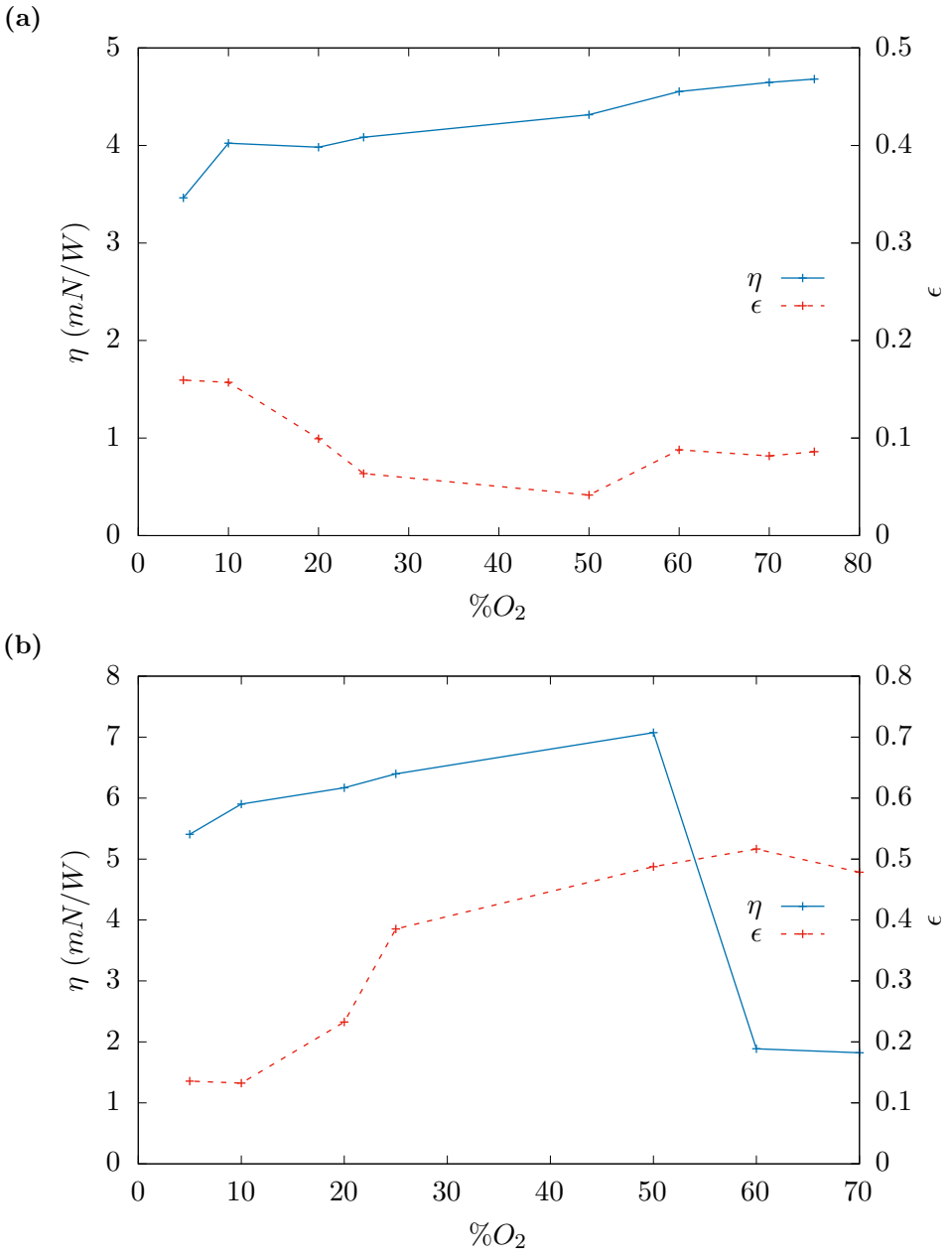

Figure 4.22: *The efficiency η and effectiveness ϵ for (a) $D = 1$ mm, $h = 50$ μm and (b) $D = 2$ mm, $h = 50$ μm cases operating at different oxygen gas-fractions.*

actuators, by reducing electrode thickness, or increasing oxygen gas-fraction. However, inward jets can be induced for larger actuators by increasing the oxygen content to such a degree that positive streamers are formed.

Chapter 5

Inducing Boundary Layer Structures with DBD Plasma Actuators

5.1 Introduction

Controlling the transition of a laminar boundary layer to a turbulent one, is one of the most studied areas of fluid mechanics. Delaying transition reduces skin friction and allows for significant global savings across a range of sectors. It is estimated that a 1% reduction in skin friction could save the transport industry £13B and 9 million tons of CO_2 per year [148]. Inducing turbulence can prevent boundary layer separation and the production of form drag, allowing for less conservative aerodynamic designs with higher lift coefficients. Currently, only passive suppression techniques e.g.surface smoothing and riblets are implemented in real-world applications [149]. Such passive flow control systems cannot generate a time-varying control, limiting their versatility, and maximal performance. However, the active suppression of laminar-turbulent transition has long been a frontier of flow control research, and questions remain about it's feasibility [97].

Typically, boundary layer transition of a flat plate is the result of structures

in the boundary layer, called streaks, becoming unstable and breaking down and leading to a fully turbulent boundary layer. This process is described in Chapter 1. It has been shown in experiments that suppression of these streaks, preventing them from breaking down, can significantly delay transition [92, 96, 97].

The superposition of induced streamwise counter-rotating vortices, allows for the suppression of streaks with a high efficiency as it limits unnecessary flow actuation. To implement such a control, the induced vortices need to be the same scale as the streaks found in real-world applications. Whilst both the inward and outward configurations of linear synthetic jet actuators have been used in a variety of situations in literature, there has been limited research to investigate there performance on the sub-millimetric length scales of most streaks. In this section we examine behaviour of a sub-millimetric linear plasma synthetic jet actuators and assess their suitability for the modification of streamwise coherent structures.

5.2 Methodology

In this section, a low-profile sub-millimetric actuator design is proposed, which can generate streamwise counter-rotating vortices, based on a linear plasma synthetic jet operating in a suction configuration. In principle, this design could be extended to a dense and uniform array of actuators allowing for the distributed control of local coherent structures. As a fully electronic device with fast response time, it could be combined with MEMS microsensors and respond to flow disturbances in real-time. The scope of this work is to assess the feasibility of using such an actuator to control individual streaks, and we therefore only examine the resulting flow field of a single actuator pair, whilst the investigation of a full array of actuators is left to future work.

Figure 5.1 illustrates a schematic of the proposed actuator. The exposed electrodes have a thickness of 50 μm, but are made flush to surface in order to

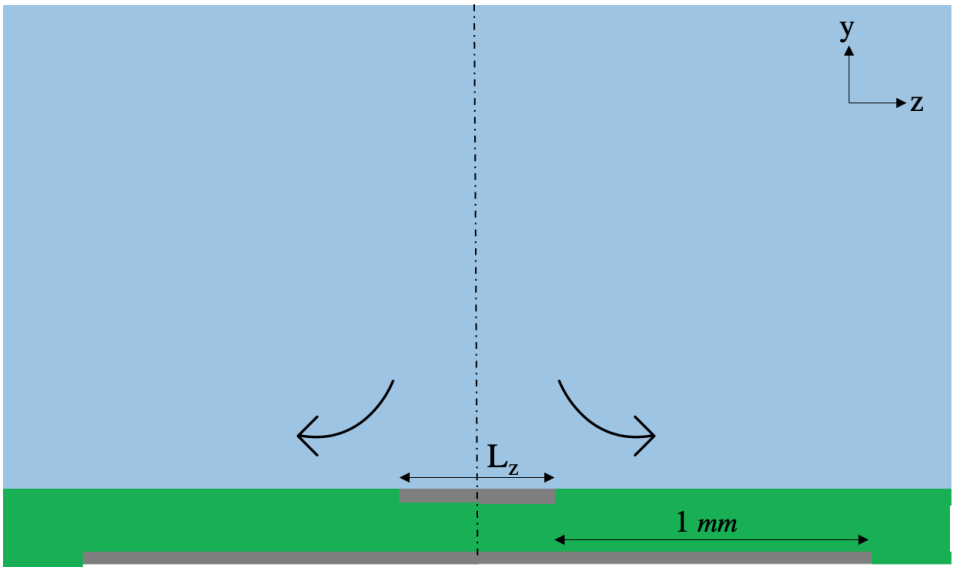

Figure 5.1: *Schematic of actuator design. Green: Dielectric Material, Grey: Electrodes, and Blue: Fluid.*

prevent any surface flow complexity when acting in passive mode. The absence of such an equivalent low profile MEMS sub-millimetric control has made their design difficult to implement [93].

In a notable difference to the actuators investigated in literature, the upper electrode has a span $L_z = 0.25\ mm$, and the lower electrode's half-span = $1.25\ mm$. This reduced scale allows for the generation of a localised actuation at the sub-millimetric scale. By centering the exposed electrode, the design will generate an effective suction on the flow.

The suction configuration was chosen so that the discharges are directed away from each other and will not interact. For an outward jet configuration there is a likelihood of the discharges interacting as the discharge propagation is greater than the half-gap. This interaction would likely cause both physical and numerical artifacts as the assumption of symmetry cannot be strictly assumed due to the unsteady nature of the discharge.

The forcing volume is localised by the short span of the submerged electrode, and the resulting high electric field line curvature. As with other DBD actuators, the absence of any moving parts reduces the required maintenance, and ensures the actuators durability. The small total span of the actuator,

2.5 mm, and the separated lower electrodes allow for this design to be implemented in a dense spatial array, whilst the forcing magnitude can be controlled with changes to the applied voltage profile.

Coherent structures are 3D phenomena, and the modelling of 3D plasma dynamics is still too numerically expensive to be tractable on modern machines. It is therefore necessary to reduce the dimensionality of the problem. The 4-species fluid model described in Chapter 2 [124] is therefore used to calculate a 2D cycle-averaged forcing distribution from a representative AC cycle. This 2D distribution is then extruded to the length of the actuator, neglecting potential end effects. As there is a difference of several orders of magnitude between the associated time scales of the fluid mechanics and the plasma dynamics, a constant cycle-averaged forcing distribution is calculated and assumed to be independent of the flow field.

This forcing distribution was then applied to a 3D laminar boundary layer generated by a flat plate. The resulting dynamics were resolved by direct numerical simulation (DNS) of the full range of turbulent spatial and temporal scales using the spectral element method (SEM) described in detail in [150]. The flow is governed by the Navier-Stokes (NS) equations:

$$\partial_t \boldsymbol{u} + \boldsymbol{u} \cdot \boldsymbol{\nabla} \boldsymbol{u} + \boldsymbol{\nabla} \boldsymbol{p} - Re^{-1} \nabla^2 \boldsymbol{u} + \boldsymbol{F} = 0, \boldsymbol{\nabla} \cdot \boldsymbol{u} = 0 \tag{5.1}$$

Where $\boldsymbol{u} = \{u, v, w\}^T$ and p denote the non-dimensional velocity and pressure respectively. u, v and w are the streamwise, wall-normal and spanwise velocity respectively. The geometry was non-dimensionalised with the half-thickness of the flat plate $R = 1$ mm, such that $x = x^*/R$, $y = y^*/R$, $z = z^*/R$. Finally, the Reynold's number is defined as $Re = U_\infty R/\nu$.

Figure 5.2 shows a cross section in the $x-y$ plane of a flat plate used to generate a boundary layer flow, whilst periodic boundary conditions are applied at $z = 0$ and $z = 12$. The $x - y$ cross-section of the mesh containing 8^{th} order elements is shown in Figure 5.3. In all cases described below the actuator is located

between $\{x, y, z\} = \{30, 1, 6\}$ and $\{30 + L_x, 1, 6\}$. where L_x is the streamwise length of the actuator.

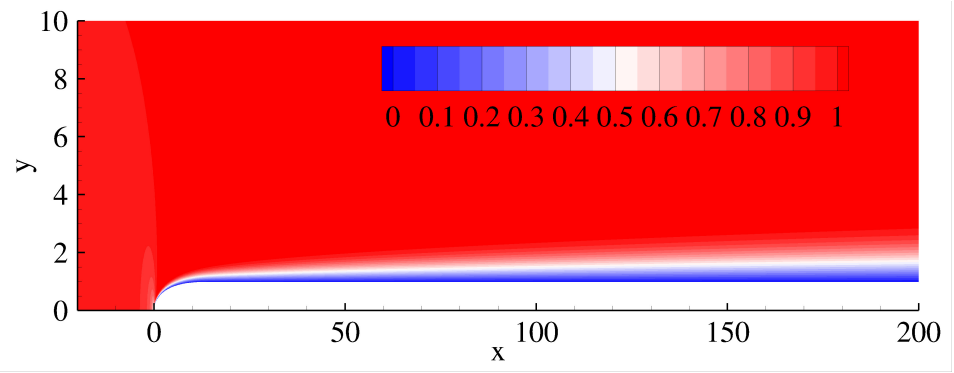

Figure 5.2: *Contours of the streamwise velocity component of the base flow around the upper part of the plate at* $Re = 800$ *corresponding to a unit* $Re = 8e5$.

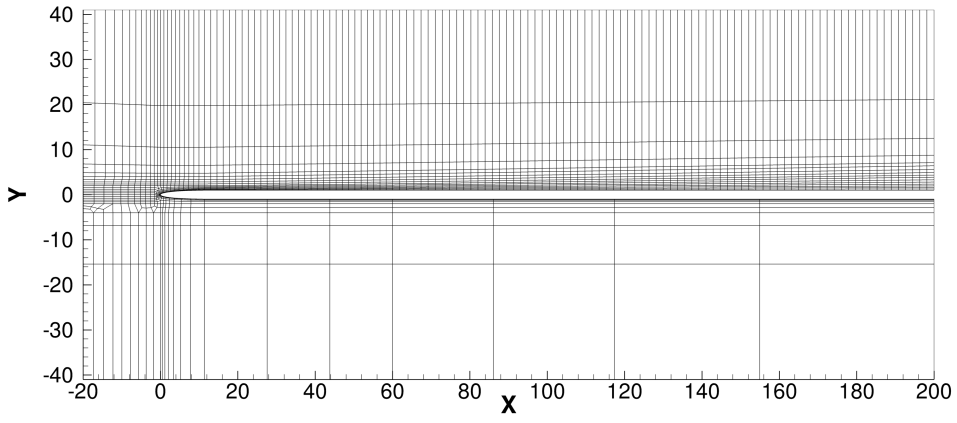

Figure 5.3: *Mesh Schematic of the x-y plane.*

Before the control was implemented, a uniform distribution of 5% turbulence intensity was applied at the inlet, so that the formation of streaks can be observed. Figure 5.4 shows these uncontrolled streaks at $x = 30$. The formation of low and high speed streaks can be clearly seen, with spatial scales closely matching the dimensions of the actuator.

As streaks can be controlled by antagonistic super-position, we therefore examine the flow structures generated by this actuator set-up in a laminar boundary layer and their suitability for controlling streaks. The laminar boundary layer is generated by applying a 0% turbulence intensity at the inlet. After this boundary layer had developed at $x = 30$, varying lengths of actuator were investigated and their resulting flow fields examined.

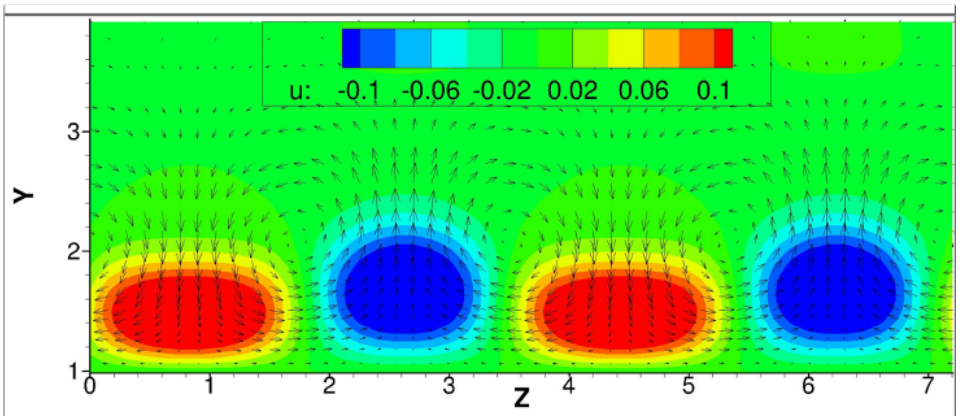

Figure 5.4: *Velocity perturbations in the $y-z$ plane at $x = 30$ without actuation and with 5% uniform turbulence intensity introduced at inlet. The Reynolds number based on boundary layer thickness at this location is $Re_\delta = 560$.*

5.3 Bypass Transition Induced by Plasma Actuation

In this section, the results of the DNS simulations of the flow dynamics generated by actuators with different streamwise lengths, L_x, acting on a laminar boundary layer are presented. In all cases, except where explicitly stated, the sinusoidal applied voltage is $2KV$ at $60KHz$, and the actuator geometry matches that described in the previous section. The formation of boundary layer streaks are observed, and with sufficient actuation so too is an induced bypass transition due to the breakdown of secondary streak instabilities. It is found that both a symmetric and asymmetric breakdowns can be induced by different actuator geometries.

Figure 5.5 shows the streamwise vorticity profile at $x = 50$, $L_x = 50$. The presence of streamwise counter rotating vortices are indicative of the formation of streaks. These structures could be used to suppress the natural formation of streaks via antagonistic superposition.

Figure 5.6 shows the isosurfaces of streamwise velocity perturbation (0.2 for red and -0.2 for blue) for different actuator lengths. The formation of both low-speed and high speed streaks can be observed. If $L_x \leq 50$ the streaks are formed and dissipated without breaking down. However, for longer actuators

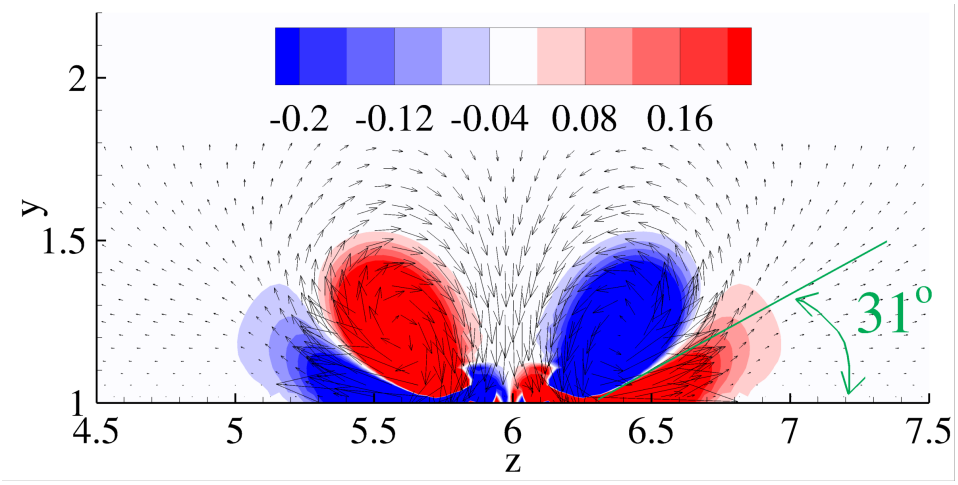

Figure 5.5: *Vorticity contours in the $y-z$ plane with the corresponding velocity vector field induced at $x = 50$, $L_x = 50$ by a millimetric plasma synthetic jet actuator.*

with $L_x > 50$ the streaks continue to grow and lead to breakdown without the presence of freestream turbulence. For short actuation lengths the high speed streak is longer and more prominent. However as the length of actuation increases the relative intensity of the low speed streaks increases. The streak-lifting mechanism discussed in Chapter 1, is identified leading to an inflection point in the velocity profile, and ultimately a symmetric breakdown. This breakdown is significantly further downstream than the end of the actuation region.

Figure 5.7 examines the velocity perturbations of the $L_x = 90$ case at $y = 1.5$ in more detail. It is observed that the low-speed and high speed streaks are formed by the actuator's upwash and downwash respectively. The low-speed streaks then develop an instability and form structures similar to hairpin vortices, leading to a spanwise expansion and ultimately breakdown. The progressive lift-up of the low-speed streaks can also be identified.

The effect of L_x is quantitatively further investigated by examining the streak amplitude A, defined as,

$$A = \frac{1}{2}[max(u - U) + min(u - U)] \tag{5.2}$$

Figure 5.8 shows streak amplitude A as a function of streamwise location x

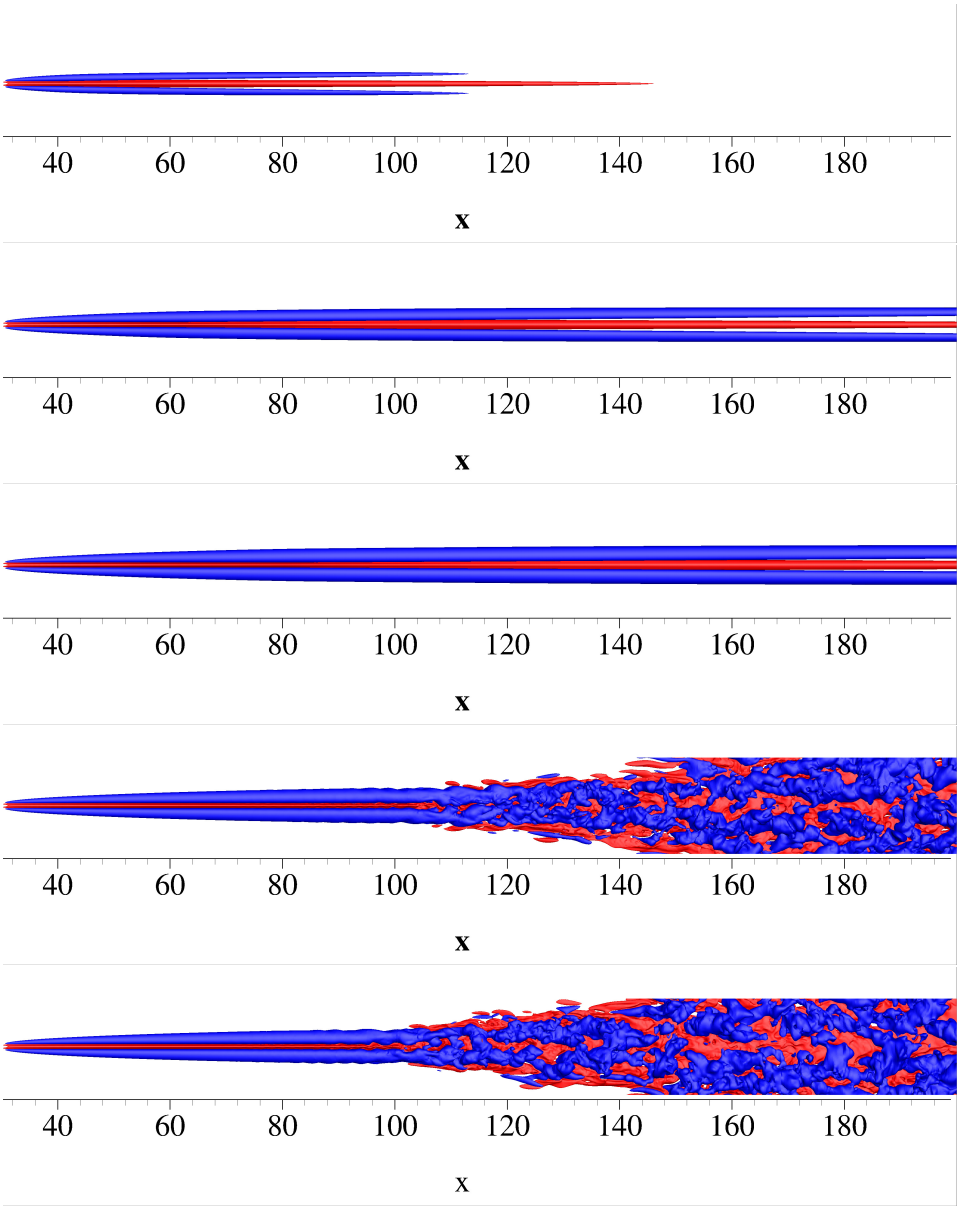

Figure 5.6: *Isosurfaces of streamwise perturbation velocity* 0.1 *(red) and* -0.1 *(blue) for fixed* $L_z = 0.25$ *and varying* L_x*: (a)* $L_x = 10$*, (b)* $L_x = 30$*, (c)* $L_x = 50$*, (d)* $L_x = 70$ *and (e)* $L_x = 90$

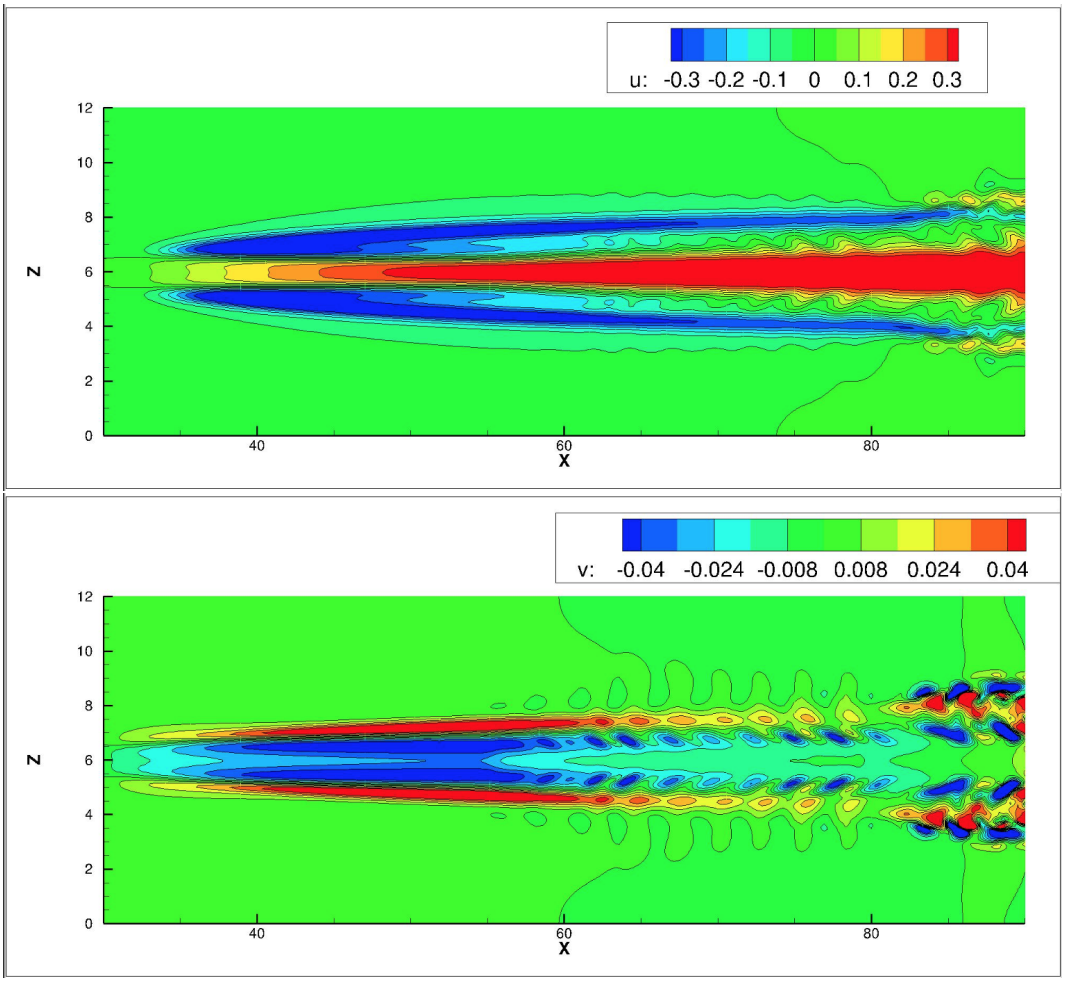

Figure 5.7: *(a) Streamwise and (b) wall-normal velocity perturbations for* $L = 25$ *at* $y = 1.5$

for various values of L_x. Note that for $L_x = 10$, 30 and 50, A is steady, while for $L_x = 70$ and $L_x = 90$, A is an instantaneous value obtained when the mean flow becomes steady. It can be seen that the streak amplitude increases at the same rate for all the cases. For the first three steady cases, A starts to decrease immediately after the plasma region with a similar decay rate. These results are in agreement with experimental results from Jukes and Choi [151], where they investigated three different lengths of plasma actuators and reported that the vortex circulation increases as the length of the plasma actuators increase. Jukes and Choi also reported that the strength of the vortex starts to decrease due to the viscous effect beyond the plasma region. For the three lengths tested, the vortex increased linearly with the plasma length, from which they concluded that longer and stronger vortices can be generated merely by increasing the length of plasma actuation. They also predicted that a limit will be reached for very long plasma actuators, where the viscosity balances the induced momentum. After this limit, the plasma actuator can only act to maintain the vortex instead of continuously increasing it. These conclusions are generally confirmed by this work.

In figure 5.8, the streak amplitude initially increases linearly before $x = 40$ and then the growth rate gradually decrease until a limit is reached at around $x = 80$. For cases where the plasma actuators are longer than the limit, the streak amplitude becomes large enough and breaks down into turbulent flow. It is expected that the breakdown location will remain the same as L_x is increased.

Figure 5.9 compares the λ_2 isosurfaces of the $L_x = 50$ and $L_x = 90$ cases. We see that the apparent hairpin vortices form after the actuation region in the $L_x = 90$ case, whereas they are not present in the $L_x = 50$ case. It is these structures which become unstable and lead to breakdown. Due to the absence of freestream turbulence, it is concluded that these structures must be inherently unstable and do not require external actuation to breakdown.

The nature of this breakdown can be modified by changing the actuator ge-

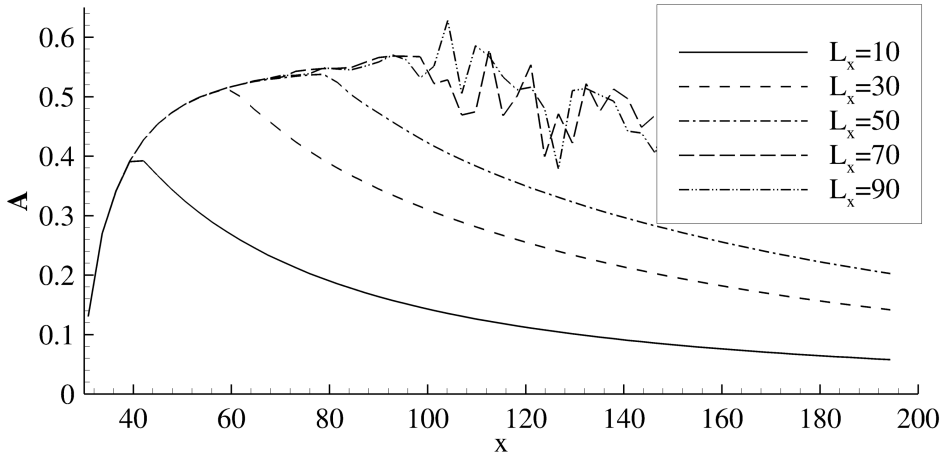

Figure 5.8: *Variation of streak amplitude A against streamwise location x for various values of L_x and fixed $L_z = 0.25$.*

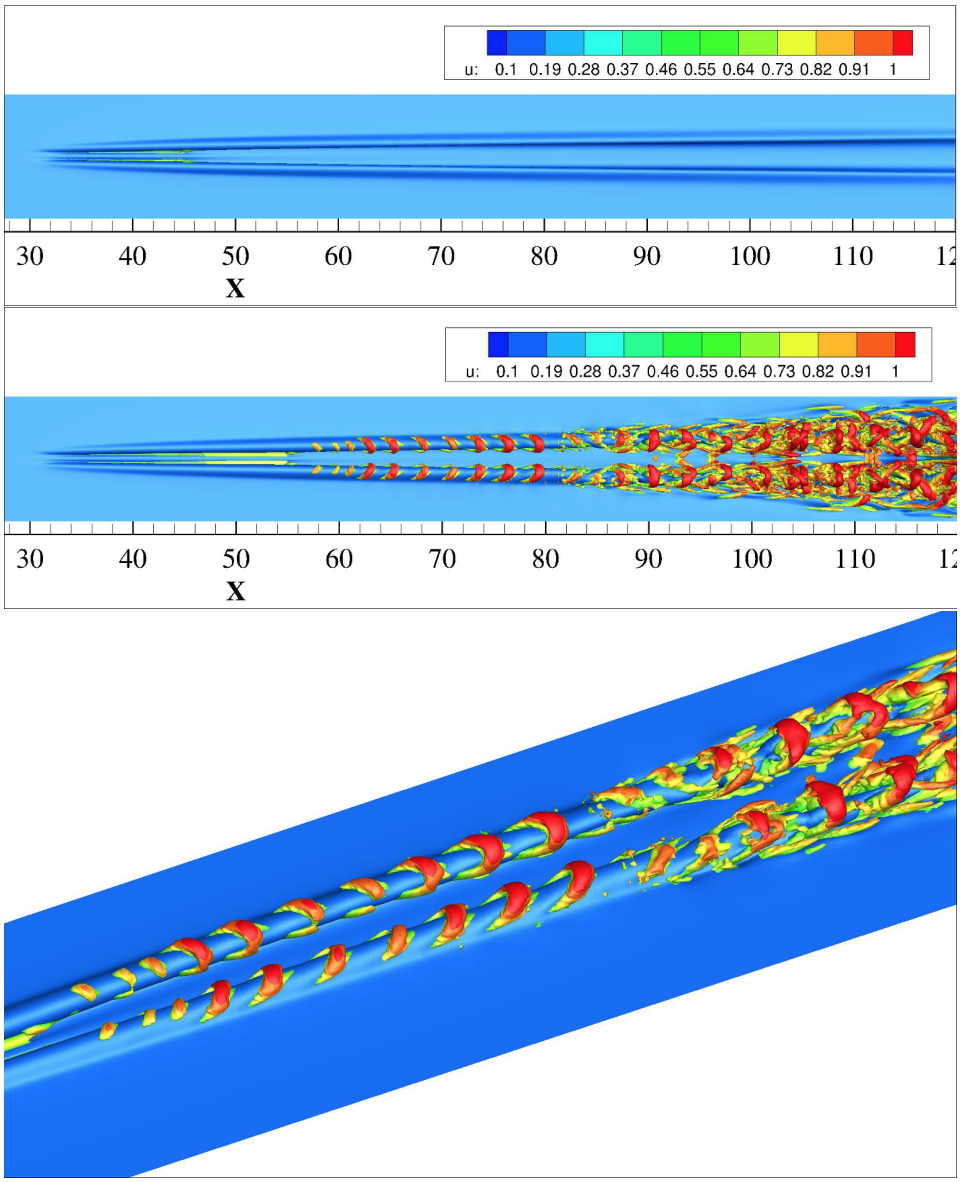

Figure 5.9: *λ_2 isosurfaces for $L_x = 50$ (top), $L_x = 90$ (middle), and a zoomed in view of $L_x = 90$ (bottom).*

ometry. The effect of changing the length of the exposed electrode on the nature of the flow structures and resulting breakdown is examined. As the forcing distribution depends on the length of the submerged electrode and not the length of the exposed electrode, it is therefore reasonable to not recalculate the forcing distributions and simply translate the forcing distributions to account for changes to the span of the exposed electrode. This significantly reduces the computational costs.

Figure 5.10 shows the velocity perturbation isosurfaces for the $L_x = 90$ case with different exposed electrode spans. It can be observed that increasing the span of the exposed electrode, leads to the induced streaks becoming increasingly unstable. When the exposed electrode span is $L_z = 0.1$, the flow structures are stable and dissipate without transition. However as the span is increased to $L_z = 0.25$ the streaks become unstable and we observe the asymmetric breakdown. The increasingly dominant high speed streaks interact with the low-speed streaks, leading to a meandering instability and breakdown. Further increasing the electrode span increases the instability, causing breakdown to occur earlier.

The effect of L_z on the streak amplitude is shown in figure 5.11. In a similar way to before, for cases that break down into turbulence, A is instantaneous and obtained when the mean flow becomes steady. For $L_z = 0.1$, the streak amplitude reaches a peak of 0.4 after $x = 60$, which is because the generated vortices are maintained by the balance between the energy added by the plasma actuators and the viscous interaction with the wall, as predicted by Jukes and Choi. The streaks immediately start to decay beyond the downstream edge of the plasma at $x = 120$. For the remaining three cases with larger L_z, the streak grows at a similar but greater rate and reaches above 0.55 at $x = 90$. The streak amplitude prior to breakdown for $L_z = 0.25$, which corresponds to the asymmetric shape in figure 5.10 (b), is slightly smaller than the other two cases, which correspond to 5.10(c) and (d).

In conclusion, the actuator design specified in the previous section can induce

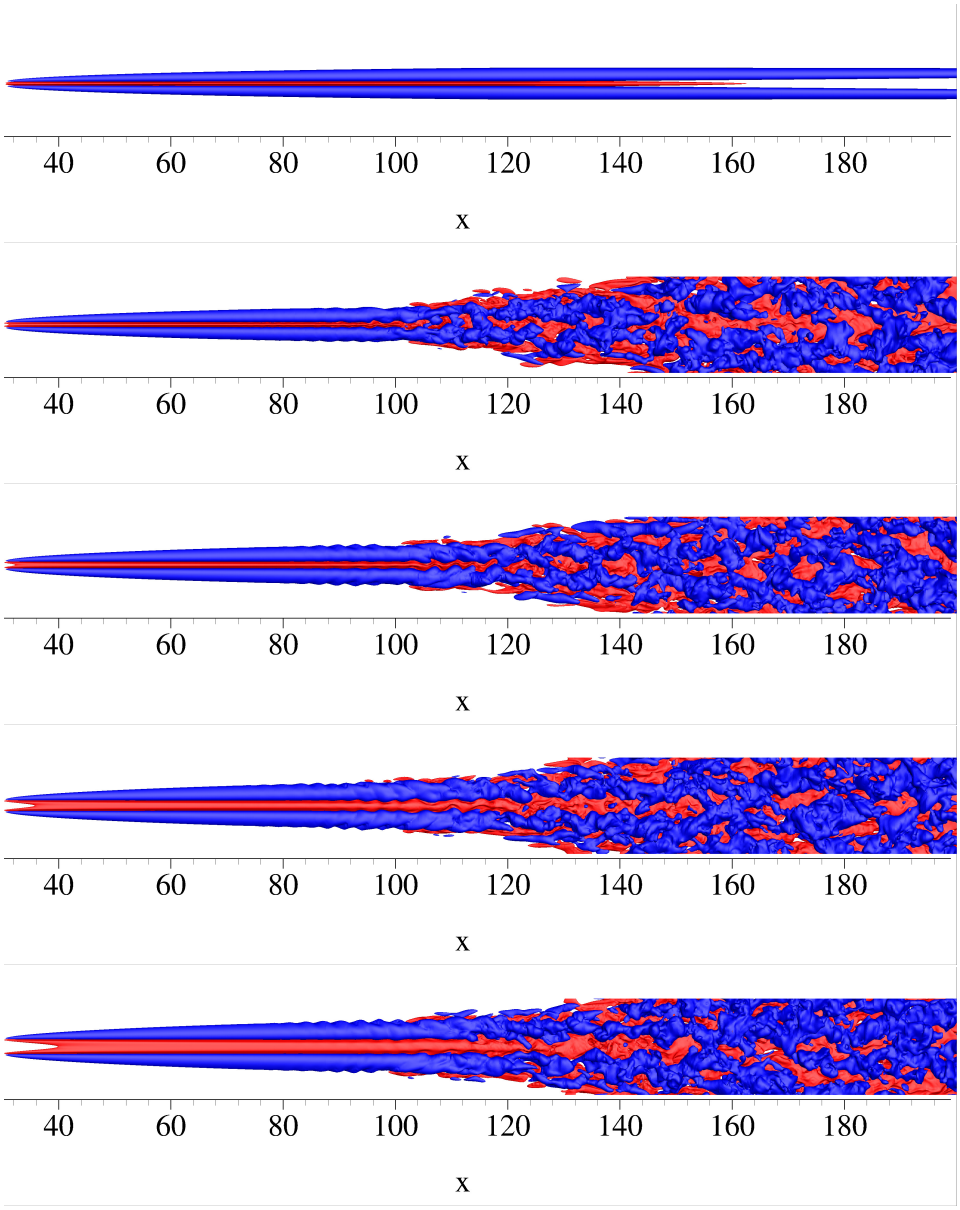

Figure 5.10: *Isosurfaces of streamwise perturbation velocity* 0.1 *(red) and* -0.1 *(blue) for fixed* $L_x = 90$ *and varying* L_z*: (a)* $L_z = 0.1$*, (b)* $L_z = 0.25$*, (c)* $L_z = 0.5$*, (d)* $Lz = 1$ *and (e)* $Lz = 1.5$

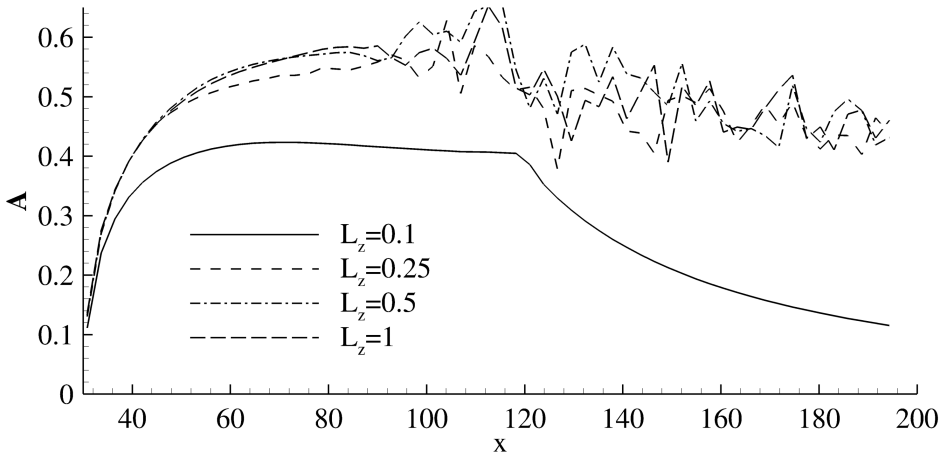

Figure 5.11: *Variation of streak amplitude A against streamwise location x for various values of L_z and fixed $L_x = 90$.*

streaks into a laminar boundary layer. In principle, such an actuator could be used to suppress streaks and transition via antagonistic superposition. Increasing the streamwise length of the actuator leads to the formation of unstable streaks resulting in breakdown even without freestream turbulence. Examining the breakdown of this structure, we note the absence of the meandering instability indicating this is induced by freestream disturbance. The breakdown is caused by the lift-up of low speed streaks, leading to an inflection in the velocity profile. This leads to the formation of hairpin vortex-like structures which are inherently unstable leading to a symmetric breakdown. Changing the span of the exposed electrode can change the breakdown mode. Increasing the electrode span leads to an increased streak instability, and an asymmetric breakdown.

5.4 Variation of the Control Magnitude with Applied Frequency

As the strength of boundary-layer streaks is unpredictable, it is important to vary the magnitude of the induced streaks depending on the conditions. It is practically important that the magnitude of the control can be varied without varying the geometry, ensuring rapid deployment and low cost. This

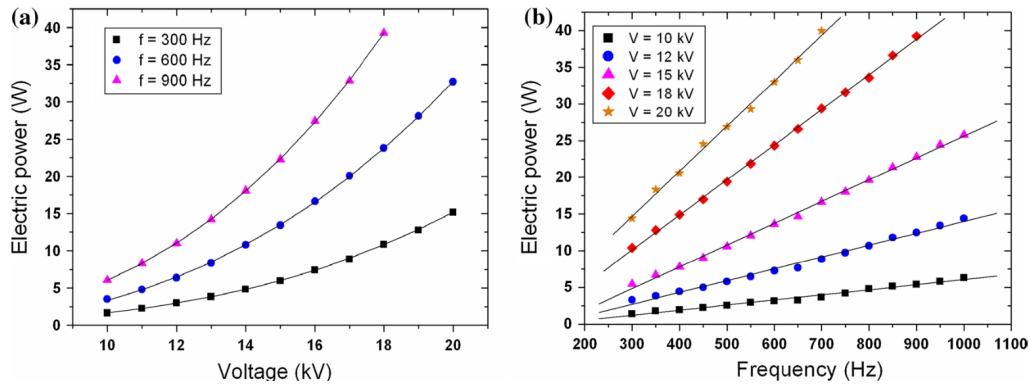

Figure 5.12: *Electrical power consumption versus applied voltage (a) and frequency (b) with a 2-mm-thick dielectric and 20-cm-long electrodes [152].*

can be achieved by implementing different applied voltage profiles to achieve different control magnitudes. It is well documented that operating at either higher frequencies or a higher applied voltage generates a larger EHD force for larger scale DBD actuators [7]. As an actuator's power consumption varies linearly with frequency, and superlinearly with voltage magnitude (shown in figure 5.12), we therefore anticipate a wider range of operating frequencies available for practical implementations, without transitioning to the less efficient streamer regime. It is best to avoid transition to the streamer regime as this will modify both the distribution and direction of the induced forcing altering the behaviour of the induced flow structures.

In this section, the forcing is scaled by varying the applied voltage frequency, as this will limit changes to the forcing distribution. Figure 5.13 shows the cycle-averaged (radial and axial) forcing distributions for different frequency magnitudes. We observe that whilst the positive radial forcing region increases disproportionately with frequency, all other forcing regions increase approximately proportionately with frequency. This relative consistency ensures the resultant forcing direction and distribution does not change significantly within this range of frequencies, with the resultant forcing vector rotating only 8°. This ensures the production of similar streamwise flow structures to the previous sections, with different magnitude streaks being produced.

Figure 5.14 shows the spatially integrated cycle-averaged forcing. Despite a

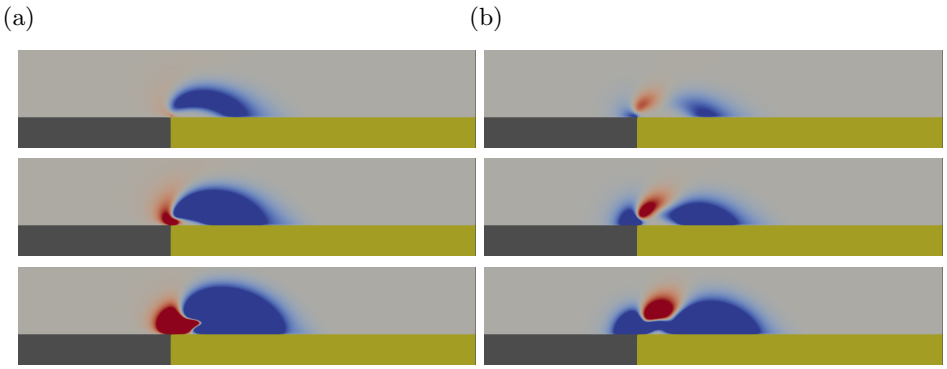

Figure 5.13: *Cycle-average distributions of (a) radial EHD forcing component, $\overline{F_r}$ and (b) axial EHD forcing component $\overline{F_y}$ for actuators operating at different operating frequencies. $f = 20KHz$, $40KHz$, and $60KHz$ from top to bottom.*

limited change in forcing direction, the resultant forcing magnitude increases 400% from $20 - 60kHz$. This super-linear increase indicates a reduced efficiency at lower frequencies. It also suggests that the actuator is capable of inducing counter-rotating streamwise vortices of a wide range of strengths, whilst maintaining a consistent forcing distribution and direction.

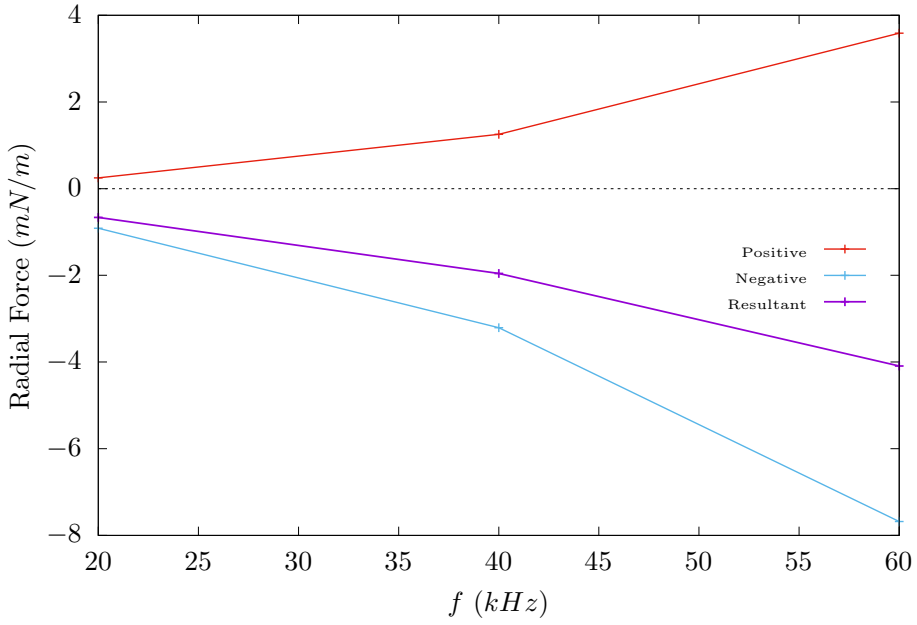

Figure 5.14: *Cycle-averaged and spatially-integrated (a) radial and (b) axial forcing components operating at different frequencies. Each resultant forcing is broken into a positive and a negative component.*

To examine the changes in discharge structure, figure 5.15 compares the forcing contributions from the positive and negative ions in each sub-cycle for the $f = 20\ KHz$ and $f = 60\ kHz$ cases. The forcing contribution from electrons

was found to be small and is not included. During the positive discharge both the contributions of the negative and positive ions increase at higher frequencies, but the contribution of the negative ions increases the most. These additional negative ions are driven towards the exposed electrode edge, making this part of the cycle more antagonistic and accounting for the change in the resultant forcing direction. For each species the radial forcing direction is more uniform than the axial forcing, because the submerged electrode increases the curvature of the electric field lines which must be normal to the electrode surface, ensuring the axial forcing for each species will have both positive and negative components.

The axial forcing is more antagonistic during the negative discharge due to it's less diffuse nature. More plasma is therefore congregated near the edge where the curvature is highest. For all frequencies, the negative discharge is dominated by the positive ions being driven toward the electrode. However, at high frequencies, the antagonistic negative ions play an increasingly important role at the surface. This increase is less obvious than that seen during the positive discharge, and the majority of the increase in forcing during the negative cycle comes from the increasing volume of positive ions near the electrode edge.

Figure 5.16 shows the amplitude of different streaks generated by an actuator operating across a range of frequencies with $L_z = 0.25$ and $L_x = 30$. As the applied frequency is increased from 20 kHz to 60 kHz, the amplitude of the induced streaks increases significantly. This is important, as it would allow this actuator to control a range of naturally occurring streaks via antagonistic superposition. In all cases, there is a consistent profile as the streak amplitude increases over the length of the actuator, and then exponentially decays downstream of the actuator. The peak amplitude of the streaks increases approximately linearly with frequency. However, at higher frequencies the rate the streak amplitude drops off downstream of the actuator is lower.

It is important to see how these time-averaged distributions are formed. To do this the temporal structure of the discharge is investigated. Figure 5.17 shows

(a) The Positive Discharge

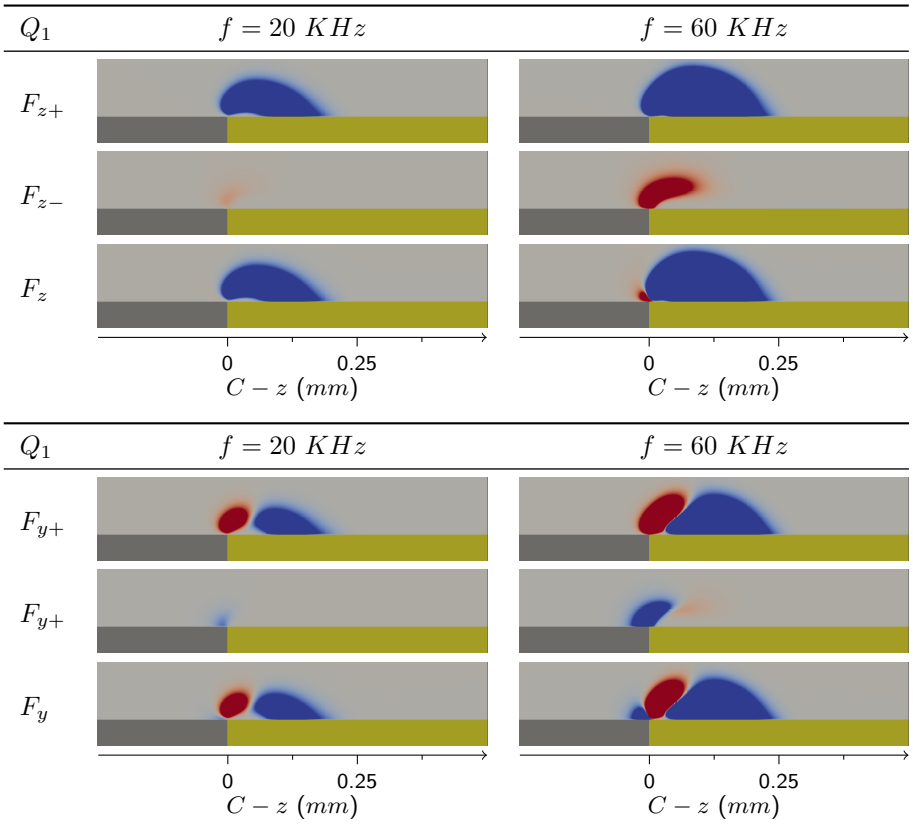

(b) The Negative Discharge

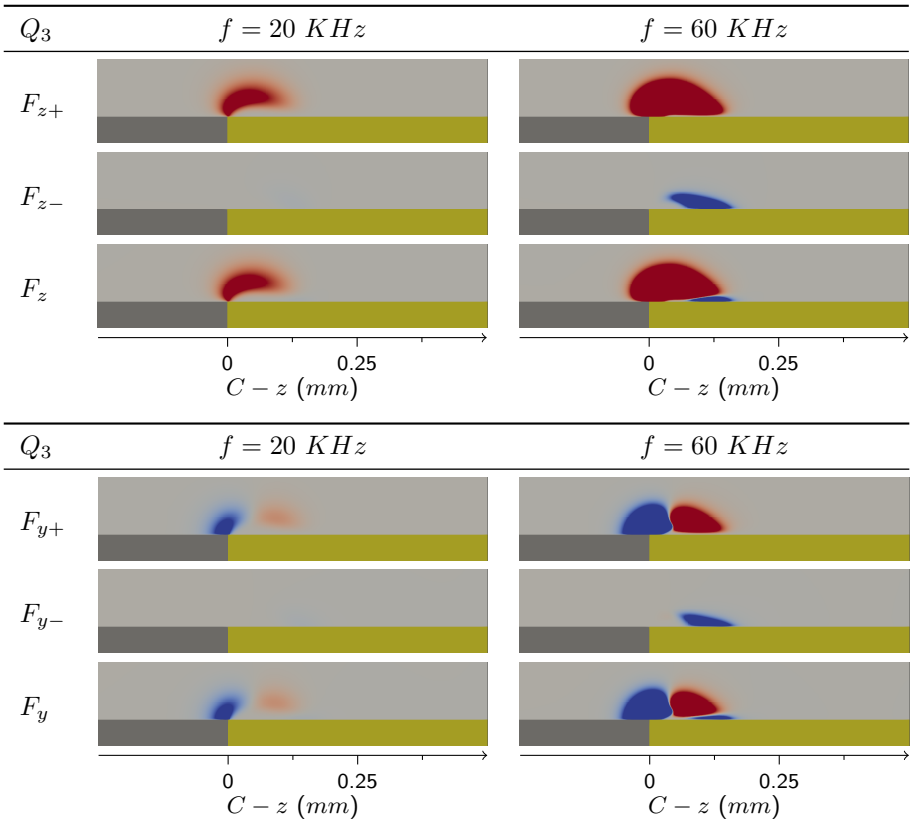

Figure 5.15: *Forcing contributions of the positive ions, negative ions and all species averaged over different periods of activity for* $f = 20KHz$ *and* $f = 60KHz$. *Red:* $\geq 10\ kNmm^{-3}$, *Blue:* $\leq -10\ kNmm^{-3}$.

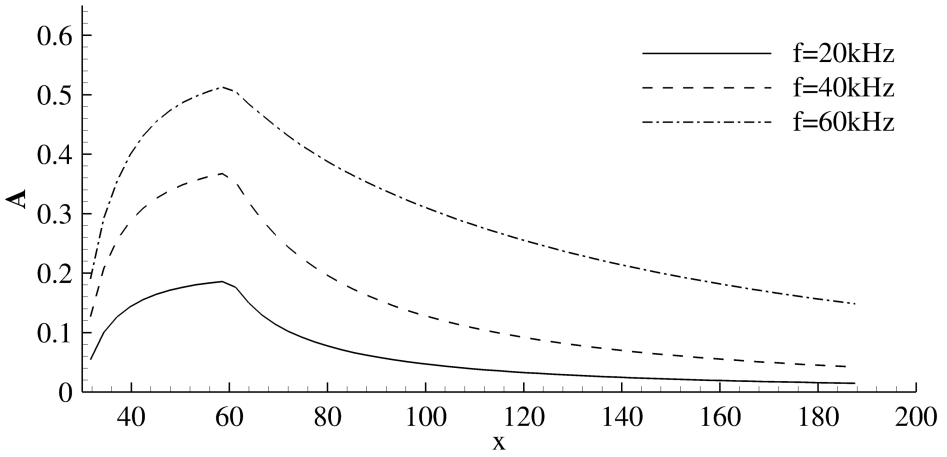

Figure 5.16: *Variation of streak amplitude A against streamwise location x for various applied voltage frequencies f. The geometry is fixed $L_z = 0.25$ and $L_x = 30$*

variation of the spatially-integrated EHD force across the AC cycle. Whilst there are strong similarities with the temporal structure of a larger diameter actuator with similar periods of activity and inactivity, and identifiable positive and negative discharges, there are also some distinct differences. The positive discharge is less diffuse than in larger actuators, whilst the negative discharge is more diffuse. The shorter forcing peaks during the positive discharge are likely due to the smaller area of dielectric charging more quickly by similar mechanisms to those described in Chapter 3. As the frequency increases, the forcing peaks become stronger and earlier. Similarly, the magnitude of the forcing peaks during the negative discharge also increase at high frequencies. In fact, these negative forcing peaks grow significantly more than their positive discharge equivalents. This leads to a reduced resultant radial forcing leading to a reduced effectiveness.

The actuator performance must also be considered across the operating frequency range. Figure 5.18 shows the actuator efficiency and effectiveness as defined in Chapter 3 against frequency. The actuator effectiveness decreases at higher frequencies, due to the relative increase in the negative sub-cycle forcing shown in figure 5.17. However, the efficiency also increases at higher frequency as the increased voltage gradient delays the quenching of the discharge, allowing for more secondary ionisation and a larger discharge volume.

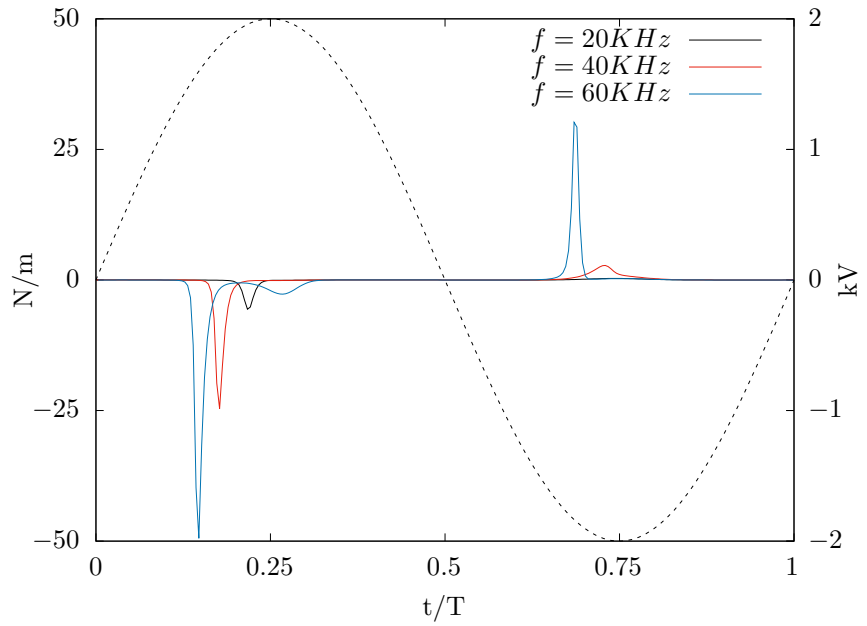

Figure 5.17: *Spatially-integrated radial EHD forcing over a single AC cycle. The dotted line represents the excitation voltage.*

Overall the total efficiency defined as the product of η and ε slightly increases over this frequency range. However this variation is small, and these actuators are efficient over this frequency range.

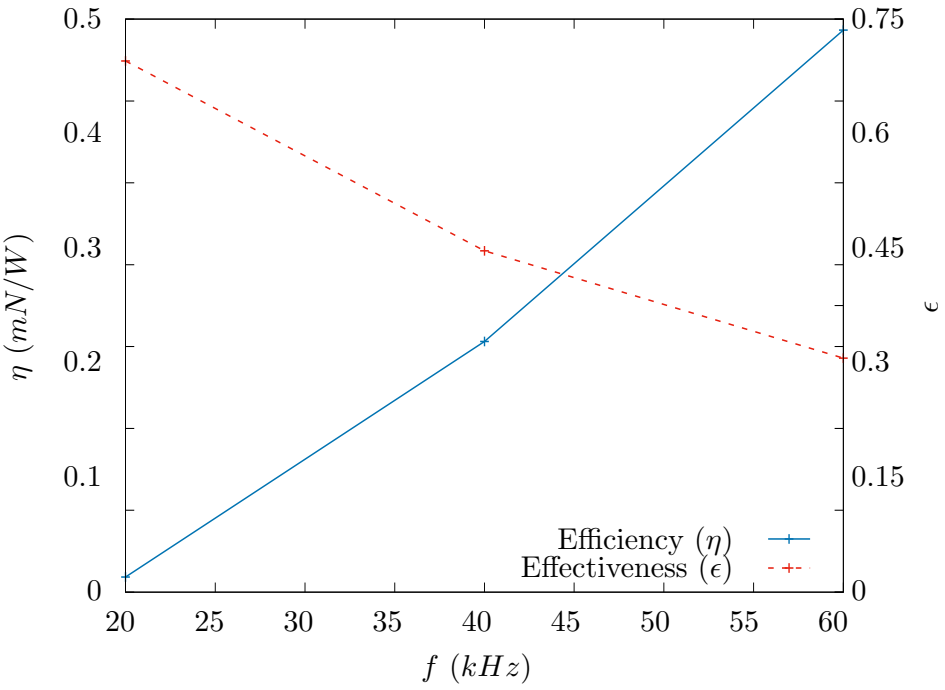

Figure 5.18: *The efficiency η and effectiveness ϵ of actuators operating at different frequencies.*

5.5 Concluding Remarks

In this chapter, a novel actuator design based on a linear plasma synthetic jet operating in a suction configuration is proposed. This design has a very fast response time and can be well integrated with microsensors. This design is also low-profile, reducing surface complexity, and aids easy modelling for practical applications. With a span of 2.5 mm, it can be operated as part of a dense spatial array required for a distributed control system. This study examined the feasibility of utilising this design to suppress streamwise coherent structures. Using a 4-species numerical model the 2D EHD forcing profile was calculated and extruded to various lengths in a 3D laminar boundary layer. The formation of counter-rotating streamwise vortices, as well as the corresponding high and low-speed streaks were observed. These structures could be used to suppress naturally occurring streaks via antagonistic superposition. When the actuator length $L \leq 50$ wall units the induced streaks dissipated without breaking down. However, when $L > 70$ the streaks developed an instability and a symmetric breakdown was observed. Notably no secondary (meandering) instability was observed, indicating this was induced by the freestream turbulence not present in the simulation. Different widths of exposed electrode were also investigated. Wider exposed electrodes were found to induce more unstable streaks, with an asymmetric breakdown being observed for $L = 90$ and an exposed electrode span ≥ 0.25.

The ability to control the magnitude of the induced streaks without modifying the geometry was also investigated. This was achieved by varying the frequency of the applied voltage profile, to ensure a consistent discharge structure and corresponding forcing distribution. It was found that varying the frequency f from 20 kHz to 60 kHZ increased the induced cycle-averaged EHD force by 400% whilst maintaining a consistent discharge structure and direction which varied by only 8°. The small scale of the actuator and reduced dielectric surface resulted in the early quenching and a less continuous discharge than equivalent

larger scale actuators. At higher frequencies the discharge was found to become more antagonistic, with a larger volume of negative ions being produced during the positive and the negative discharges. Despite this, higher frequencies were found to increase the actuator efficiency. The resulting streak amplitudes were found to vary significantly across the frequency range, with an induced frequency magnitude increase of 290% between $f = 20\ kHz$ and $f = 60\ kHz$ being observed.

Chapter 6

Summary and Conclusions

Millimetric and sub-millimetric DBD plasma actuators are investigated for flow control applications. Other actuators have been shown to control coherent structures and boundary layer transition with an extremely high efficiency. However due to their mechanical nature, the feasibility of applying these devices is far from certain. DBD actuators are fully electronic, do not have any moving parts, and are cheap to manufacture, addressing these issues. The low resolution of experiments, and the high computational cost of fully resolving the plasma physics means that there has been limited progress in understanding and applying DBD actuators. A number of phenomenological models exist, which use empirical observations to reduce the computational cost. However, these models fail to predict the experimentally observed behaviour of DBD actuators at the millimetric and sub-millimetric scales.

This work has utilised the recent progress in plasma modelling, as well as improved computing power, to model the plasma mechanics over a relevant time period with a 4-species fluid model. By resolving the plasma structures, a deeper understanding of the mechanics of DBD plasma actuators at all scales has been developed.

In Chapter 3, the mechanics behind an unexplained flow reversal phenomena first observed by Humble et al. [153] are examined. Here, as the scale of the millimetric annular DBD actuator is reduced, the direction of the perpendic-

ular jet is reversed. The curvature of the electric field lines at the millimetric and the sub-millimetric scale were found to have a significant effect on the discharge. The AC cycle of the actuator necessitates an antagonistic discharge, with distinct structures being observed during the positive-going positive part of the cycle, and the negative-going negative part. These periods are termed positive discharge and negative discharge, respectively. The differences in discharge structure observed during these periods, leads to different forcing volumes, and the production of a net resultant force, which controls the direction of flow.

As the scale of the actuator is reduced, unequal changes to the discharge structures during each half-cycle are identified. The positive discharge becomes more intermittent significantly reducing the plasma and forcing volumes. Meanwhile, the microdischarges during the negative cycle reduce in intensity, but time-average forcing over this half-cycle is unaffected. It was determined that these modifications to the structure are due to the rate at which the surface is charged. By reducing the scale of the actuator, the curvature of the electric field lines increases with more current being directed towards the surface. This increases the rate at which the surface is charged, leading to an increased quenching of the positive discharge. The reduction in negative-cycle microdischarge intensity was also found to disproportionately reduce the forcing generated during the positive discharge. The reduction in microdischarge intensity significantly reduces the negative charge deposited on the surface and the propagation of the negative discharge. The absence of this negative charge, reduces the potential difference and leads to earlier quenching during the subsequent discharge cycle.

In Chapter 4, the effect of variations in the actuator geometry, and ambient gas-fraction effect on the performance of annular actuators of different scales is investigated. It was possible to reverse the axial flow direction at a constant actuator diameter by modifying either the exposed electrode thickness or the oxygen gas-fraction in isolation. In both cases, the modifications of the dis-

charge structure and resulting EHD forcing, are due to the increased local rate of production of both positive and negative ions. Reductions in the exposed electrode thickness lead to an increased local electric field strength near the edge of the exposed electrode. On the other hand, an increased oxygen gas-fraction reduces the mean electron energy required for the production of both positive and negative ions, although the increase in negative ions is larger. Both cases increase the discharge intensity, and the production of negative ions, which have a higher threshold for ionisation. This crucially affects the discharge structure of each sub-cycle differently. Generally, the increased discharge intensity leads to more intense negative cycle microdischarges. These short lived and relatively high current structures lead to a strong increase in the negative charge deposited on the dielectric surface. Their transient nature ensures that the forcing production does not increase during this cycle. However the increase in negative charge being deposited during the negative cycle leads to an increase in the volume of the subsequent positive discharge. This increases discharge asymmetry and encourages the development of an outward jet.

As the oxygen gas-fraction of a 2 mm actuator is increased above 60%, the high local production of ions leads to the formation of positive streamers during the positive sub-cycle. This leads to a collapse of the plasma volume during the positive subcycle and the subsequent increase of the plasma volume during the negative sub-cycle. This causes the reversal of the axial jet from an outward one to an inward one. It also explains why experimental observations of filamentary annular DBD actuators found the threshold of reversal to be larger than our numerical works operating in the corona regime. The understanding that streamer regimes lead to a reduced thrust, at least initially, due to the increase in the antagonistic negative discharge is useful for all DBD configurations.

Efficiency also reduces with more constricted higher-current discharges. Generally, smaller actuators generating an inward axial jet have a lower effectiveness

than their outward counterparts. This is due to the similar magnitudes of the antagonistic positive and negative discharges. However, at high oxygen gas-fractions, there is an increased production of negative ions, which behave antagonistically to the positive ions. This leads to a reduced effectiveness for actuators generating an outward axial jet at high oxygen gas-fractions. Some works record a positive contribution of the negative ions during the negative discharge, but this was not observed for our cases.

In Chapter 5, a new design of sub-millimetric actuator is examined. This parallel configuration can generate streamwise vortices, indicating the potential for the suppression of boundary layer streaks via antagonistic superposition. To assess the performance of this design the forcing contributions were tested in a laminar boundary layer and the resulting flow structures examined. Firstly different geometries of actuator were tested. For actuators with a length $L_x \leq 50$ and fixed width $L_z = 0.25$, streaks were generated but dissipated without breaking down. However, for actuators with $L_x \geq 70$, a bypass transition was observed. Our simulations utilised a smooth laminar boundary layer without free-stream turbulence. The meandering instability was not observed, supporting the theory that this is induced by free stream turbulence [154]. The effect of varying the width of the actuator was also investigated. Wider actuators induced a symmetric breakdown. For an active flow control device to actively control streaks, it is important that the magnitude of the generated streaks can be controlled. To do this without varying the actuator geometry, the applied voltage frequency was varied. It was found that by varying the frequency between $20 - 60\ kHz$, the induced forcing could be varied by 400%, without strong changes to the discharge structure. This approach increased the magnitude of the induced streaks by 290%.

Bibliography

[1] B. Graver, D. A. N. Rutherford, and S. Zheng, "CO2 Emissions From Commercial Aviation - 2013, 2018 and 2019," no. October, 2020.

[2] Assorted, "Intergovernmental Panel on Climate Change - Data Distribution Centre," *IPCC*, 2020. [Online]. Available: https://www.ipcc-data.org/

[3] C. Façanha, K. Blumberg, J. Miller, D. Kodjak, F. Kamakaté, C. Malins, J. German, A. Bandivadekar, A. Lloyd, B. Sharpe, D. Rutherford, E. Olivares, F. Fung, H. Wang, J. Schultz, M. Zeinali, N. Lutsey, R. Muncrief, R. Minjares, S. Searle, and Z. Shao, "Global Transportation Energy and Climate Roadmap The impact of transportation policies and their potential to reduce oil consumption and greenhouse gas emissions," 2012. [Online]. Available: www.theicct.org

[4] M. A. Leschziner, H. Choi, and K. S. Choi, "Flow-control approaches to drag reduction in aerodynamics: Progress and prospects," *Philosophical Transactions of the Royal Society A: Mathematical, Physical and Engineering Sciences*, vol. 369, no. 1940, pp. 1349–1351, 2011.

[5] E. Moreau, A. Debien, N. Bénard, T. Jukes, R. Whalley, K. Choi, A. Berendt, J. Podliński, and J. Mizeraczyk, "Surface Dielectric Barrier Discharge Plasma Actuators," *ERCOFTAC Bulletin*, vol. 94, pp. 5–10, 2013. [Online]. Available: http://www.ercoftac.org/downloads/sig20/actuators{_}moreau.pdf/

[6] T. N. Jukes and K.-S. Choi, "Flow control around a circular cylinder using pulsed dielectric barrier discharge surface plasma," *Physics of Fluids*, vol. 21, no. 2009, p. 084103, 2009. [Online]. Available: http://scitation.aip.org/content/aip/journal/pof2/21/8/10.1063/1.3194307

[7] N. Benard and E. Moreau, "Electrical and mechanical characteristics of surface AC dielectric barrier discharge plasma actuators applied to airflow control," *Experiments in Fluids*, vol. 55, no. 11, p. 1846, nov 2014. [Online]. Available: http://link.springer.com/10.1007/s00348-014-1846-x

[8] J. Little, K. Takashima, M. Nishihara, I. Adamovich, and M. Samimy, "Separation Control with Nanosecond Pulse Driven Dielectric Barrier Discharge Plasma Actuators," *AIAA Journal*, vol. 50, no. 2, pp. 350–365, 2012.

[9] P. Peschke, "Experimental Investigation of Pulsed DBD Plasma Actuators for Aerodynamic Flow Control," 2014. [Online]. Available: http://infoscience.epfl.ch/record/200229

[10] V. Bityurin, J. Lineberry, V. Potebnia, V. Alferov, A. Kuranov, and E. Sheikin, "Assessment of Hypersonic MHD Concepts," *AIAA Journal*, no. 301, p. 5559, 1997.

[11] J. D. Jackson, *Classical electrodynamics*. Wiley, 1975. [Online]. Available: https://cds.cern.ch/record/100964

[12] J. M. Meek, "A Theory of Spark Discharge," *Phys. Rev*, 1940.

[13] Y. P. Raizer and J. E. Allen, *Gas discharge physics*. Springer Berlin, 1997, vol. 2.

[14] J. R. Roth, D. M. Sherman, S. P. Wilkinson, B. Drive, J. Reece, and M. Sherman, "Boundary Layer Flow Control With A One Atmosphere Uniform Glow Discharge Surface Plasma," *Aiaa*, vol. 28, no. 03, 1998.

[15] T. Michelis and M. Kotsonis, "Flow Control on a Transport Truck Side Mirror Using Plasma Actuators," *Journal of Fluids Engineering*, vol. 137, no. 11, p. 111103, jul 2015. [Online]. Available: http://fluidsengineering.asmedigitalcollection.asme.org/article.aspx?doi=10.1115/1.4030724

[16] G. Eoker, "Electrode components of the arc discharge," in *Ergebnisse der Exakten Naturwissenschaften*. Berlin, Heidelberg: Springer Berlin Heidelberg, 1961, pp. 1–104.

[17] A. Nakano and H. Nishida, "The effect of the voltage waveform on performance of dielectric barrier discharge plasma actuator," *Journal of Applied Physics*, vol. 126, no. 17, p. 173303, 2019.

[18] T. C. Corke, C. L. Enloe, and S. P. Wilkinson, "Dielectric Barrier Discharge Plasma Actuators for Flow Control*," *Annual Review of Fluid Mechanics*, vol. 42, no. 1, pp. 505–529, 2010.

[19] B. MERTZ and T. C. CORKE, "Single-dielectric barrier discharge plasma actuator modelling and validation," *J. Fluid Mech*, vol. 669, pp. 557–583, 2011. [Online]. Available: https://www-cambridge-org.ezproxy.nottingham.ac.uk/core/services/aop-cambridge-core/content/view/ADECA6BB257AD69C21F65B97CC76A98A/S0022112010005203a.pdf/singledielectric{_}barrier{_}discharge{_}plasma{_}actuator{_}modelling{_}and{_}validation.pdf

[20] C. L. Enloe, T. E. Mclaughlin, R. D. Vandyken, K. D. Kachner, E. J. Jumper, and T. C. Corke, "Mechanisms and Responses of a Single Dielectric Barrier Plasma Actuator: Plasma Morphology Introduction: Morphology of the Plasma Actuator," *AIAA JOURNAL*, vol. 42, no. 3, 2004. [Online]. Available: http://www3.nd.edu/{~}sst/teaching/AME60637/reading/2004{_}AIAA{_}Enloe{_}et{_}al{_}dbd.pdf

[21] D. Orlov, T. Corke, and M. Patel, "Electric Circuit Model for Aerodynamic Plasma Actuator," in *44th AIAA Aerospace Sciences Meeting and Exhibit*. Reston, Virigina: American Institute of Aeronautics and Astronautics, jan 2006. [Online]. Available: http://arc.aiaa.org/doi/10.2514/6.2006-1206

[22] J. P. Boeuf, Y. Lagmich, T. Unfer, T. Callegari, and L. C. Pitchford, "Electrohydrodynamic force in dielectric barrier discharge plasma actuators," *Journal of Physics D: Applied Physics*, vol. 40, no. 3, pp. 652–662, 2007. [Online]. Available: http://stacks.iop.org/0022-3727/40/i=3/a=S03?key=crossref.602cdfe93259b6e4678cf12a749c567d

[23] A. Likhanskii, M. Shneider, D. Opaits, R. Miles, and S. Macheret, "Numerical modeling of DBD plasma actuators and the induced air flow," *38th Plasmadynamics and Lasers Conference*, no. December 2014, 2007. [Online]. Available: http://arc.aiaa.org/doi/10.2514/6.2007-4533

[24] K. Takashima, Y. Zuzeek, W. R. Lempert, I. V. Adamovich, and M. A. Chaszeyka, "Characterization of Surface Dielectric Barrier Discharge Plasma Sustained by Repetitive Nanosecond Pulses," *AIAA Plasmadynamics and Lasers Conference*, 2010. [Online]. Available: http://www.enu.kz/repository/2010/AIAA-2010-4764.pdf

[25] J.-P. Boeuf, "Modeling and comparison of sinusoidal and nanosecond pulsed surface dielectric barrier discharges for flow control," *Plasma Phys. Control. Fusion*, vol. 52, 2010. [Online]. Available: http://iopscience.iop.org/article/10.1088/0741-3335/52/12/124019/pdf

[26] M. Abdollahzadeh, F. Rodrigues, J. C. Pascoa, and P. J. Oliveira, "Numerical design and analysis of a multi-DBD actuator configuration for the experimental testing of ACHEON nozzle model," *Aerospace Science and Technology*, vol. 41, no. January 2011, pp. 259–273, 2015.

[27] S. Goekce, "Plasma Diagnostics and Modelling of Nanosecond Pulsed Actuators," *EPFL Publications*.

[28] J. P. Boeuf, Y. Lagmich, and L. C. Pitchford, "Contribution of positive and negative ions to the electrohydrodynamic force in a dielectric barrier discharge plasma actuator operating in air," *Journal of Applied Physics*, vol. 106, no. 2, 2009.

[29] A. Debien, N. Benard, L. David, and E. Moreau, "Unsteady aspect of the electrohydrodynamic force produced by surface dielectric barrier discharge actuators," *Applied Physics Letters*, vol. 100, no. 1, pp. 3–6, 2012.

[30] A. V. Likhanskii, M. N. Shneider, S. O. MacHeret, and R. B. Miles, "Modeling of dielectric barrier discharge plasma actuator in air," *Journal of Applied Physics*, vol. 103, no. 5, 2008.

[31] C. L. Enloe, M. G. McHarg, G. I. Font, and T. E. McLaughlin, "Plasma-induced force and self-induced drag in the dielectric barrier discharge aerodynamic plasma actuator," *47th AIAA Aerospace Sciences Meeting*

including the New Horizons Forum and Aerospace Exposition, no. January, 2009.

[32] N. Benard, A. Debien, and E. Moreau, "Time-dependent volume force produced by a non-thermal plasma actuator from experimental velocity field," *Journal of Physics D: Applied Physics*, vol. 46, no. 24, 2013.

[33] M. Neumann, C. Friedrich, J. Czarske, J. Kriegseis, and S. Grundmann, "Determination of the phase-resolved body force produced by a dielectric barrier discharge plasma actuator," *Journal of Physics D: Applied Physics*, vol. 46, no. 4, 2013.

[34] K. Kourtzanidis, G. Dufour, and F. Rogier, "Explaining the electrohydrodynamic force and ionic wind spatiotemporal distribution in surface AC dielectric barrier discharge actuators." *ArXiv Preprint*, 2020.

[35] J. Pons, E. Moreau, and G. Touchard, "Asymmetric surface dielectric barrier discharge in air at atmospheric pressure: electrical properties and induced airflow characteristics," *J. Phys. D: Appl. Phys*, vol. 38, pp. 3635–3642, 2005.

[36] F. O. Thomas, T. C. Corke, M. Iqbal, A. Kozlov, and D. Schatzman, "Optimization of dielectric barrier discharge plasma actuators for active aerodynamic flow control," *AIAA Journal*, vol. 47, no. 9, pp. 2169–2178, 2009.

[37] M. L. Post and T. Corke, "Plasma actuators for separation control on stationary and oscillating airfoils," NOTRE DAME UNIV IN, Tech. Rep., 2004.

[38] R. A. Humble, S. A. Craig, J. Vadyak, P. D. McClure, J. W. Hofferth, and W. S. Saric, "Spatiotemporal structure of a millimetric annular dielectric barrier discharge plasma actuator," *Physics of Fluids*, vol. 25, no. 1, 2013.

[39] Y. Yang and G. Zha, "Super-Lift Coefficient of Active Flow Control Airfoil: What is the Limit?" in *55th AIAA Aerospace Sciences Meeting*. Reston, Virginia: American Institute of Aeronautics and Astronautics, jan 2017. [Online]. Available: http://arc.aiaa.org/doi/10.2514/6.2017-1693

[40] D. M. Bushnell, "Aircraft drag reduction-a review," *J. Aerospace Engineering*, vol. 217, pp. 1–18, 2003.

[41] O. Reynolds, "XXIX. An experimental investigation of the circumstances which determine whether the motion of water shall be direct or sinuous, and of the law of resistance in parallel channels," *Philosophical Transactions of the Royal society of London*, no. 174, pp. 935–982, 1883.

[42] J. H. M. Fransson and S. Shahinfar, "On the effect of free-stream turbulence on boundary-layer transition," *Journal of Fluid Mechanics*, vol. 899, 2020.

[43] W. Tollmien, "The origin of turbulence," *1st message. Head of Department, Wiss. Gottingen, Math. Phys. Class*, pp. 21–44, 1929.

[44] V. H. Schlichting, "Laminar beam propagation," *ZAMM-Journal of Applied Mathematics and Mechanics / Zeitschrift f {\ "u} r Applied Mathematics and Mechanics*, vol. 13, no. 4, pp. 260–263, 1933.

[45] H. Schlichting and K. Gersten, *Boundary-layer theory*. Springer, 2016.

[46] F. M. White, *Viscous fluid flow*, 2006.

[47] P. J. Schmid, D. S. Henningson, and D. F. Jankowski, "Stability and transition in shear flows. applied mathematical sciences, vol. 142," *Appl. Mech. Rev.*, vol. 55, no. 3, pp. B57—-B59, 2002.

[48] J. Sun, *Open Aircraft Performance Modeling Based on an Analysis of Aircraft Surveillance Data*, 2019.

[49] R. J. Lingwood, "The absolute instability of the boundary layer on a rotating cone," *J. Fluid Mech.*, vol. 299, no. 3, pp. 17–33, 1995.

[50] L. M. Mack, "Boundary-layer linear stability theory," California Inst of Tech Pasadena Jet Propulsion Lab, Tech. Rep., 1984.

[51] M. V. Morkovin and E. Reshotko, "Dialogue on progress and issues in stability and transition research," in *Laminar-turbulent transition*. Springer, 1990, pp. 3–29.

[52] A. Lundbladh and A. V. Johansson, "Direct simulation of turbulent spots in plane Couette flow," *Journal of Fluid Mechanics*, vol. 229, pp. 499–516, 1991.

[53] V. A. Romanov, "Stability of plane-parallel Couette flow," *Functional analysis and its applications*, vol. 7, no. 2, pp. 137–146, 1973.

[54] P. Klebanoff, "Characteristics of turbulence in a boundary layer with zero pressure gradient," NATIONAL BUREAU OF STANDARDS GAITHERSBURG MD, Tech. Rep., 1955.

[55] J. KENDALL, "Boundary layer receptivity to freestream turbulence," in *21st Fluid Dynamics, Plasma Dynamics and Lasers Conference*, 1990, p. 1504.

[56] J. Kendall, "Experiments on boundary-layer receptivity to freestream turbulence," in *36th AIAA Aerospace Sciences Meeting and Exhibit*, 1998, p. 530.

[57] T. Ellingsen and E. Palm, "Stability of linear flow," *The Physics of Fluids*, vol. 18, no. 4, pp. 487–488, 1975.

[58] M. T. Landahl, "A note on an algebraic instability of inviscid parallel shear flows," *Journal of Fluid Mechanics*, vol. 98, no. 2, pp. 243–251, 1980.

[59] a. Sveningsson, "Transition Modelling – A Review," *October*, no. 1958, 2006.

[60] J. C. R. Hunt and P. A. Durbin, "Perturbed vortical layers and shear sheltering," *Fluid dynamics research*, vol. 24, no. 6, p. 375, 1999.

[61] J. D. Swearingen and R. F. Blackwelder, "The growth and breakdown of streamwise vortices in the presence of a wall," *Journal of Fluid Mechanics*, vol. 182, pp. 255–290, 1987.

[62] P. Andersson, L. Brandt, A. Bottaro, and D. S. Henningson, "On the breakdown of boundary layer streaks," *Journal of Fluid Mechanics*, vol. 428, pp. 29–60, 2001.

[63] M. Matsubara and P. H. Alfredsson, "Disturbance growth in boundary layers subjected to free-stream turbulence," *Journal of fluid mechanics*, vol. 430, pp. 149–168, 2001.

[64] S. K. Robinson, "The kinematics of turbulent boundary layer structure." 1992.

[65] S. J. Kline, W. C. Reynolds, F. A. Schraub, and P. W. Runstadlers, "The structure of turbulent boundary layers." *J . Fluid Mech.*, vol. 30, 1967.

[66] G. Alfonsi, "Coherent structures of turbulence: Methods of eduction and results," *Applied Mechanics Reviews*, vol. 59, no. 1-6, pp. 307–323, 2006.

[67] R. F. Blackwelder and H. Eckelmann, "Streamwise vortices associated with the bursting phenomenon," *Journal of Fluid Mechanics*, vol. 94, no. 3, pp. 577–594, 1979.

[68] W. Schoppa and F. Hussain, "Coherent structure generation in near-wall turbulence," *Journal of Fluid Mechanics*, vol. 453, pp. 57–108, 2002.

[69] J. JEong and F. Hussain, "On the identification of a vortex," *Journal of Fluid Mechanics*, vol. 285, no. January 1995, pp. 69–94, 1995.

[70] Z. Harun and L. E. Reda, "Generation, Evolution, and Characterization of Turbulence Coherent Structures," *IntechOpen*, p. 38, 2012. [Online]. Available: 10.5772/intechopen.76854

[71] T. Theodorsen, "The structure of turbulence," in *50 Jahre Grenzschichtforschung*. Springer, 1955, pp. 55–62.

[72] M. R. Head and P. Bandyopadhyay, "New aspects of turbulent boundary-layer structure," *Journal of fluid mechanics*, vol. 107, pp. 297–338, 1981.

[73] V. Picchio, V. Cammisotto, F. Pagano, R. Carnevale, and I. Chimenti, "Generation, Evolution, and Characterization of Turbulence Coherent Structures," *Intechopen*, no. Cell Interaction - Regulation of Immune Responses, Disease Development and Management Strategies, pp. 1–15, 2020. [Online]. Available: https://www.intechopen.com/books/advanced-biometric-technologies/liveness-detection-in-biometrics

[74] H. T. Kim, S. J. Kline, and W. C. Reynolds, "The production of turbulence near a smooth wall in a turbulent boundary layer," *Journal of Fluid Mechanics*, vol. 50, no. 1, pp. 133–160, 1971.

[75] J. R. Roth, D. M. Sherman, and S. P. Wilkinson, "BOUNDARY LAYER FLOW CONTROL WITH A ONE ATMOSPHERE UNIFORM GLOW DISCHARGE SURFACE PLASMA," *AIAA Journal*, 1998. [Online]. Available: https://ntrs.nasa.gov/archive/nasa/casi.ntrs.nasa.gov/19980022683.pdf

[76] L. S. Hultgren and D. E. Ashpis, "Demonstration of separation delay with glow-discharge plasma actuators," *41st Aerospace Sciences Meeting and Exhibit*, no. December 2004, 2003.

[77] S. Grundmann and C. Tropea, "Experimental damping of boundary-layer oscillations using DBD plasma actuators," *International Journal of Heat and Fluid Flow*, vol. 30, no. 3, pp. 394–402, 2009. [Online]. Available: http://dx.doi.org/10.1016/j.ijheatfluidflow.2009.03.004

[78] C. Y. Schuele, T. C. Corke, and E. Matlis, "Control of stationary cross-flow modes in a Mach 3.5 boundary layer using patterned passive and active roughness," *Journal of Fluid Mechanics*, vol. 718, pp. 5–38, 2013.

[79] F. O. Thomas, A. Kozlov, and T. C. Corke, "Plasma actuators for bluff body flow control," *Collection of Technical Papers - 3rd AIAA Flow Control Conference*, vol. 1, no. June, pp. 60–75, 2006.

[80] A. Asghar and E. J. Jumper, "Phase synchronization of vortex shedding from two circular cylinders using plasma actuators," *AIAA Journal*, vol. 47, no. 7, pp. 1608–1616, 2009.

[81] N. Benard, J. Jolibois, and E. Moreau, "Lift and drag performances of an axisymmetric airfoil controlled by plasma actuator," *Journal of Electrostatics*, vol. 67, no. 2-3, pp. 133–139, 2009.

[82] D. Greenblatt, B. Göksel, I. Rechenberg, C. Y. Schüle, D. Romann, and C. O. Paschereit, "Dielectric barrier discharge flow control at very low flight Reynolds numbers," *AIAA Journal*, vol. 46, no. 6, pp. 1528–1541, 2008.

[83] P. F. Zhang, J. J. Wang, L. H. Feng, and G. B. Wang, "Experimental study of plasma flow control on highly swept delta wing," *AIAA Journal*, vol. 48, no. 1, pp. 249–252, 2010.

[84] M. R. Visbal, "Strategies for control of transitional and turbulent flows using plasma-based actuators," *International Journal of Computational Fluid Dynamics*, vol. 24, no. 7, pp. 237–258, 2006.

[85] D. P. Rizzetta and M. R. Visbal, "Large eddy simulation of plasma-based control strategies for bluff body flow," *AIAA Journal*, vol. 47, no. 3, pp. 717–729, 2009.

[86] X. Huang and X. Zhang, "Streamwise and spanwise plasma actuators for flow-induced cavity noise control," *Physics of Fluids*, vol. 20, no. 3, 2008.

[87] N. Benard, J. P. Bonnet, G. Touchard, and E. Moreau, "Flow control by dielectric barrier discharge actuators: Jet mixing enhancement," *AIAA Journal*, vol. 46, no. 9, pp. 2293–2305, 2008.

[88] P. F. Zhang, A. B. Liu, and J. J. Wang, "Aerodynamic modification of a NACA 0012 airfoil by trailing-edge plasma gurney flap," *AIAA Journal*, vol. 47, no. 10, pp. 2467–2474, 2009.

[89] P. F. Zhang, B. Yan, A. B. Liu, and J. J. Wang, "Numerical simulation on plasma circulation control airfoil," *AIAA Journal*, vol. 48, no. 10, pp. 2213–2226, 2010.

[90] J. Little and M. Samimy, "High-lift airfoil separation with dielectric barrier discharge plasma actuation," *AIAA Journal*, vol. 48, no. 12, pp. 2884–2898, 2010.

[91] A. Balogh, O. M. Aamo, and M. Krstić, "Optimal Mixing Enhancement in 3-D Pipe Flow," *IEEE Transactions on Control Systems Technology*, vol. 13, no. 1, pp. 27–41, 2005.

[92] M. Gad-El-Hak and R. F. Blackwelder, "Selective suction for controlling bursting events in a boundary layer," *AIAA Journal*, vol. 27, no. 3, pp. 308–314, 1989.

[93] L. Löfdahl and M. Gad-el Hak, "MEMS applications in turbulence and flow control," *Progress in Aerospace Sciences*, vol. 35, no. 2, pp. 101–203, 1999.

[94] F. Sherman, S. Tung, C. J. Kim, C. M. Ho, and J. Woo, "Flow control by using high-aspect-ratio, in-plane microactuators," *Sensors and Actuators, A: Physical*, vol. 73, no. 1-2, pp. 169–175, 1999.

[95] S. A. Jacobson and W. C. Reynolds, "Active control of streamwise vortices and streaks in boundary layers," *Journal of Fluid Mechanics*, vol. 360, pp. 179–211, 1998.

[96] W. Schoppa and F. Hussain, "A large-scale control strategy for drag reduction in turbulent boundary layers," *Physics of Fluids*, vol. 10, no. 5, pp. 1049–1051, 1998.

[97] J. Yao, X. Chen, and F. Hussain, "Drag control in wall-bounded turbulent flows via spanwise opposed wall-jet forcing," *Journal of Fluid Mechanics*, vol. 852, no. August, pp. 678–709, 2018.

[98] R. Rathnasingham and K. S. Breuer, "Active control of turbulent boundary layers," *Journal of Fluid Mechanics*, vol. 495, pp. 209–233, 2003.

[99] X. Meng, J. Cai, Y. Tian, X. Han, D. Zhang, and H. Hu, "Experimental study of deicing and anti-icing on a cylinder by DBD plasma actuation," *47th AIAA Plasmadynamics and Lasers Conference*, no. June, pp. 1–14, 2016.

[100] F. Rodrigues, J. Pascoa, and M. Trancossi, "Heat generation mechanisms of DBD plasma actuators," *Experimental Thermal and Fluid Science*, vol. 90, no. May 2017, pp. 55–65, 2018. [Online]. Available: http://dx.doi.org/10.1016/j.expthermflusci.2017.09.005

[101] A. Santhanakrishnan, J. D. Jacob, and Y. B. Suzen, "Flow control using plasma actuators and linear/annular plasma synthetic jet actuators," *Collection of Technical Papers - 3rd AIAA Flow Control Conference*, vol. 2, no. February 2015, pp. 685–715, 2006.

[102] A. Santhanakrishnan and J. D. Jacob, "Flow control with plasma synthetic jet actuators," *Journal of Physics D: Applied Physics*, vol. 40, no. 3, pp. 637–651, 2007.

[103] A. B. Liu, P. F. Zhang, B. Yan, C. F. Dai, and J. J. Wang, "Flow characteristics of synthetic jet induced by plasma actuator," *AIAA Journal*, vol. 49, no. 3, pp. 544–553, 2011.

[104] T. N. Jukes, T. Segawa, and H. Furutani, "Flow control on a NACA 4418 using dielectric-barrier-discharge vortex generators," *AIAA Journal*, vol. 51, no. 2, pp. 452–464, 2013.

[105] J. R. Roth, D. M. Sherman, and S. P. Wilkinson, "Electrohydrodynamic Flow Control with a Glow-Discharge Surface Plasma," *AIAA Journal*, vol. 38, no. 7, pp. 1166–1172, jul 2000. [Online]. Available: http://arc.aiaa.org/doi/10.2514/2.1110

[106] J. R. Roth, J. Rahel, X. Dai, and D. M. Sherman, "The physics and phenomenology of One Atmosphere Uniform Glow Discharge Plasma (OAUGDP?) reactors for surface treatment applications," *Journal of Physics D: Applied Physics*, vol. 38, no. 4, pp. 555–567, feb 2005. [Online]. Available: http://stacks.iop.org/0022-3727/38/i=4/a=007?key=crossref.77bfdc552e4a7c4d6a1c55ca929fe81c

[107] C. L. Enloe, T. E. McLaughlin, R. D. VanDyken, and J. C. Fischer, "Plasma structure in the aerodynamic plasma actuator," *AIAA Paper*, no. January, pp. 9466–9474, 2004.

[108] E. Peers, X. Huang, and X. Luo, "A numerical model of plasma-actuator effects in flow-induced noise control," *IEEE Transactions on Plasma Science*, vol. 37, no. 11, pp. 2250–2256, 2009.

[109] W. Shyy, B. Jayaraman, and A. Anderson, "Modeling of glow discharge-induced fluid dynamics," *JOURNAL OF APPLIED PHYSICS*, vol. 92, no. 11, 2002. [Online]. Available: https://www.researchgate.net/profile/Balaji{_}Jayaraman3/publication/224490920{_}Modeling{_}of{_}glow{_}discharge-induced{_}fluid{_}dynamics/links/54dcd17a0cf25b09b912d17d.pdf

[110] Y. B. Suzen, P. G. Huang, J. D. Jacob, and D. E. Ashpis, "Numerical simulations of plasma based flow control applications," *AIAA paper*, no. June, pp. 1–11, 2005. [Online]. Available: http://arc.aiaa.org/doi/pdf/10.2514/6.2005-4633

[111] T. C. Corke, M. L. Post, and D. M. Orlov, "Single Dielectric Barrier Discharge Plasma Enhanced Aerodynamics: Physics, Modeling and Applications," *Experiments in Fluids*, 2009. [Online]. Available: http://www3.nd.edu/{~}tcorke/w.ExpFluidsArticle/ExpFluids{_}plasma{_}2.pdf

[112] B. E. Mertz, *Refinement, validation, and implementation of lumped circuit element model for single dielectric barrier discharge plasma actuators*. University of Notre Dame, 2010.

[113] S. Roy and D. V. Gaitonde, "Modeling surface discharge effects of atmospheric RF on gas flow control," *43rd AIAA Aerospace Sciences Meeting and Exhibit - Meeting Papers*, pp. 5815–5823, 2005.

[114] S. Roy, "Flow actuation using radio frequency in partially ionized collisional plasmas," *Applied Physics Letters*, vol. 86, no. 10, pp. 1–3, 2005.

[115] K. P. Singh and S. Roy, "Simulation of an asymmetric single dielectric barrier plasma actuator," *Journal of Applied Physics*, vol. 98, no. 8, pp. 0–7, 2005.

[116] J. P. Boeuf and L. C. Pitchford, "Electrohydrodynamic force and aerodynamic flow acceleration in surface dielectric barrier discharge," *Journal of Applied Physics*, vol. 97, no. 10, 2005.

[117] B. Jayaraman, S. Thakur, and W. Shyy, "Modeling of fluid dynamics and heat transfer induced by dielectric barrier plasma actuator," *Journal of Heat Transfer*, vol. 129, no. 4, pp. 517–525, 2007.

[118] B. Jayaraman and W. Shyy, "Modeling of dielectric barrier discharge-induced fluid dynamics and heat transfer," *Progress in Aerospace Sciences*, vol. 44, no. 3, pp. 139–191, 2008.

[119] B. Jayramann, "Computational modeling of glow discharge-induced fluid dynam-ics [Ph. D. thesis]," *University of Florida*, 2006.

[120] J. P. Boeuf, Y. Lagmich, and L. C. Pitchford, "Contribution of positive and negative ions to the electrohydrodynamic force in a dielectric barrier discharge plasma actuator operating in air," *Journal of Applied Physics*, vol. 106, no. 2, 2009.

[121] T. Unfer, J. P. Boeuf, F. Rogier, and F. Thivet, "Modeling of Dielectric Barrier Discharge and coupling with computational fluid dynamics," *46th AIAA Aerospace Sciences Meeting and Exhibit*, no. January, 2008.

[122] H. Nishida, T. Nonomura, and T. Abe, "Three-dimensional simulations of discharge plasma evolution on a dielectric barrier discharge plasma actuator," *Journal of Applied Physics*, vol. 115, no. 13, 2014.

[123] M. M. Turner, "Kinetic properties of particle-in-cell simulations compromised by Monte Carlo collisions," *Physics of Plasmas*, vol. 13, no. 3, 2006.

[124] G. Dufour and F. Rogier, "Based Plasma Actuators for Flow Control : the Numerical Modeling of Dielectric Barrier Discharge Based Plasma Actuators for Flow Control : the COPAIER / CEDRE Example," *Aerospacelab Journal*, no. 10, pp. AL10–5, 2015. [Online]. Available: https://hal.archives-ouvertes.fr/hal-01270823

[125] K. Kourtzanidis, F. Rogier, and G. Dufour, "Self-consistent modeling of a surface AC-DBD actuator: In-depth analysis of positive and negative phases," *Under Review*, 2020.

[126] A. A. Vlasov, "the Vibrational Properties of an Electron Gas," *Soviet Physics Uspekhi*, vol. 10, no. 6, pp. 721–733, 1968.

[127] J. M. Hagelaar and L. C. Pitchford, "Solving the Boltzmann equation to obtain electron transport coefficients and rate coefficients for fluid models," *Plasma Sources Sci. Technol. Plasma Sources Sci. Technol*, vol. 14, no. 14, pp. 722–733, 2005. [Online]. Available: http://iopscience.iop.org/0963-0252/14/4/011

[128] A. V. Phelps, "Phelps database, LXCat," 2012. [Online]. Available: www.lxcat.net/Phelps

[129] L. C. Pitchford and J. P. Boeuf, "SIGLO database, LXCat," 2012. [Online]. Available: www.lxcat.net/SIGLO

[130] J.-C. Matéo-Vélez, "Modélisation et simulation numérique de la génération de plasma dans les décharges couronnes et de son interaction avec l'aérodynamique," Ph.D. dissertation, Toulouse, ENSAE, 2006.

[131] G. J. M. Hagelaar and L. C. Pitchford, "Solving the Boltzmann equation to obtain electron transport coefficients and rate coefficients for fluid models," *Plasma Sources Science and Technology*, vol. 14, no. 4, pp. 722–733, nov 2005. [Online]. Available: http://stacks.iop.org/0963-0252/14/i=4/a=011?key=crossref.2a24e96f0d2a1cd028c8141d01c6b2b0

[132] G. J. M. Hagelaar and G. M. W. Kroesen, "Speeding up fluid models for gas discharges by implicit treatment of the electron energy source term," *Journal of Computational Physics*, vol. 159, no. 1, pp. 1–12, 2000.

[133] B. Van Leer and P. R. Woodward, "The MUSCL code for compressible flow: philosophy and results," *TICOM Conferece*, 1979.

[134] J. M. Ortega, *Numerical analysis: a second course*. SIAM, 1990.

[135] P. Gosselet, C. Rey, P. Gosselet, C. Rey, and P. Gosselet, "Non-overlapping domain decomposition methods in structural mechanics To cite this version : HAL Id : hal-00277626 Non-overlapping domain decomposition methods in structural mechanics," 2012.

[136] V. Alexiades, G. Amiez, and P. A. Gremaud, "Super-time-stepping acceleration of explicit schemes for parabolic problems," *Communications in Numerical Methods in Engineering*, vol. 12, no. 1, pp. 31–42, 1996.

[137] E. Moreau, "Airflow control by non-thermal plasma actuators," *Journal of Physics D: Applied Physics*, vol. 40, no. 3, pp. 605–636, 2007.

[138] E. Moreau, R. Sosa, and G. Artana, "Electric wind produced by surface plasma actuators: A new dielectric barrier discharge based on a three-electrode geometry," *Journal of Physics D: Applied Physics*, vol. 41, no. 11, 2008.

[139] C.-C. Wang, R. J. Durscher, and S. Roy, "Three-dimensional effects of curved plasma actuators in quiescent air," *Journal of Applied Physics*, 2011.

[140] K. S. Choi and J. H. Kim, "Plasma virtual roughness elements for cross-flow instability control," *Experiments in Fluids*, vol. 59, no. 10, pp. 1–15, 2018. [Online]. Available: http://dx.doi.org/10.1007/s00348-018-2609-x

[141] B. L. Smith and A. Glezer, "The formation and evolution of synthetic jets," *Physics of Fluids*, vol. 10, no. 9, pp. 2281–2297, 1998.

[142] R. A. Siliprandi, H. E. Roman, R. Barni, and C. Riccardi, "Characterization of the streamer regime in dielectric barrier discharges," *Journal of Applied Physics*, vol. 104, no. 6, 2008.

[143] I. Biganzoli, R. Barni, A. Gurioli, R. Pertile, and C. Riccardi, "Experimental investigation of Lissajous figure shapes in planar and surface dielectric barrier discharges," *Journal of Physics: Conference Series*, vol. 550, no. 1, 2014.

[144] Y. Hao, J. Chen, L. Yang, and X. Wang, "Lissajous figures of glow and filamentary dielectric barrier discharges under high frequency voltage at atmospheric pressure in helium," *Proceedings of the IEEE International Conference on Properties and Applications of Dielectric Materials*, pp. 626–629, 2009.

[145] J. P. Boeuf, Y. Lagmich, T. Unfer, T. Callegari, and L. C. Pitchford, "Electrohydrodynamic force in dielectric barrier discharge plasma actuators," *Journal of Physics D: Applied Physics*, vol. 40, no. 3, pp. 652–662, 2007.

[146] P. Audier, H. Rabat, A. Leroy, and D. Hong, "Experimental investigation of a surface {DBD} plasma actuator at atmospheric pressure in different N2/O2gas mixtures," *Plasma Sources Science and Technology*, vol. 23, no. 6, p. 65045, nov 2014. [Online]. Available: https://doi.org/10.1088/0963-0252/23/6/065045

[147] G. Neretti, P. Seri, M. Taglioli, A. Shaw, F. Iza, and C. A. Borghi, "Geometry optimization of linear and annular plasma synthetic jet actuators," *Journal of Physics D: Applied Physics*, vol. 50, no. 1, p. 15210, 2016.

[148] M. A. Leschziner, H. Choi, and K. S. Choi, "Flow-control approaches to drag reduction in aerodynamics: Progress and prospects," *Philosophical Transactions of the Royal Society A: Mathematical, Physical and Engineering Sciences*, vol. 369, no. 1940, pp. 1349–1351, 2011.

[149] L. P. Chamorro, R. E. Arndt, and F. Sotiropoulos, "Drag reduction of large wind turbine blades through riblets: Evaluation of riblet geometry and application strategies," *Renewable Energy*, vol. 50, pp. 1095–1105, 2013. [Online]. Available: http://dx.doi.org/10.1016/j.renene.2012.09.001

[150] H. M. Blackburn and S. J. Sherwin, "Formulation of a Galerkin spectral element-Fourier method for three-dimensional incompressible flows in cylindrical geometries," *Journal of Computational Physics*, vol. 197, no. 2, pp. 759–778, 2004.

[151] T. N. Jukes and K.-S. Choi, "Dielectric-barrier-discharge vortex generators: characterisation and optimisation for flow separation control," *Experiments in Fluids*, vol. 52, no. 2, pp. 329–345, nov 2011. [Online]. Available: http://link.springer.com/10.1007/s00348-011-1213-0

[152] M. Forte, J. Jolibois, J. Pons, E. Moreau, G. Touchard, and M. Cazalens, "Optimization of a dielectric barrier discharge actuator by stationary and non-stationary measurements of the induced flow velocity: Application to airflow control," *Experiments in Fluids*, vol. 43, no. 6, pp. 917–928, 2007.

[153] R. A. Humble, S. A. Craig, J. Vadyak, P. D. McClure, J. W. Hofferth, and W. S. Saric, "Spatiotemporal structure of a millimetric annular dielectric barrier discharge plasma actuator," *Physics of Fluids*, vol. 25, no. 1, 2013.

[154] A. Zhang, M. Dong, and Y. Zhang, "Receptivity of secondary instability modes in streaky boundary layers," *Physics of Fluids*, vol. 30, no. 11, 2018. [Online]. Available: http://dx.doi.org/10.1063/1.5046136